POLITECNICO
MILANO 1863

SCUOLA DI INGEGNERIA INDUSTRIALE
E DELL'INFORMAZIONE

Evaluation of Geometrical Accuracy in Single-Isocenter Multi-Target Cranial Stereotactic Radiotherapy and Stereotactic Radiosurgery

Tesi di Laurea Magistrale in
Computer Science and Engineering - Ingegneria
Informatica

Author: **Enrico Sarneri**

Student ID: 968934
Advisor: Prof. Ing. Maria Gabriella Signorini
Co-Advisors: Dott. Regis Ferrand, Dott. Jean-Luc Dumas
Academic Year: 2022-23

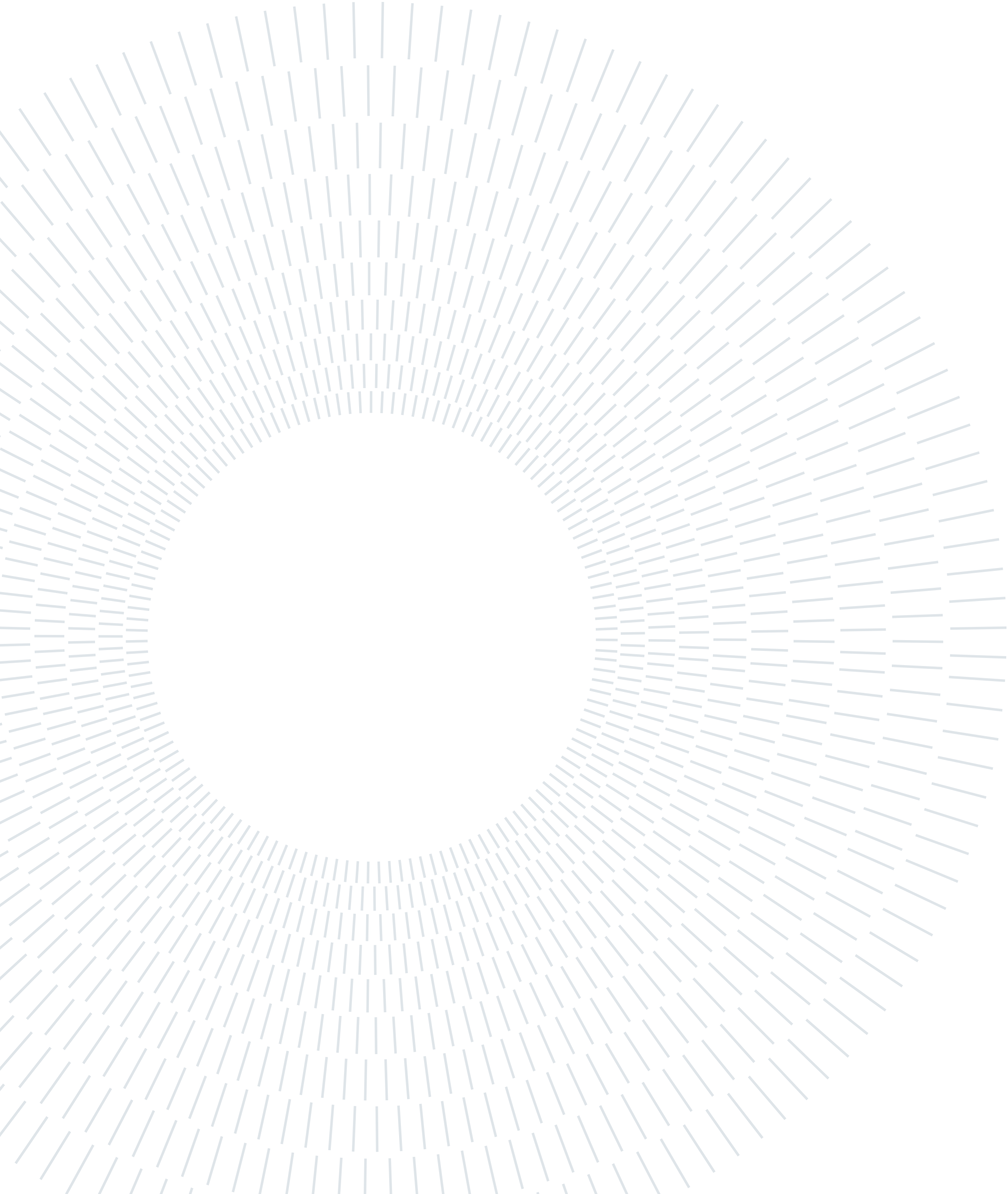

Contents

List of Figures iii

List of Tables vi

Abstract 1

Sommario 7

1 Introduction 13
- 1.1 Motivations and Goal . . . 15
- 1.2 Contributions . . . 16
- 1.3 Structure of the Thesis . . . 19

2 Background 21
- 2.1 Radiotherapy . . . 21
- 2.2 Technologies . . . 23
- 2.3 Pipeline . . . 30
- 2.4 Quality Assurance . . . 34

3 Materials and Methods 37
- 3.1 Materials . . . 37
  - 3.1.1 Phantoms . . . 37
  - 3.1.2 Treatment Plan . . . 39
- 3.2 Methods . . . 57
  - 3.2.1 Tools . . . 58
  - 3.2.2 Dataset Preparation . . . 58
  - 3.2.3 Preprocessing . . . 63
  - 3.2.4 Sphere Selection and Identification . . . 75
  - 3.2.5 Sphere Shift Measurements . . . 82
  - 3.2.6 DRR - Irradiation Field Reconstruction . . . 88

3.2.7 Portal Image - Irradiation Field Identification 93
3.2.8 Irradiation Field Shift Measurements 98

4 Results and Discussion **103**
4.1 Sphere Detection Evaluation 103
4.2 Sphere Displacement Evaluation 112
4.3 Irradiation Field Displacement Evaluation 115

5 Conclusions **131**

6 Future Developments **133**

Acknowledgements **135**

Bibliography **141**

List of Figures

2.1 CT scanner and functioning of the CT scanner 24
2.2 CT planes and multiple axial abdomen slices 25
2.3 Treatment Planning System (TPS). 25
2.4 LINAC and LINAC components 29
2.5 LINAC treatment head and MLC irradiation field shape 29
2.6 LINAC kV and MV sources, flat-panel detectors and 2D projections of 3D volume 30
2.7 Standard SRT/SRS workflow 33

3.1 Head phantom and its 3D rendering reconstruction on 3D Slicer 5.0.3 38
3.2 ISO Cube. 39
3.3 Different ISO Cube planes 39
3.4 DICOM format. 41
3.5 DRR images from the 4 different gantry angle rotations. 46
3.6 DRR ANT Image and correspondent Portal Image 51
3.7 DRR LAT G Image and correspondent Portal Image 52
3.8 DRR LAT D Image and correspondent Portal Image 53
3.9 DRR POST Image and correspondent Portal Image 54
3.10 Hounsfield Unit. 61
3.11 DRR images batch. 62
3.12 Portal images batch. 63
3.13 Image reconstruction process. 64
3.14 Flat panel detector. 65
3.15 Pixel spacing and magnification. 66
3.16 Windowed DRR images batch. 70
3.17 Windowed Portal images batch. 71
3.18 Bicubic Interpolation. 73
3.19 ESRGAN. 74
3.20 ANT DRR: Original Image, Bicubic Interpolation, ESRGAN. 75

3.21 ROIs cropped from Portal images. 76
3.22 Hough Circle Transform. 78
3.23 Result of Hough Circle Transform for ANT Portal image crops. . . . 79
3.24 ANT Portal image identified spheres. 79
3.25 ROIs cropped from DRR images. 81
3.26 Result of Hough Circle Transform for ANT DRR image crops. 82
3.27 ANT DRR Image - identified spheres. 82
3.28 Blended ANT DRR and ANT Portal images. 84
3.29 Blended LAT D DRR and LAT D Portal images. 84
3.30 Blended LAT G DRR and LAT G Portal images. 85
3.31 Blended POST DRR and POST Portal images. 85
3.32 ISO Cube Phantom DRR images from the 4 different gantry angles. . 87
3.33 ISO Cube Phantom DRR images from the 4 different gantry angles. . 88
3.34 MLC leaf pairs positions. 91
3.35 ANT DRR image irradiation fields. 92
3.36 LAT D DRR image irradiation fields. 92
3.37 LAT G DRR image irradiation fields. 93
3.38 POST DRR image irradiation fields. 93
3.39 Geometric Unsharpness. 95
3.40 Penumbra Effect. 95
3.41 Batch of thresholded Portal images. 97
3.42 ANT Portal image thresholded - zoom. 98
3.43 ANT Portal image detected irradiation fields. 98
3.44 Blended ANT DRR and ANT Portal images - irradiation fields. . . . 100
3.45 Blended LAT D DRR and LAT D Portal images - irradiation fields. . 100
3.46 Blended LAT G DRR and LAT G Portal images - irradiation fields. . 101
3.47 Blended POST DRR and POST Portal images - irradiation fields. . . 101

4.1 Comparison between identification algorithm and manual identification for X and Y-coordinates in ANT DRR Image Spheres. 106
4.2 Comparison between identification algorithm and manual identification for X and Y-coordinates in LAT D DRR Image Spheres. 106
4.3 Comparison between identification algorithm and manual identification for X and Y-coordinates in LAT G DRR Image Spheres. 107
4.4 Comparison between identification algorithm and manual identification for X and Y-coordinates in POST DRR Image Spheres. 107

4.5 2D Euclidean Distance. 108
4.6 Comparison between identification algorithm and manual identification for X and Y-coordinates in ANT Portal Image Spheres. 110
4.7 Comparison between identification algorithm and manual identification for X and Y-coordinates in LAT D Portal Image Spheres. 110
4.8 Comparison between identification algorithm and manual identification for X and Y-coordinates in LAT G Portal Image Spheres. 111
4.9 Comparison between identification algorithm and manual identification for X and Y-coordinates in POST Portal Image Spheres. 111
4.10 Measured Spheres Displacements in DRR and Portal images. 115
4.11 Intersection over Union. 116
4.12 Measured averaged edge displacements for each irradiation field between DRR and Portal Images. 128
4.13 Measured 3D displacements averaging all irradiation fields of DRR and Portal Images. 128
4.14 2D displacements of 3D volume. 129

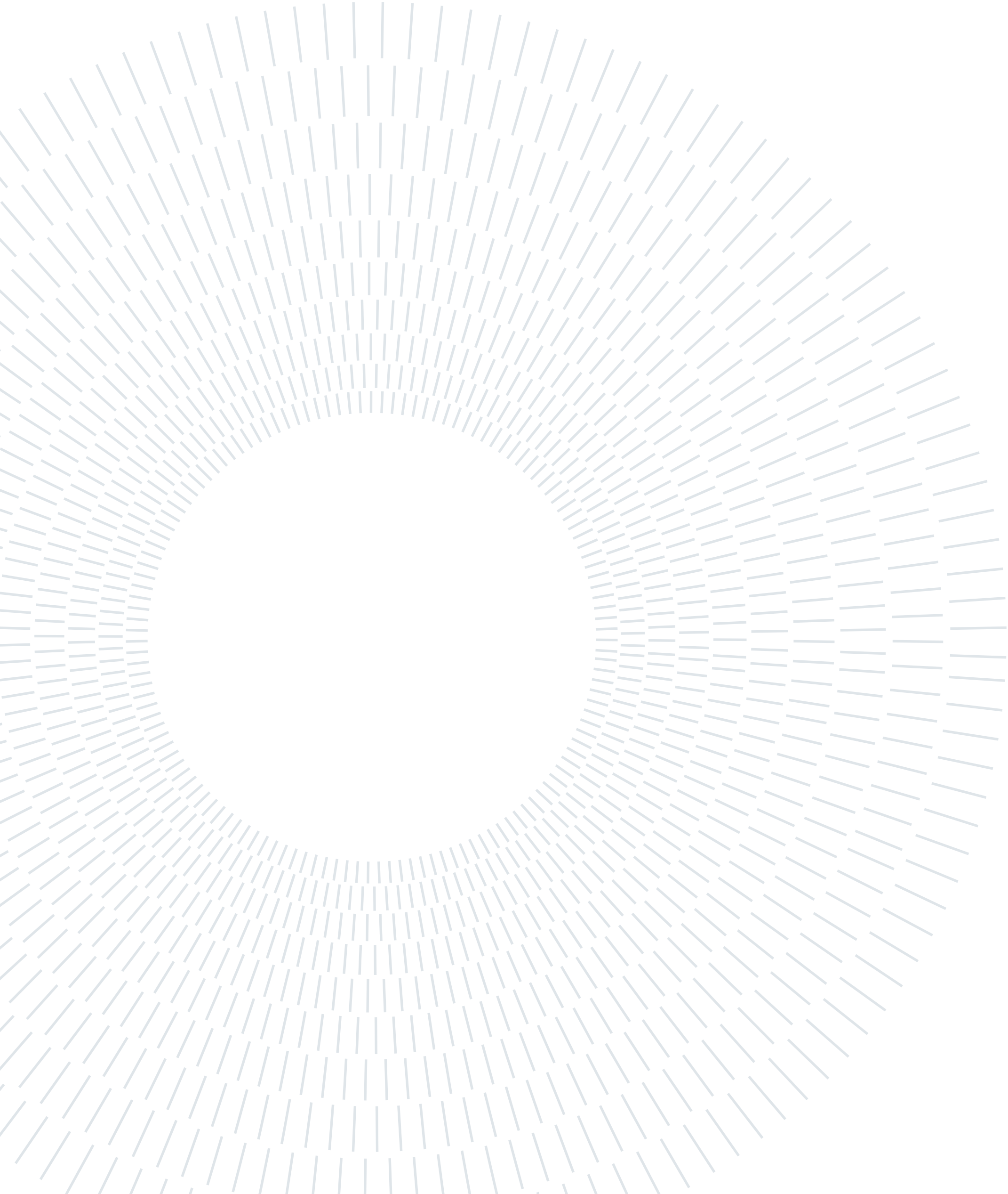

List of Tables

3.1 CT Scan DICOM Tags. 44
3.2 Image Acquisition Gantry Angles. 45
3.3 DRR ANT DICOM Tags. 49
3.4 Portal Image ANT DICOM Tags. 57
3.5 Programming Language. 58
3.6 Libraries. 58

4.1 Coordinates of detected sphere centers - DRR Images. 103
4.2 Coordinates of detected sphere centers - Portal Images. 104
4.3 Coordinates of sphere centers manually labeled - DRR Images. 105
4.4 Coordinates of sphere centers manually labeled - Portal Images. . . . 105
4.5 Difference between manually identified and algorithm identified spheres for each DRR image as 2D Euclidean distance. 109
4.6 Difference between manually identified and algorithm identified spheres for each Portal image as 2D Euclidean distance. 112
4.7 Measured displacements between correspondent spheres in DRR and Portal images - identification algorithm. 113
4.8 Measured displacements between correspondent spheres in DRR and Portal images - manual annotation. 114
4.9 DRR ANT Image Irradiation Fields Coordinates. 117
4.10 DRR LAT D Image Irradiation Fields Coordinates. 118
4.11 DRR POST Image Irradiation Fields Coordinates. 119
4.12 DRR LAT G Image Irradiation Fields Coordinates. 120
4.13 ANT Portal Image Irradiation Fields Coordinates. 121
4.14 LAT D Portal Image Irradiation Fields Coordinates. 122
4.15 POST Portal Image Irradiation Fields Coordinates. 123
4.16 LAT G Portal Image Irradiation Fields Coordinates. 124
4.17 IoU metrics for each irradiation field in all images. 125
4.18 Edge displacement for each irradiation field in all paired images. . . . 127

4.19 Total time required for the entire pipeline. 130

Abstract

Introduction

Radiotherapy (RT), together with surgery and chemotherapy, is one of the three main modalities used in the treatment of cancer. Nowadays, thanks to the advanced technological development of imaging equipment, Image-Guided Radiotherapy (IGRT) has been introduced. It allows visualization of the patient's anatomy prior to radiation fraction delivery, allowing accurate knowledge of the location of the target volume. IGRT has also been integrated with Stereotactic Radiotherapy (SRT) and Stereotactic Radiosurgery (SRS): this combination of procedures is the actual standard for treating particularly sensitive and less-evident zones, such as very small lesions in the cranium.

IGRT is based on the integration of two fundamental imaging systems on the Linear Accelerator (LINAC): a kV X-ray source with its flat imaging panel, i.e., On-Board Imaging (OBI), and an MV X-ray source with the respective flat imaging panel, i.e., Electronic Portal Imaging (EPI). Both of them are used for assessing patient positioning before treatment and have the possibility to perform 2D and 3D volume acquisitions; the latter also represents the high-dose X-ray source for effective patient treatment. Once an IGRT system is commissioned, it is necessary to perform periodic Quality Assurance (QA) controls to ensure optimal therapy outcomes. In particular, geometric accuracy aims to verify the setting of the patient and X-ray beams.

The purpose of this work is to develop an automatic method to evaluate the alignments of multiple targets - simulating distributed metastases - and Multi-Leaf Collimator (MLC) irradiation beam fields from a cranial phantom in single isocenter treatments, after previous registration with the OBI system. The need for this task stems from the problem that MV image analysis, due to low subject contrast and low signal-to-noise ratio, is still performed by hand. Therefore, an automatized process is needed. Specifically, this method performs analysis and comparisons of paired 2D Digital Reconstructed Radiographs (DRRs) and Portal images, enabling sub-millimeter accuracy and an 88% speedup compared with current manually performed QA processes.

Methods

The entire process is based on four couples of 2D images, where each couple is characterized by a DRR and a Portal image representing different projections of the cranial phantom i.e. anterior, left lateral, right lateral, and posterior views (0°, 90°, 180°, and 270° gantry angle rotations). DRR images are virtually generated from the Treatment Planning System (TPS) and represent the ground truth in terms of volume positioning. Portal images, instead, are acquired through the EPI system at the time of treatment and should ideally match the correspondent DRRs in a perfect treatment.

Initially, the images were prepared by reading the original DICOM format and performing pixel value transformations relying on Pydicom functions, a Python DICOM image analysis toolkit widely used in academia and industry. This first step allowed us to move from raw pixel data values to *float64* dtype Hounsfield Unit (HU) quantitative measurements. The second step involves resampling for DRR images. Since DRR and Portal images were generated considering different source-to-image distances (SID) - $1000mm$ and $1500mm$ respectively - and different pixel spacing values - (0.9765625, 0.9765625) and (0.784, 0.784) respectively, it was necessary to bring them to the same plane (SID value) in order to allow geometrical comparisons. This was done by performing resampling for DRR images considering the value of pixel spacing that Portal images would have had if they had been generated with a SID of $1000mm$. The resampling process relied on SimpleITK methods. After that, the windowing step was implemented for both DRR and Portal images calculating the optimal values of Window Width (WW) and Window Level (WL) so that all target spheres were clearly visible in all images and all unnecessary elements were filtered out. This is done by customizing HU ranges over which images are displayed. A final step of standardization to the 0-255 grayscale is then necessary.

The next stage consists of executing an image up-scaling, increasing image resolution by a factor of x8. This operation was performed through image interpolation and a specific Generative Adversarial Network (GAN). In this way, the value of pixel spacing assumes a much smaller value, allowing more accurate distance measurements. After that, the objective was to isolate the different target spheres in each image in order to facilitate automatic shape recognition. We then implemented a method through which the operator, thanks to a GUI, is able to draw approximate bounding boxes around each sphere on Portal images. From the extracted crops, we then performed sphere shape recognition through Hough Transform method. The saved coordinates of each crop were then translated on DRR images, where image padding was implemented and sphere shape recognition was performed a second time. At this point, we proceeded by making measurements of displacements between each corresponding sphere in all coupled images.

The final stage involves MLC irradiation beam fields. The theoretical fields of DRR images were reconstructed by analyzing DICOM header information, where every necessary information about images belonging to the treatment plan is contained. We still relied on Pydicom for this purpose. The fields of Portal images, on the other side, were computed by a sequence of thresholding, blurring, and Canny Edge detection, considering approximations due to the penumbra effect irradiation problem. Also here, the following step consists of measuring the displacements between each correspondent irradiation field around each target on DRR and Portal images.

Results and Discussion

The first aim is to quantify the displacements between corresponding spheres in DRR and Portal images. For this purpose, we adopted Euclidian distance in pixel coordinates (converted then in millimeters) on 2D images to evaluate the shifts of identified sphere centers.

Firstly, to check the effectiveness of the shape identification algorithm, we compared the detected sphere centers coordinates of DRR and Portal Images with centers manually localized by a skilled medical physicist operator through 3D Slicer, an open-source software package widely used in this domain. The differences between the two identification methods for each sphere center in DRR images never exceeded the value of $0.3mm$. In particular, they resulted in average values of $0.20395mm$ for ANT image, $0.197mm$ for LAT D image, $0.198725mm$ for LAT G image, and $0.21185mm$ for POST image, considering all spheres. These results certainly depend on the high contrast that characterizes DRR images and facilitates the identification of the centers of the spheres for both our implemented method and the operator. For what concerns Portal images we registered average values of $0.229525mm$ for ANT image, $0.289525mm$ for LAT D image, $0.285275mm$ for LAT G image, and $0.38435mm$ for POST image. The differences between the two methods are still good but a bit higher with respect to the previous case, mainly due to the lower signal-to-noise ratio and artifacts that characterize Portal images.

After that, we performed the computation of displacements between corresponding spheres. The displacements represent the accuracy of the registration phase and the alignment between the EPI and OBI systems. We evaluated these displacements firstly considering the results coming from our identification method, and then considering manual identification. The displacements have been measured again through 2D Euclidean distance of pixel coordinates for each pair of spheres in superimposed correspondent DRR and Portal images. Considering our identification method we registered average displacements of $0.5356mm$ for sphere 1, $0.7152mm$ for sphere 2, $0.5864mm$ for sphere 3, and $0.4959mm$ for sphere 4. With manual identification, on the other side, we registered $0.6169mm$ for sphere 1, $0.7247mm$ for sphere 2, $0.7084mm$ for sphere 3, and $0.5063mm$ for sphere 4 as average values. These results show how the two identification methods do not significantly differ and that the registration phase, together with the alignment of EPI and OBI systems are accurate, strictly below $1.5mm$ threshold, even if we take into account the uncertainties due to the different methods.

For what concerns irradiation beam fields, the principle is the same. Couples of corresponding irradiation fields, belonging to paired spheres, were superimposed and their distances were then computed. Here we considered the reconstructed coordinates from DICOM tags as ground truth irradiation fields, and the algorithm-identified coordinates as detected irradiation fields. In this case, the displacements have been evaluated on the four sides of each irradiation field, where the threshold not to be exceeded is still $1.5mm$. Edge displacements have been computed by considering the maximum value between the differences of the paired coordinates of the extremes for each edge. In general, all the displacements fall into the desired threshold. There are a few peaks of $1.3327mm$ and $1.2543mm$, while all the other cases remain below $1mm$. Also, comparing the two methods, we registered how there is not a significant difference between them, which resulted in a maximum of $0.1252mm$ for irradiation field 2.

Finally, we compared the performances of the entire automatized process through our developed program with the manually performed process. For what concerns the manual process, we considered the execution by an expert medical physician and we took average values for each phase. It is clear that from a computational point of view, the procedure executed by our developed program is way faster than the manual process, allowing us to speed up the entire pipeline of execution by 88%.

Conclusions

In this work, a new automatic method was developed for measuring the displacements of multiple cranial phantom sphere targets and their irradiation fields on 2D Portal images, relative to their theoretical positions in 2D DRR images. In particular, the need for this solution arises from the problem that in IGRT SRT/SRS QA processes, the analysis is still manually performed by a medical physicist operator due to two main factors: firstly, MV images are subjected to significant noise and low contrast resolution, because of the high dose emitted. In addition, this type of treatment is characterized by a single isocenter and multiple targets, a rather new irradiation technique within our institute, which still needs automatized verification tests.

This method has been compared with the manual process in terms of procedural delays. The manual method, whose measurements have been considered performed by an expert medical physicist, took approximately $25min$, while the automatic procedure required about $3min$, allowing a speed-up of 88%.

This process of automatic evaluation sits after the OBI registration phase in QA geometrical accuracy pipeline. It aims to be an end-to-end test for MV system as well as LINAC treatment head. In particular, the measured sphere displacements will represent misalignments between OBI and EPI systems or treatment couch correction problems, while irradiation field shifts could also depend on MLC or jaws mechanical calibration inaccuracies. It is a follow-up task to further investigate with specific tests and identify the source of error.

Keywords: Image-Guided Radiotherapy; LINAC; Digital-Reconstructed Radiographs; Electronic Portal Imaging; Image Analysis; DICOM.

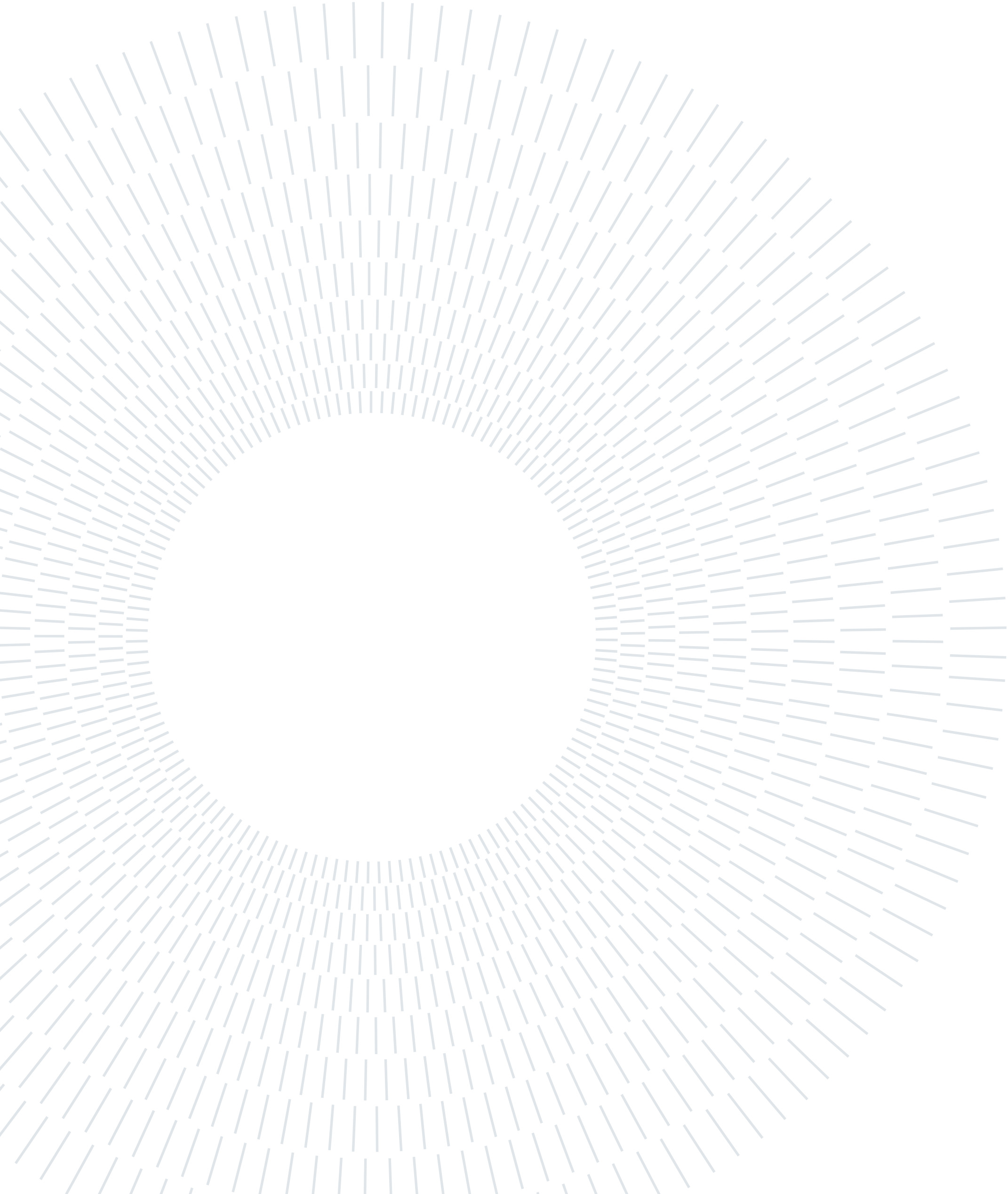

Sommario

Introduzione

La Radioterapia (RT), insieme alla chirurgia e alla chemioterapia, è una delle tre modalità principali utilizzate nel trattamento del cancro. Oggi, grazie all'avanzato sviluppo tecnologico delle apparecchiature di imaging, è stata introdotta la radioterapia guidata dalle immagini (IGRT). Essa consente di visualizzare l'anatomia del paziente poco prima dell'erogazione della frazione di radiazioni, permettendo di conoscere con precisione la posizione del volume da irradiare. L'IGRT è stata inoltre integrata con la Radioterapia Stereotassica (SRT) e la Radiochirurgia Stereotassica (SRS): questa combinazione di procedure rappresenta lo standard attuale per il trattamento di zone particolarmente sensibili e meno evidenti.

L'IGRT si basa sull'integrazione di due sistemi fondamentali di imaging nell'acceleratore lineare (LINAC): una sorgente kV di raggi X con il suo pannello di imaging, cioè l'On-Board Imaging (OBI), e una sorgente MV di raggi X con il rispettivo pannello di imaging, ovvero l'Electronic Portal Imaging (EPI). Entrambi sono utilizzati per valutare il posizionamento del paziente e hanno la possibilità di eseguire acquisizioni di volumi 2D e 3D; quest'ultimo rappresenta anche la sorgente di raggi X ad alta dose utilizzata per il trattamento effettivo del paziente. Una volta che un sistema di IGRT viene commissionato, è necessario eseguire verifiche periodiche di controllo qualità per garantire che i risultati dei trattamenti siano ottimali. In particolare, l'accuratezza geometrica ha lo scopo di verificare il set-up sia del paziente che dei fasci di raggi X.

Lo scopo di questa tesi è sviluppare un metodo automatico per valutare gli allineamenti di bersagli multipli (volti a simulare metastasi distribuite) all'interno di un phantom cranico e dei fasci di irradiazione del Multi-Leaf Collimator (MLC) in trattamenti a singolo isocentro, a seguito di una precedente registrazione tramite il sistema OBI. La necessità di questo compito nasce dal problema che l'analisi delle immagini MV, a causa del basso contrasto del soggetto e del basso rapporto

segnale/rumore, viene ancora eseguita a mano. Pertanto, è necessario un processo automatizzato. In particolare, questo metodo esegue l'analisi e il confronto di radiografie digitali ricostruite (DRR) e immagini MV (Portal images), garantendo un'accuratezza sub-millimetrica e una velocizzazione dell'88% rispetto agli attuali processi di controllo qualità, i quali prevedono misurazioni geometriche eseguite manualmente.

Metodi

L'intero processo si basa su quattro coppie di immagini 2D, in cui ogni coppia è caratterizzata da un'immagine DRR e da un'immagine Portal che rappresentano diverse proiezioni del phantom cranico, ovvero la vista anteriore, laterale sinistra, laterale destra e posteriore (0°, 90°, 180° e 270° di rotazione del gantry angle). Le immagini DRR sono generate virtualmente dal sistema di pianificazione del trattamento (TPS) e rappresentano la verità di base in termini di posizionamento del volume. Le immagini Portal, invece, sono acquisite attraverso il sistema EPI al momento del trattamento e idealmente dovrebbero matchare le DRR corrispondenti in un trattamento perfetto.

Inizialmente, le immagini sono state preparate leggendo il formato DICOM originale e trasformando i valori dei pixel, affidandosi alle funzioni di Pydicom, un toolkit Python per l'analisi delle immagini DICOM ampiamente utilizzato in ambito accademico e industriale. Questo primo step ci ha permesso di passare dai valori grezzi dei pixel ai valori di Hounsfield Unit (HU) di tipo *float64*. La seconda fase prevede il ricampionamento per le immagini DRR. Poiché le immagini DRR e Portal sono state generate considerando distanze diverse tra le sorgenti e le immagini (SID), rispettivamente $1000mm$ e $1500mm$, e diversi valori di pixel spacing, (0,9765625, 0,9765625) e (0,784, 0,784) rispettivamente, è stato necessario portarle sullo stesso piano (SID) per poterle confrontare geometricamente. Questo è stato fatto eseguendo un ricampionamento per le immagini DRR considerando il valore di pixel spacing che le immagini Portal avrebbero avuto se fossero state generate con un SID di $1000mm$. Il processo di ricampionamento si è basato sui metodi di SimpleITK. Successivamente, è stata implementata la fase di windowing sia per le immagini DRR che per quelle Portal, calcolando i valori ottimali di Window Width (WW) e di Window Level (WL), in modo che tutte le sfere target fossero chiaramente visibili in tutte le immagini e che tutti gli elementi superflui fossero filtrati. Ciò è stato fatto personalizzando gli intervalli HU su cui vengono visualizzate le immagini. Di conseguenza, risulta necessario uno step finale di standardizzazione secondo la grayscale 0-255.

La fase successiva consiste nell'esecuzione di un up-scaling dell'immagine, aumentando la risoluzione dell'immagine di un fattore x8. Questa operazione è stata eseguita attraverso l'interpolazione dell'immagine e una specifica Generative Adversarial Network (GAN). In questo modo, il valore del pixel spacing assume un valore molto più piccolo, consentendo misurazioni più accurate delle distanze. Successivamente, l'obiettivo è stato quello di isolare le diverse sfere target in ogni immagine per facilitare il riconoscimento automatico delle forme. Abbiamo quindi implementato un metodo attraverso il quale l'operatore, grazie a un'interfaccia grafica, è in grado di disegnare dei bounding-box approssimativi intorno a ciascuna sfera sulle immagini Portal. Dai crops estratti, abbiamo poi effettuato il riconoscimento della forma della sfera attraverso l'Hough Transform. Le coordinate salvate di ciascun crop sono state poi traslate sulle immagini DRR, dove è stato implementato il padding dell'immagine e il riconoscimento della forma della sfera è stato eseguito una seconda volta. A questo punto si è proceduto a misurare gli spostamenti tra le sfere corrispondenti in tutte le immagini accoppiate.

La fase finale riguarda i campi di irradiazione MLC. I campi teorici delle immagini DRR sono stati ricostruiti analizzando le informazioni dell'header DICOM, dove sono presenti tutte le informazioni necessarie sulle immagini appartenenti al piano di trattamento. Per questo scopo ci siamo ancora affidati a Pydicom. I campi di irradiazione delle immagini Portal, invece, sono stati sono stati calcolati con una sequenza di thresholding, blurring e Canny Edge detection, considerando le approssimazioni dovute all'effetto penombra. Anche in questo caso, la fase successiva consiste nel misurare gli spostamenti tra ogni campo di irradiazione corrispondente intorno a ciascun bersaglio sulle immagini DRR e Portal.

Risultati e Discussione

Il primo obiettivo è quello di quantificare gli spostamenti tra le sfere corrispondenti nelle immagini DRR e nelle immagini Portal. A questo scopo, abbiamo adottato la distanza euclidea in coordinate pixel (convertita poi in millimetri) su immagini 2D per valutare gli spostamenti dei centri delle sfere identificate.

In primo luogo, per verificare l'efficacia dell'algoritmo di identificazione della forma, abbiamo confrontato le coordinate dei centri delle sfere individuate nelle immagini DRR e Portal con i centri localizzati manualmente da un operatore esperto in fisica medica attraverso 3D Slicer, un pacchetto software open-source ampiamente utilizzato in questo settore. Le differenze tra i due metodi di identificazione per ciascun centro di sfera nelle immagini DRR non ha mai superato il valore di 0,3mm. In particolare, sono risultati valori medi di 0,20395mm per l'immagine ANT, 0,197mm per l'immagine LAT D, 0,198725mm per l'immagine LAT G e 0,21185mm per l'immagine POST, considerando tutte le sfere. Questi risultati dipendono certamente dall'elevato contrasto che caratterizza le immagini DRR e che facilita l'identificazione dei centri delle sfere sia per il metodo implementato da noi che per l'operazione manuale. Per quanto riguarda le immagini Portal abbiamo registrato valori medi di 0,229525mm per l'immagine ANT, 0,289525mm per l'immagine LAT D, 0,285275mm per l'immagine LAT G e 0,38435mm per l'immagine POST. Le differenze tra i due metodi sono ancora buone ma un po' più alte rispetto al caso precedente, soprattutto a causa del minore rapporto segnale/rumore e degli artefatti che caratterizzano le immagini Portal.

Successivamente, abbiamo eseguito il calcolo degli spostamenti tra le sfere corrispondenti. Gli spostamenti rappresentano l'accuratezza della fase di registrazione e l'allineamento tra i sistemi EPI e OBI. Abbiamo valutato questi spostamenti prima considerando i risultati ottenuti con il nostro metodo di identificazione, e poi considerando l'identificazione manuale. Gli spostamenti sono stati misurati di nuovo attraverso la distanza euclidea 2D delle coordinate pixel per ogni coppia di sfere in immagini DRR e Portal sovrapposte. Considerando il nostro metodo di identificazione, abbiamo registrato spostamenti medi di 0,5356mm per la sfera 1, 0,7152mm per la sfera 2, 0,5864mm per la sfera 3 e 0,4959mm per la sfera 4. Con l'identificazione manuale, abbiamo registrato 0,6169mm per la sfera 1, 0,7247mm per la sfera 2, 0,7084mm per la sfera 3 e 0,5063mm per la sfera 4 come valori medi. Questi risultati mostrano come i due metodi di identificazione non differiscano significativamente e che la fase di registrazione, insieme all'allineamento dei sistemi EPI e OBI, sono accurati, rigorosamente al di sotto di sotto della soglia di 1,5mm, anche tenendo conto delle incertezze dovute ai diversi metodi.

Per quanto riguarda i campi di irradiazione, il principio è lo stesso. Le coppie di corrispondenti campi di irradiazione, appartenenti a sfere accoppiate, sono state sovrapposte e le loro distanze sono state calcolate. In questo caso abbiamo considerato le coordinate ricostruite dai tag DICOM come campi di irradiazione veritieri e le coordinate identificate dal nostro metodo di identificazione come campi di irradiazione rilevati. In questo caso, gli spostamenti sono stati valutati sui quattro lati di ogni campo di irradiazione, dove la soglia da non superare è ancora di 1,5mm. Gli spostamenti dei lati sono stati calcolati considerando il valore massimo tra le differenze delle coppie di coordinate degli estremi per ciascun lato. In generale, tutti gli spostamenti rientrano nella soglia desiderata. Ci sono alcuni picchi di 1,3327mm e 1,2543mm, mentre tutti gli altri casi rimangono al di sotto di 1mm. Inoltre, confrontando i due metodi, abbiamo registrato come non c'è una differenza significativa tra i due, che ha portato a un massimo di 0,1252mm per il campo di irradiazione 2.

Infine, abbiamo confrontato le prestazioni dell'intero processo automatizzato attraverso il metodo sviluppato con il processo eseguito manualmente. Per quanto riguarda il processo manuale, abbiamo preso in considerazione l'esecuzione da parte di medici esperti e abbiamo preso i valori medi per ogni fase. È evidente che da un punto di vista computazionale la procedura eseguita dal nostro programma è molto più veloce del processo manuale, consentendoci di velocizzare l'intera pipeline di esecuzione dell'88%.

Conclusioni

In questo lavoro è stato sviluppato un nuovo metodo automatico per misurare gli spostamenti di più target di un phantom cranico e dei loro campi di irradiazione su immagini Portal 2D, rispetto alle loro posizioni teoriche nelle immagini DRR 2D. In particolare, la necessità di questa soluzione nasce dal problema che nei processi di QA di IGRT SRT/SRS l'analisi è ancora eseguita manualmente da un operatore di fisica medica, a causa di due fattori principali: in primo luogo, le immagini MV sono soggette a un rumore significativo e a una bassa risoluzione di contrasto, a causa dell'elevata dose emessa. Inoltre, questo tipo di trattamento è caratterizzato da un singolo isocentro e da bersagli multipli, una tecnica di irradiazione piuttosto nuova nel nostro istituto, che necessita ancora di test di verifica automatizzati.

Questo metodo è stato confrontato con il processo manuale in termini di ritardi procedurali. Il metodo manuale, le cui misurazioni sono state considerate eseguite da un fisico medico esperto, ha richiesto circa 25 minuti, mentre la procedura automatica ha richiesto circa 3 minuti, consentendo una velocizzazione dell'88%.

Questo processo di valutazione automatica si colloca dopo la fase di registrazione OBI nella pipeline di accuratezza geometrica QA. Si tratta di un test end-to-end per il sistema MV e per il LINAC. In particolare, gli spostamenti delle sfere misurati rappresenteranno disallineamenti tra i sistemi OBI ed EPI o problemi di correzione del lettino di trattamento, mentre gli spostamenti del campo di irradiazione potrebbero dipendere anche da imprecisioni nella calibrazione meccanica del MLC o delle ganasce. È un progetto da portare avanti, soprattuto l'ulteriore indagine con test

specifici per identificare la specifica fonte dell'errore.

Parole chiave: Image-Guided Radiotherapy; LINAC; Digital-Reconstructed Radiographs; Electronic Portal Imaging; Image Analysis; DICOM.

1 | Introduction

Radiotherapy (RT), together with surgery and chemotherapy, is one of the three main modalities used in the treatment of cancer. It uses ionizing radiations and heavily relies on modern technologies and the collaborative effort of several professionals, whose purpose is to constantly improve the outcome of the treatment [4]. Nowadays, thanks to the advanced technological development of radiotherapy procedures and imaging equipment, we are able to use techniques that lead to really precise and encouraging results, hardly conceivable until a few years ago.

A first step in this direction has been made by Three-Dimensional Conformal Radiotherapy (3D CRT), a technique capable of generating three-dimensional images of a patient's tumor and nearby organs and tissues. Subsequently, Intensity Modulated Radiotherapy (IMRT) followed, introducing the possibility of modulating and controlling the intensity of radiation beam in multiple small volumes. However, after the introduction of these two methodologies, the accuracy of dose delivery is still limited by uncertainty in target localization at the time of treatment. Movement of the target in both interfraction and intrafraction relative to reference landmarks, coupled with set-up errors and other inaccuracies, add to this uncertainty [4]. To mitigate that, the standard approach was to add margins to the target volume, usually at the expense of most of the potential benefits of the more precise treatment delivery techniques.

Only recently has Image-Guided Radiotherapy (IGRT) been introduced, thanks to which we are now able to image the patient's anatomy just prior to the delivery of a treatment radiation fraction, gaining accurate knowledge of the location of the target volume. This allows for reduced treatment margins, avoidance of geographical errors in X-ray beam delivery, increased dose, and generally fewer complications. IGRT technique has then been integrated with historical radiotherapy methodologies such as Stereotactic Radiotherapy (SRT) and Stereotactic Radiosurgery (SRS) on Linear Accelerator machines (LINACs) in order to obtain extremely accurate outcomes. Such a combination of procedures represents the actual standard for treating particularly sensitive and less-evident zones, especially very small lesions in the cranium.

IGRT procedures are based on the integration of two fundamental imaging systems, one constituted by a kV[1] X-ray source with the corresponding flat panel detector, and the second by an MV[2] source with the respective flat panel detector called Electronic Portal Image Device (EPID). The first imaging system is denominated On-Board Imaging (OBI) and it is additionally attached to the gantry of the LINAC, while the MV system, called Electronic Portal Imaging (EPI), is part of the LINAC itself. Both of them have the possibility to perform 2D radiographic acquisitions, by projecting the 3D irradiated volume on the correspondent flat panel, and 3D Cone Beam Computed Tomographies (CBCTs) by rotating around the LINAC isocenter. The difference between the two systems lies in the voltage at which radiations are emitted from each source: in the first case between 1 and $3mGy$, while in the second around 30-$70mGy$. The kV imaging system is generally used for patient positioning, thanks to its low dose radiation dose capable of obtaining high-contrast images. The MV system, on the other hand, represents the system through which high-dose X-rays are emitted for treating the patient. The latter has also the advantage that the beams come directly from the LINAC, thus no additional equipment is required to produce them.

In modern LINACs, in particular, the one that will be considered as the reference in this work, TrueBeam LINAC (Varian Medical Systems, Palo Alto, v. 2.5), both the above-mentioned imaging systems are integrated and can be used both mutually and in combination during a radiotherapy treatment in order to improve patient positioning accuracy.

Once an IGRT system is commissioned, it is necessary to perform quality assurance (QA) controls by periodically assessing that the image space used for guidance is representative of the treatment room geometry [6]. It follows that geometric calibration must be tested for validity and that the entire image guidance process must be checked, not only to assess its functionality but also to evaluate how tasks performed at one stage of the process affect the accuracy of subsequent stages. Specifically, these controls aim at verifying the precision of patient positioning and the edges of the beam field produced by the Multi-Leaf Collimator (MLC).

Several tests have been introduced in this direction. They can concern either the

---

[1] Kilovolt

[2] Megavolt

imaging systems independently or one in relation to the other (as in the case of Song Gao et al. [13] or Wendell Lutz et al. [23]). Also, they can be related to the treatment couch (as in J-L Dumas et al. [12]) or the gantry and collimator rotation (Laurence Court at al. [9]). Another possibility is linked to the mechanical isocenter (Sua Yoo et al. [33]) and the light field of the MLC (Ui-Jung Hwang et al. [19]). There are several variables involved, which make the QA process particularly complicated in identifying a potential source of error and extremely important in order to ensure effective treatments in terms of precision and correctness.

1.1. Motivations and Goal

In the past, patients with multiple brain metastasis were typically treated by whole-brain radiotherapy. However, this is no longer the customary treatment due to the associated deterioration in neurocognitive functions. Over the years, SRT and SRS integrated with IGRT have become the standard therapies for dealing with this type of cancer, adopting a multiple-isocenter approach, one distributed for each target in the area. Nevertheless, these procedures are not really advantageous in terms of both time consumption and dose delivery. Only recently, a new approach has emerged for treating multiple brain metastasis on LINACs with a single isocenter, thanks to the introduction of Volumetric Modulated Arc Therapy (VMAT).

This work takes place as the integration of two bigger research projects at Institut Curie (26 Rue d'Ulm, 75005 Paris, France), Department of Medical Physics [12] [15]. The first one proposes an end-to-end quality assurance method for 6DOF couches, IGRT systems, and for the repositioning of treatment beams in order to ensure submillimetric accuracy. It helps to assess the accuracy of single-isocenter stereotactic treatments and to improve the overall control of a TrueBeam LINAC when 6DOF rotations and translations are used. The second one, on the other side, compares the positioning accuracy between CBCT and ExacTrac (ETX) for a single-isocenter multiple target SRS on two TrueBeam systems.

The aim of this thesis is to develop a method for automatizing the analysis of images taken from TrueBeam LINAC and CT Siemens VA30, capable of calculating the geometric accuracy of positioning between correspondent multiple targets in Digital Reconstructed Radiographs (DRR) and Portal images as well as the MLC irradiation beam field accuracy, by performing multi-modal image super-impositions. In particular, it will contribute to QA processes replacing the actual standard according to which geometric measurements are manually performed by the medical physicist in charge. As will be explained in detail in the next chapter, the phase of QA workflow in which this control occurs, requires a preliminary positioning and alignment with the OBI imaging system. In this case, we will assume that the treatment couch as well as the OBI system are working properly and that the offset corrections for repositioning are reliable.

The evaluations have been done by imaging two phantoms. The first one is the ISO Cube Daily QA Phantom (Computerised Imaging Reference Systems Inc., Norfolk, VA, USA), characterized by two spherical radiopaque fiducials, one central and one off-center. The second, on the other hand, is an in-house head phantom with multiple spherical radiopaque fiducials, created by our institution. TrueBeam LINAC Portal images are acquired in both cases through the EPI system and considering the respective central sphere as the single-isocenter.

The need for this task stems from the problem that MV image analysis, due to low subject contrast and low signal-to-noise ratio inherent to imaging with high energy X-rays, is still performed by hand. An automatized process is needed, in particular with regard to single isocenter multi-target treatment images, which are rather recent in radiotherapy QA processes. Moreover, Portal images assume primary importance since they are those images generated with the effective treatment beams (MV), produced by the X-ray source and collimator. Portal imaging is thus directly correlated with verification of the treatment area with respect to the treatment beam edges. Therefore, an accurate control of the precision of this imaging system is strongly necessary.

1.2. Contributions

This dissertation involves three main disciplines, namely medicine, in the context of radiotherapy; medical physics, which enables the provision of appropriate radiotherapy services to support efficient and safe patient care; and finally, computer science. The goal of this last field is to create a tool that can measure geometrical displacements of the targets and MLC accuracy through image analysis and image processing techniques. It is exactly in the latter area that this thesis fits. The contribution is mainly to overcome the current QA control, which is time-consuming and manually performed, by providing an automatized version.

The general idea behind the whole measurement process consists of having 4 couples of 2D images (corresponding to different projections of the head phantom, namely anterior, left lateral, right lateral, and posterior), each characterized by a DRR and a Portal Image. The DRR image is automatically generated through the Treatment Planning System (TPS) by performing a virtual irradiation on the 3D CT volume image acquired from the CT Scanner. It represents the ground truth in terms of volume positioning and irradiation field and is the ideal image that should be performed on the LINAC during a therapy fraction, considering all the parameters set in the TPS. The second one instead, constitutes the correspondent real image acquired by the LINAC at the time of treatment, through the EPI system. All the coupled images show the irradiated volume from the same angulation.

With regard to the multiple spheres displacement evaluation, the objective is to identify the shapes of the spheres of the coupled DRR and Portal images (already aligned with the OBI in a preliminary step) and quantify the displacements between them. As previously specified, the recognized shapes in DRR images will represent the ground truth positions, and the recognized shapes in Portal images will be compared to them. With regard to the MLC accuracy, on the other side, the process is still the same: identifying the shape of irradiation fields of the coupled DRR and Portal Images, and evaluating the shifts. In this case, the ground truth irradiation fields are not recognized by image analysis but they are reconstructed from metadata coupled with DICOM files. In Portal images instead, the field is still recognized by image processing.

Let us see an overview of the pipeline adopted.

Initially, the images have been analyzed. This process is performed in parallel for the different couples of DRR and Portal images. The original images are provided in DICOM format, which is the international standard for storing, retrieving, and displaying medical imaging information. The images have been normalized, moving from the Hounsfield Unit (HU) representation space to grayscale (0-255).

Let's consider now the DRR images. Since DRR and Portal images, which will be discussed shortly, have been performed considering different Source to Image Distances (SID) - $1500mm$ and $1000mm$ respectively - and different pixel spacing values, it is necessary to bring them to the same plane and to the same pixel spacing value. This is done by rescaling DRR images, so as to obtain them directly comparable with Portal images. Detailed information will be given in Chapter 3. After that, the windowing phase is implemented in order to find optimal parameters for window width and window level such that all the spheres could be clearly visible in all the images. Image processing is then applied in order to remove noise and unnecessary artifacts.

The next stage consists in executing an image up-scaling, by increasing image resolution of a x8 factor. This is done through image interpolation and a specific Generative Adversarial Network (GAN). By performing this, the value of pixel spacing will assume a much smaller value, allowing us to execute more accurate distance measures. At this stage, the precision is preferred at the expense of a longer, but still acceptable computation time.

After that, the objective is to isolate the different spheres in each image in order to facilitate automatic shape recognition. Thereby, thanks to a GUI, the operator separates the spheres by drawing an approximate bounding box around them. The sphere shape recognition is achieved through the Canny Edge and Hough Transform methods. Finally, the MLC theoretical irradiation field is constructed on the image by analyzing the RT Plan DICOM file, where every necessary information about images belonging to the treatment plan is contained. As previously highlighted, these DRR metadata represent the reference to which the correspondent Portal images will be compared.

The same workflow just described is applied for the 2D Portal images, except for the initial rescaling (that will not be effectuated, since the SID distance is already the desired one) and for the identification of irradiation fields. The latter is not theoretically constructed from an RT Plan DICOM File, but it is identified from images by a combination of thresholding and Canny Edge techniques. In this case, the images are the real ones acquired by the EPI system of LINAC, thus the MLC fields and the positioning of the different balls are concretely reflected on images (ideally following the DRR). However, it is technically improbable that everything will coincide at the 100%, for this reason, the are several boundaries into which all shifts and uncertainties must fall by law. Portal images will reflect the mechanical or configuration problems we want to measure.

In particular, the shifts between corresponding identified spheres in DRR and Portal images will represent misalignments of EPI and OBI imaging systems or 6DOF couch problems. At the same time, the shifts between the corresponding irradiation fields will represent misalignments possibly caused by MLC problems. These calculations are performed after a 2D/2D multi-modal superimposition process among the couples of paired DRR and Portal images.

The metric adopted for the accuracy measurements is Target Registration Error (TRE), which is the quantitative distance between corresponding targets, particularly useful as a measure of how well the different modality images are matched. The measurements are performed in 2D/2D paired images and then reported in a 3D context thanks to the exploitation of height, width, and depth parameters.

1.3. Structure of the Thesis

The contents of this thesis are organized as follows. First of all, in Chapter 2 we give a general illustration of the context in which this work fits. In particular, a taxonomy will be defined together with a detailed description of the technologies involved in image acquisition processes. Secondly, we will see the typical workflow of a therapy session, its phases, and how they are connected to each other. This is particularly useful in order to comprehend how what has been described before is placed in space and time. After that, an overview of the quality assurance and image registration concepts is presented. In Chapter 3 we thoroughly analyze the work that has been done. A detailed description of the technologies used and the methods designed and adopted is faced, starting from the initial acquisition of images and their analysis. Here, theoretical concepts are paired with practical work so that a clear understanding can be achieved. Chapter 4 presents the experimental results of the methods described in Chapter 3. Finally, Chapter 5 and Chapter 6 contain the conclusions of the work and further perspectives for future contributions, respectively.

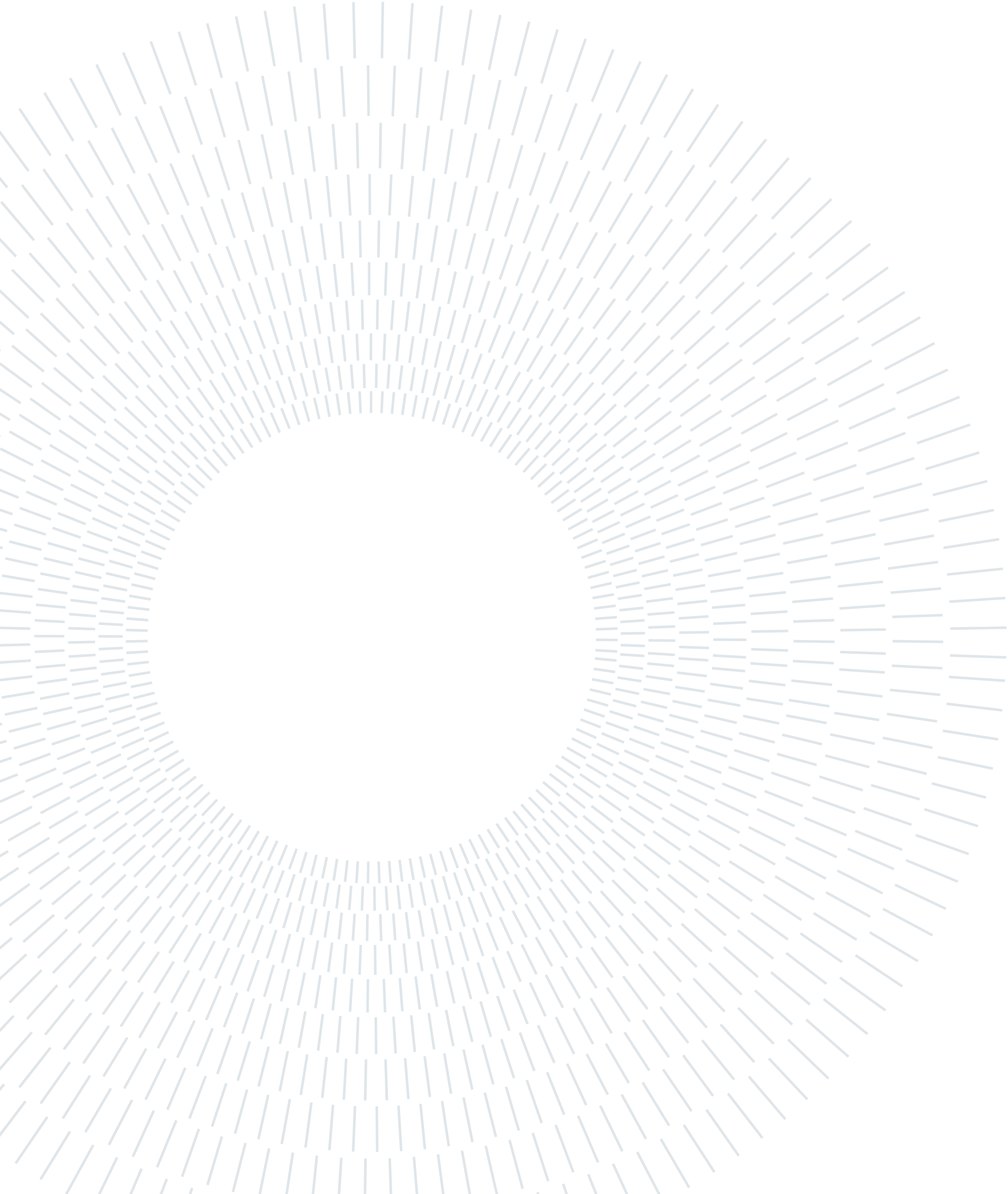

2 | Background

This chapter introduces the key concepts that represent the basis of the work presented in this thesis. They are necessary in order to properly comprehend the context and the steps that will be addressed later. First, we give some fundamental definitions and classifications, and we see the involved technologies. Secondly, we analyze in detail the routine of radiotherapy treatments and how the image acquisition process works. Finally, before concluding by reviewing the related work, we describe the concepts of quality assurance and image registration.

2.1. Radiotherapy

Radiotherapy (RT) is a medical treatment that exploits high-energy ionizing radiation to kill cancer cells and shrink tumors. The first main differentiation is between Internal Beam Radiotherapy (IBRT) and External Beam Radiotherapy (EBRT). The former is a treatment in which a solid or liquid source of radioactive material is put inside the patient's body in order to slowly release radiation over time, while the latter uses an external machine to deliver radiation beams to tumors with extreme precision. We will focus on the second one.

EBRT is the most common type of RT used for cancer treatment thanks to its capability of maximizing the radiation reaching cancer and limiting the damage to healthy tissue and nearby organs. A second classification can be made by considering which type of beam is used in the treatment:

- **Photon Beam Radiotherapy**. This is the most common approach utilized. The radiation is released by a linear accelerator (LINAC) and the emitted rays can be X-rays or gamma-rays. The energy of the rays is expressed in kilovolts (kV) or megavolts (MV) and typically, a lower amount of energy is used for treating superficial structures (e.g. skin cancer) while a higher one to treat deep-seated tumors (e.g. brain, prostate, lung). The amount of radiation used in photon beam RT is measured in grays (Gy) and it is defined as the absorption of one joule of radiation energy per kilogram of matter [24].

- **Particle Beam Radiotherapy**. This therapy involves the use of protons, neutrons, and heavier ions. The radiation is emitted by particle accelerators (e.g. cyclotron, synchrotron) as a stream of high-energy particles.
- **Electron Beam Radiotherapy**. Electron beams can be given from a LINAC or a particle accelerator and cannot travel very far through body tissues. This is the reason why they are most often used to treat cancers on the skin or near the surface of the body.

From now on we are going to take into consideration the photon beam radiotherapy as the standard and it will be considered implicit when we talk about EBRT.

Proceeding with the analysis of EBRT we find the following typologies:

- **Three-Dimensional Conformal Radiation Therapy** (**3D-CRT**). 3D-CRT represents the actual standard through which the external beams of RT are delivered from different angles to the interested zone by matching the shape of the tumor. To this end, it incorporates the use of imaging technologies to generate three-dimensional images of the patient's tumor and nearby organs and tissues. The imaging technologies that can be used to create the 3D scene are Computed Tomography (CT), Magnetic Resonance Imaging (MRI), Positron Emission Tomography (PET), or PET-CT.
- **Intensity-Modulated Radiotherapy** (**IMRT**). IMRT is an advanced type of 3D-CRT. The intensity of radiation beams can be adjusted across the treatment area in fractioned and separated beams with precision and accuracy. This allows stronger doses to get to certain parts of the tumor and helps lessen damage to nearby normal body tissues.
- **Image-Guided Radiotherapy** (**IGRT**). IGRT is a type of IMRT that overcomes the possible presence of missing lesions that are invisible on the planning scans with the previous method or that move between or during a treatment. In order to control this uncertainty IGRT combines real-time imaging with real-time adjustment of the therapeutic beams. The imaging equipment may be built into the LINAC or mounted nearby in the treatment room. Thanks to this the radiation oncologist is able to adjust the position of the patient or re-focus the radiation as needed to be sure that the radiation beams are focused exactly on the tumor and that exposure to normal tissues is limited.

- **Stereotactic Radiotherapy** (**SRT**). SRT is defined as a method of EBRT, in which a clearly defined target volume is treated with high precision and accuracy with a biologically high radiation dose in one single or a few fractions with locally curative intent [16]. SRT integrates the listed above techniques and, differently from the standard EBRT methods, it uses fewer treatment fractions. A fraction is when the full dose of radiation is split into a number of smaller doses given over days or weeks. In SRT there are fewer fractions but the dose of radiation is much higher with each fraction. Thanks to its ultra-focused radiation, this method is used in particular for very sensitive areas and small tumors (e.g. brain tumors).
- **Stereotactic Radiosurgery** (**SRS**). SRS is a particular case of SRT. While during SRT we have a fractionated treatment schedule, in SRS a single high dose of radiation is delivered to the tumors. Even if there is no cutting or incision involved at all, it's called radiosurgery since it is so exact in where it delivers the radiation beams, almost like how exact surgery can be.
- **Volumetric Modulated Arc Therapy** (**VMAT**). VMAT is an advanced radiotherapy technique that uses arcs of radiation, rather than individual beams used in other types of radiotherapy. As the LINAC moves, it automatically changes the beam shape and treatment dose, minimizing the dose to the organs surrounding the tumor. This makes the treatment much more targeted and accurate than single beam-based radiotherapy (like IMRT). In our case, it will be implemented by SRT and SRS.

Note that these typologies are not mutually exclusive when we talk about an RT treatment. They can be combined in order to exploit the advantages of each of them. In fact, the treatments considered in this study, are SRT and SRS integrated with IGRT and VMAT, using a single isocenter for multiple targets. These are the standards we will refer to from now on when we talk about SRT and SRS.

2.2. Technologies

In this section, we are going to illustrate the necessary hardware and software technologies involved during an SRT/SRS treatment.

- **CT scanner**. It is the machine through which CT scans are obtained. It uses a rotating X-ray tube and a row of detectors placed in a gantry in order to create 3D views of tissues and organs as a result of their X-ray absorption. The multiple X-ray measurements taken from different angles are processed on a computer to produce tomographic (cross-sectional) images (slices) of the body. In Figure 2.1b, we are able to observe how the CT system works: a motorized table moves the patient through a circular opening in the CT scanner image system; as the patient passes through the CT imaging system, the X-ray source performs a 360° rotation inside of the circular opening; the X-ray source produces a narrow, fan-shaped beam of X-rays used to irradiate a section of the patient's body; detectors, located on the opposite side of the patient with respect to the X-ray source, record the X-rays exiting the section of the patient's body being irradiated as a snapshot at one position (angle) of the X-ray source; several different snapshots are collected during one complete rotation; the data collected by the detectors are sent to a computer to reconstruct all of the individual snapshots into a cross-sectional image (slice) of the internal tissues and organs for each complete rotation of the X-ray source. In Figure 2.2, we can see an example of a multiple-slice sequence of the abdomen taken from the axial plane.

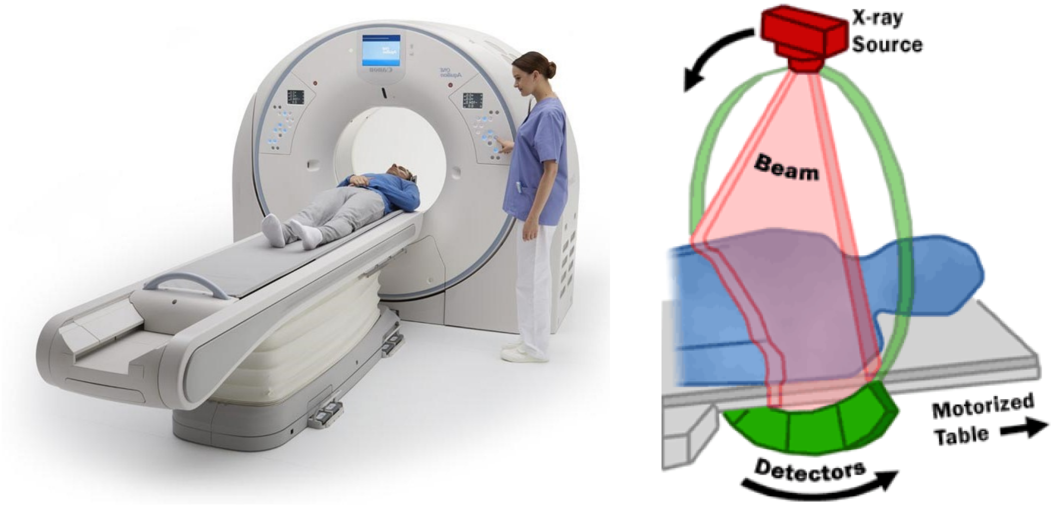

(a) CT scanner. (b) Functioning of the CT scanner.

Figure 2.1: Illustration of the CT scanner with the patient and the sanitary operator. Specific representation of the X-ray source and motorized table movements as well as irradiation beam field.

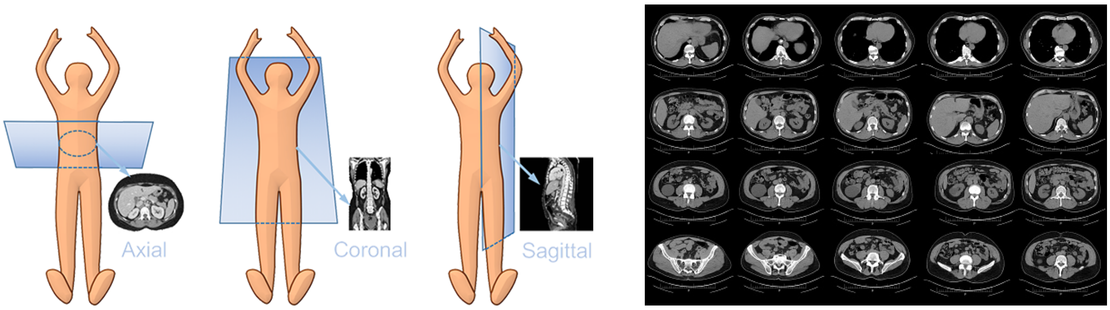

(a) CT planes. (b) Multiple axial abdomen slices.

Figure 2.2: Illustration of the CT planes (axial, coronal, and sagittal) and a sequence of multiple slices of the abdomen taken from the axial plane.

- **Treatment Planning System** (**TPS**). It is a software used in EBRT to generate beam shapes and dose distributions with the intent to maximize tumor control and minimize normal tissue complications [4]. Taking as input the CT scan of the patient, it is able to determine optimal beam arrangements, energies, field sizes, and ultimately fluence pattern to produce a safe and effective dose distribution performing a virtual simulation of the treatment irradiation under the choice and supervision of a medical physicist and a dosimetrist. All the configuration parameters will be then sent to the LINAC which will perform the real irradiation considering all these setting parameters. An example of TPS is depicted in Figure 2.3.

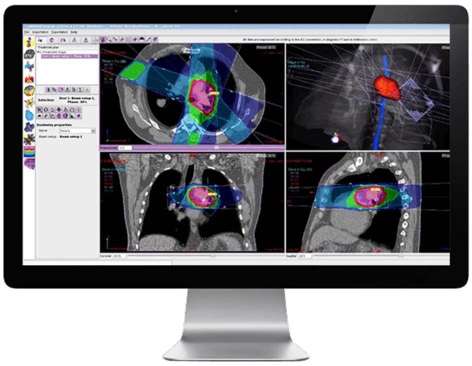

Figure 2.3: Treatment Planning System (TPS).

- **LINAC**. It is a device that uses high-frequency electromagnetic waves to accelerate charged particles to high energies through a linear tube (Figure 3.1a).

The principal components are the following (Figure 3.1b):

1. **Gantry**. The LINAC is mounted on a rotating gantry that allows to perform irradiation from multiple angles.
2. **Stand**. The stand connects the gantry to the treatment room floor and contains electronics and other systems required for LINAC operation.
3. **Treatment couch**. The couch supports and positions the patient during treatment. Modern couches are able to move along the x, y, and z-axis and can adjust patient roll, pitch, and yaw. For this reason, it is also called the 6 degrees of freedom (DOF) patient positioning system.
4. **Treatment head**. It is the principal section in which we are interested since it contains several components that influence the production, shaping, localizing, and monitoring of the clinical photon beams [4]. As we can see in Figure 2.5a, the important components found inside a treatment head include:
    (a) **Retractable X-ray target**.
    (b) **Flattening filter** (scattering filter). Clinical photon beams are produced by retracting the target and by flattening filter from the initial photon beam. Each clinical photon beam has its own target-flattening filter combination. The flattening filters are mounted on a rotating carousel or sliding drawer for ease of mechanical positioning into the beam, as required [4].
    (c) Primary collimator and secondary adjustable collimator (**Jaws**). The primary collimator is a conical opening machined into a tungsten shielding block and defines a maximum circular field. This field is then further truncated with an adjustable rectangular secondary collimator consisting of two upper and two lower independent jaws and producing rectangular and square fields at the LINAC isocentre [4].
    (d) **Multi-Leaf Collimator** (**MLC**). It is a beam-limiting device made of individual leaves that can move independently in and out of the path of an RT beam in order to shape it and vary its intensity. The beam exiting from the second collimator is additionally shaped by the MLC. In Figure 2.5b we are able to see the circular-like shape of a final beam given by the combination of the two collimators and

the MLC.

5. **Positioning systems**.
   (a) **Laser-based**. It is external to the LINAC and is used as the initial system of positioning. The laser-based system aims to display a coordinate system through three orthogonal laser beams forming corresponding planes. The intersection of these orthogonal planes corresponds to the LINAC isocenter. With three crossing points on the objective, the laser system can reposition a rigid body exactly [17].

   (b) **Image-based**. LINACs also incorporate imaging systems that are necessary for the verification of RT treatments and the correct positioning of the patient (see next section), as stated in the IGRT's previous definition. These IGRT systems may broadly be divided into radiation-based and non-radiation-based systems. We are interested in the first ones. Radiation-based systems exploit two X-ray sources that characterize the LINACs: MV X-ray source and kV X-ray source. The first one corresponds to the beam source inside the treatment head we described above, while the kV X-ray source is located orthogonally to the latter. Additionally, each of these sources has a flat-panel detector opposite and beyond the treatment couch, whose purpose is to acquire and measure the X-rays after absorption by the patient and reconstruct the image. We can see a representation in Figure 2.6a.

   The main radiation-based systems are:

      i. **Electronic Portal Imaging** (**EPI**). EPI is the system that exploits MV X-ray sources and Electronic Portal Imaging Devices (EPIDs). EPID is the technical name to define the mentioned flat-panel detector that is used to measure the X-ray intensity transmitted through a patient from a radiation source during a treatment session. The radiation signal is converted electronically into a 2D radiographic image to verify the correct beam placement in relation to the patient's anatomy [32]. The radiographic image will be in two dimensions since it consists of a single snapshot projection of a 3D volume on the flat-panel detector (see Figure 2.6b). The 2D portal images are acquired in a digital format that is amenable to computerized and distributed analysis. In EPI systems, the image contrast is really low due to the lack of low-energy components but there is less distortion from metallic implants (e.g. dental, and hip prostheses). The average dose per image is 30-70mGy [14].

ii. **On-Board Imaging** (**OBI**). OBI is the system that exploits kV X-ray source and its correspondent flat-panel detector. This system is attached to the gantry of the LINAC, orthogonally with respect to the EPI. The principle of working is the same as EPI with the only difference being that the X-ray source is less powerful in terms of voltage. This results in having higher contrast images, due to the inferior penetration in all tissues by X-ray beams. Furthermore, although it is always possible to make 2D images, with an average dose per image between 1 and 3mGy, OBI is also able to perform Cone Beam Computer Tomography (CBCT). CBCT is a volumetric radiographic imaging method that allows accurate, 3D imaging of hard tissue structures [20]. Via continuous partial or complete rotation of the LINAC gantry around the LINAC isocenter, multiple projection radiographs are acquired immediately before an RT fraction with acquisition times of 40 seconds to 2 minutes. The radiographs are reconstructed to a volumetric image with a back-projection algorithm[1], which takes several 2D image projections from different angles to produce the corresponding 3D resulting image. The average dose per image is 30-50mGy [14].

Many more imaging systems exist but they are out of the scope of this dissertation. To check them we suggest referring to the literature.

Note that one system does not exclude the other during the patient positioning routine. In most cases, the laser-based is used at first for an initial and approximate placement. However, since this system does not have a really accurate precision, the image-based one is secondly required for a more detailed and reliable evaluation.

---

[1] [22]

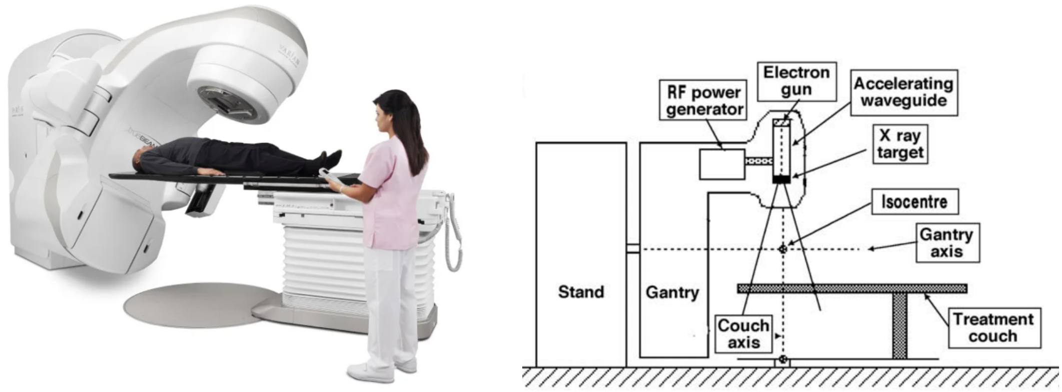

(a) LINAC. (b) LINAC components.

Figure 2.4: LINAC with the patient and the sanitary operator and LINAC components.

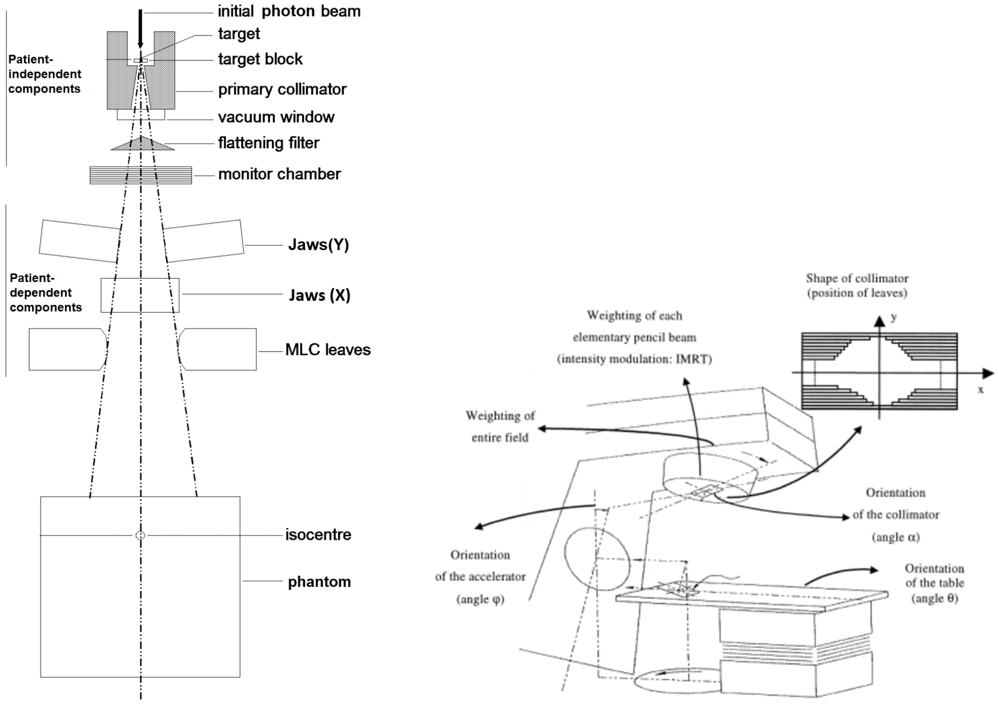

(a) LINAC treatment head. (b) Shape of the Multi-Leaf Collimator (MLC) and its irradiation field.

Figure 2.5: LINAC treatment head, shape of the MLC and its irradiation field.

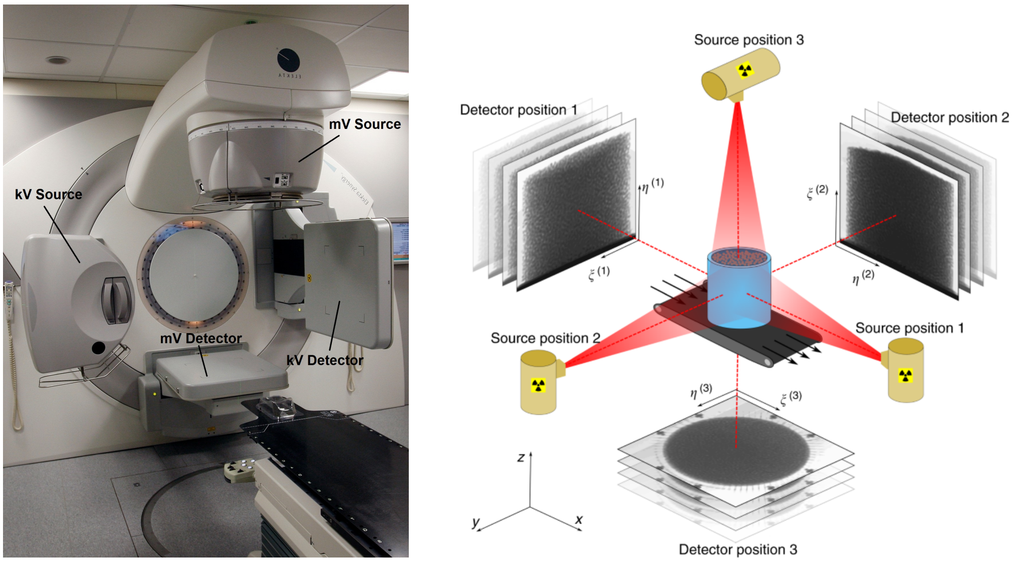

(a) LINAC kV and MV sources and their flat-panel detectors.

(b) 2D image projections of 3D volume.

Figure 2.6: LINAC kV and MV sources, flat-panel detectors and 2D projections of 3D volume.

2.3. Pipeline

In this section we describe the workflow of a standard SRT/SRS treatment, starting from the initial detection of the tumor until the last phase of the process, highlighting the different operators and imaging systems involved.

- **Treatment planning**

  After the possible diagnosis of a tumor, the patient is initially subjected to a CT scan in order to verify that. Here the treatment planning phase begins.

  1. Arrangement of the patient on CT scanner table with fixation. Performed by a radiation therapist.
  2. Checking of the patient's body comfort and adapting position based on patient needs. Performed by a radiation therapist.
  3. Scanning of the target. Performed by a radiation therapist.
  4. Sending CT images to TPS. Performed by a radiation therapist.

     In case a tumor is identified:

5. Delineation of Organs at Risk (OARs). OARs are the healthy tissues/organs placed near the Clinical Target Volume (CTV) whose irradiation could cause damage that would make changes to the radiotherapy treatment plan [25]. Performed by a radiation oncologist.
6. Delineation of target volumes. The first of these volumes is the position and extent of the primary tumor; this is known as the Gross Tumor Volume (GTV). The second volume surrounds the GTV and describes the extent of microscopic, un-imageable tumor spread; this is known as the Clinical Target Volume (CTV). Once these two volumes are established, the third volume, the Planning Target Volume (PTV), which allows for uncertainties in planning or delivery [7]. The latter is the volume that will be irradiated by the LINAC. Performed by a radiation oncologist.
7. Prescription of the dose. This process consists of calculating and deciding the ideal amount of radiation to be sent to the interested zone, based on the previous delineation. The objective is to design, generate, and measure radiation dose distributions and dose calculations. Performed by a radiation oncologist and a medical dosimetrist.
8. Creation of reference images. At this point, on the TPS, we are able to perform a virtual simulation of the real treatment that will be effectuated based on the parameters previously defined. During this simulation, Digitally Reconstructed Radiographs (DRRs) will be generated. They are a simulation of a conventional 2D X-ray image (as described in the EPID paragraph), performed on the CT 3D volume image. The basic approach to producing a DRR involves several steps, including, for example, the choice of beam virtual source position, the definition of the image plane, the definition of the treatment isocenter, and the track of rays from the beam virtual source to the image plane [4]. The DRRs represent the theoretical images we would like to achieve performing the real irradiation on the LINAC, this is the reason why from now on they will be considered as the reference images. Performed by a medical physicist.
9. Plan approval, plan check, and patient-specific quality assurance. Performed by a radiation oncologist and a medical physicist.

- **Treatment Delivery**

This phase occurs in a separate fraction with respect to the first CT scan session. The distance in time is decided by the radiation oncologist. Treatment delivery will be performed on the LINAC and will be carried out once in the case of SRS, or it will be reiterated multiple times in the case of SRT. Again the distance in time among each fraction will be decided by the radiation oncologist and may vary during the course of treatment. We draw attention to the fact that the treatment planning may be subject to change among each fraction. This could be caused for example by a different evolution of the tumor from the expectations requiring adaptations in the choice of parameters.

10. The patient is marked at the treatment isocenter (calculated at step 8) with radiopaque markers to capture a reference point in the image acquisition. Initial patient positioning with the laser system on the LINAC treatment couch based on the reference point. The position should be as close as possible to the position during the CT scan acquirement. In order to achieve that, the patient can be immobilized with the help of some special tools and is aligned with the LINAC laser system. Performed by a radiation therapist.

11. Image acquisition and image assessment (quality and gross displacements). In order to have a more accurate precision, the image-based system is being used. The images will be taken either with the OBI system (in 2D or in 3D with CBCT) or with the EPI system or even both of them. Performed by a radiation therapist.

12. Comparison with DRR image. Image registration, motion assessment, and quantification of 6 DOF treatment couch translations/rotations. Performed by a radiation therapist, radiation oncologist, and medical physicist.

13. Since the isocenter usually deviates from the reference point by scanning, it should be remarked before delivery. At this point online couch corrections are applied, repeating image acquisition as appropriate. It is imperative to ensure the accuracy of patient position and its reproducibility for fractionated treatments relative to the chosen IGRT device as well as treatment unit [14]. Performed by a radiation therapist, radiation oncologist, and medical physicist.

14. Treatment delivery, including intrafraction imaging as appropriate. The irradiation is based on the parameters set in TPS. These are transferred

to the system of the LINAC and checked by an apposite console. Note that the beam treatment dose is much higher than the beam dose for imaging. For SRT we usually have a range from 4000-5000mGy up to 11000mGy for each irradiation (at each fraction) while for SRS typically the beam treatment dose amounts up to 60000mGy. Performed by a radiation therapist.

15. Post-treatment imaging, as appropriate. Performed by a radiation therapist.

16. Subsequent off-line review and analysis of online obtained images, as appropriate. Performed by a radiation therapist.

An image representation of the described process is depicted in Figure 2.7.

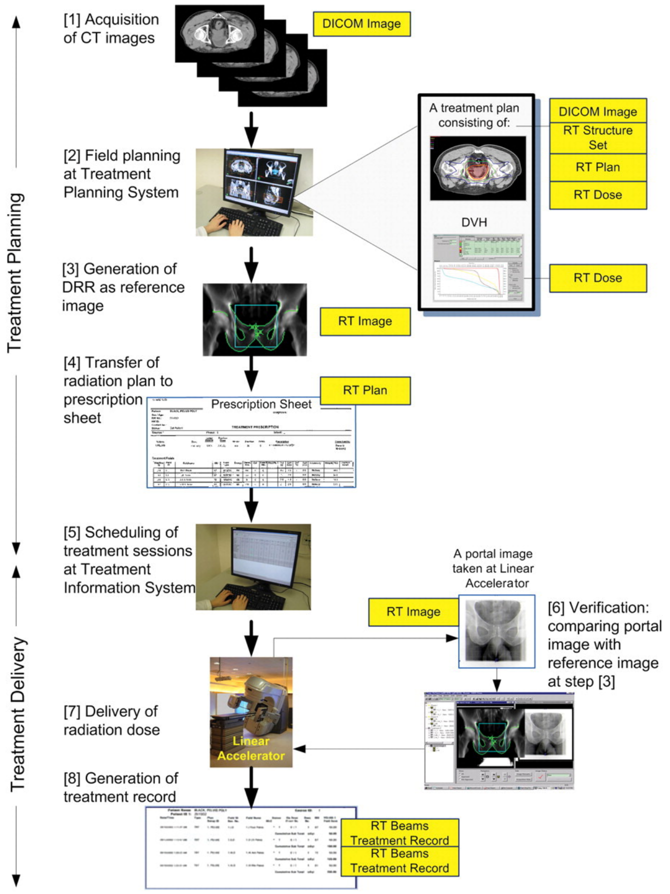

Figure 2.7: Standard SRT/SRS workflow.

2.4. Quality Assurance

In radiotherapy, Quality Assurance (QA) consists of all those procedures that ensure consistency of the medical prescription, and safe fulfillment of that prescription, as regards the dose to the target volume, together with minimal dose to normal tissue, minimal exposure of personnel and adequate patient monitoring aimed at determining the end result of the treatment. In order to guarantee that, regular activities and operational techniques are effectuated to check that quality requirements are met and to adjust and correct performance in case the requirements are not satisfied [4].

QA procedures improve geometric accuracy and precision of dose delivery, reducing the probability of accidents and errors occurring and increasing the likelihood that they will be recognized and rectified. QA procedures are necessary if we want improved technology and more complex treatments in modern radiotherapy to be fully exploited.

Considering the treatment delivery imaging system, there are five main quality assurance issue tests to take into account: safety/mechanical, image quality, imaging dosimetry, geometry, and IGRT software. Geometric accuracy is of extreme importance in determining the outcome of radiotherapy treatments. It can be influenced by uncertainties in a particular patient set-up, uncertainties in the beam set-up, and movements of the patient or the target volume during treatment [4].

In particular, set-up error is applied to describe the difference between real and predetermined therapy which includes systematic errors and random errors. The range of setup error is normally calculated as modifications of the treatment field when a Portal image is quantitatively compared to its reference image (DRR) [5]. This process is called image registration. Possible sources of error are incorrect placement of the patient in terms of anatomic and rotation, incorrect size, shape, and orientation of the field, and incorrect position of isocenters.

The purpose of this work is to assess the alignment of multiple targets and irradiation fields with respect to their ideal theoretical position through MV images obtained by the EPI system. In this way, we are able to evaluate the precision of the image registration and positioning processes performed at an early stage by the OBI imaging system. Any possible shift can be caused by several factors, for example, a misalignment between the EPI and OBI isocenters, couch rotation problems, or mechanical collimator leaf calibration. The idea is to perform an end-to-end test that could eventually identify problems at the first stage. It is a follow-up task to further investigate what might be the actual cause.

The image registration process is central in this routine since it allows to perform patient positioning before the irradiation treatment, as specified in steps 12) and 13) of the treatment delivery. To make image registration a routine process in clinical practice, one requires software that combines the functions of preparation of DRR and Portal images, image field edge and shapes detection, field edge matching, anatomy matching, and presentation of results [21]. Image registration is also always integrated into end-to-end geometric accuracy tests for IGRT processes. Tests of this type have been proposed for example by Jean-Pierre Bissonnette [6] and Sua Yoo et al. [33]. Such tests involve the following steps:

1. Placing a phantom with radio-opaque markers on the treatment couch by indicatively aligning it through the laser system.
2. Imaging the phantom with the OBI system.
3. Performing the registration in order to determine the shifts required from the comparison of the kV images to the DRR images of the phantom.
4. Applying the positional shift, with automated couch movement, and re-imaging the phantom.
5. Checking in the treatment room that the positional shift has been applied correctly.

This procedure is the one required for the study of displacement quantification for the multiple targets phantom. The contribution of this work is placed right after this procedure and will assume its correctness (previously evaluated). In particular, it will use MV images (already registered, indeed) acquired by the EPI system, comparing them to the corresponding DRR references.

To schematize, the whole process involves the following steps:

1. Placing the phantom with radio-opaque sphere markers on the treatment couch by indicatively aligning it through the laser system.
2. Imaging the phantom with the OBI system obtaining kV-CBCT 3D volume images.

3. Performing the registration in order to determine the shifts required from the comparison of the kV-CBCT images to the DRR images of the phantom.
4. Applying the positional shift, with automated couch movements. The couch movements are assumed reliable.
5. Re-imaging the phantom with the EPI system. The technique used is VMAT considering a single isocenter. We will obtain 2D Portal images as projections of the volume from different angles.
6. For each Portal image, evaluate the shifts of the sphere markers by comparing them to their corresponding theoretical position in the 2D DRR image. The same process is applied to evaluating the shifts between irradiation fields around each sphere marker. In the first case, the shifts might correspond to misalignment between OBI and EPI system isocenters or couch rotation problems. In the second case, instead, the shifts might be caused by mechanical problems of the MLC, or by gantry rotation.

In particular, the target of this thesis is to develop a program in order to automatize the process of step 6.

3 | Materials and Methods

This chapter will present a detailed description of the technologies used and the methods designed and adopted. The chapter will be structured as follows. The first section introduces the materials, in particular the phantoms, the treatment planning, and the setup conditions under which the project has been developed. Then, we will analyze the concrete implementation of the program, starting from image analysis, passing through shape recognition, to shift measurement. Before the description of each implemented functionality, its theoretical concept will be introduced and faced in order to give a clear understanding of the entire project.

3.1. Materials

3.1.1. Phantoms

Head Phantom

The phantom represents an anthropomorphic head phantom. It is divided into horizontal slides because, between them, 7 spherical 5-mm diameter steel ball bearings (BBs) have been placed by experts in order to represent seven distributed lesions. For simplicity, the locations have been chosen such that there is no overlap among them from each of the axial, coronal, and sagittal planes during the image acquisition phase. Notice that in this case the BBs have been positioned by hand at random positions without knowing ground truth positions and distances among them. This is coherent with respect to the case of a patient with internal lesions when we don't know in advance their positions and distances since the aim is to estimate them.

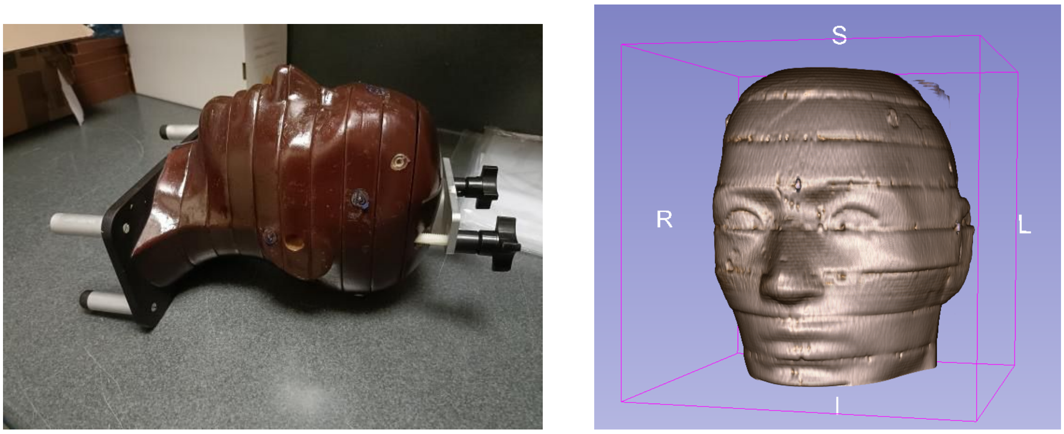

(a) Head Phantom located on LINAC.

(b) Head Phantom 3D reconstruction on 3D Slicer 5.0.3 .

Figure 3.1: Head Phantom and its 3D rendering reconstruction from CT scan on 3D Slicer 5.0.3.

ISO Cube Phantom

ISO Cube™ Daily QA Phantom CIRS Model 023[1] is a cost-effective and accurate tool used for several checks in the QA protocols. The ISO Cube contains a unique center point fiducial and an offset target. Both of them measure $6.35mm$ in diameter and are made of ceramic. Figure 3.2 represents the external view of the phantom. Figure 3.3 shows the internal view, especially the displacement of the two targets and different perspectives from axial, coronal, and sagittal points of view. In particular, we can observe how the side of the ISO Cube is $120mm$ and how the distance between the two spheres is $15mm$ horizontally, $25mm$ vertically, and $20mm$ in depth if we consider the axial view. We will see later how this phantom has been used for having robust feedback about the effectiveness of the shape recognition algorithm since the two balls have a defined distance by construction.

---

[1] see https://www.cirsinc.com/products/radiation-therapy/daily-iso-phantom/

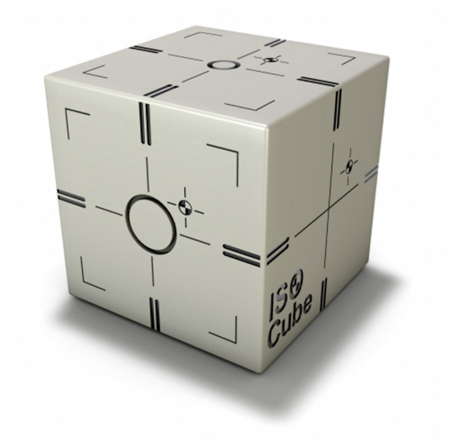

Figure 3.2: ISO Cube.

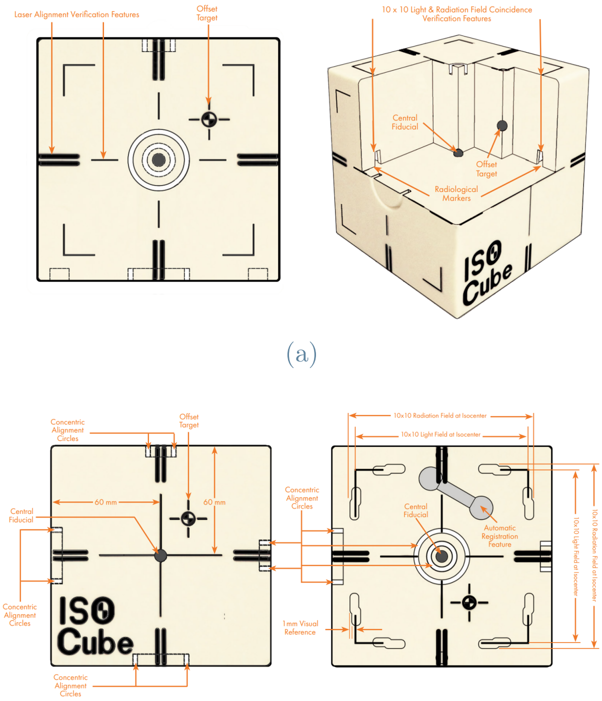

(a)

(b)

Figure 3.3: (a) Left sagittal view of the ISO Cube (left) and internal view of the ISO Cube (right). (b) Top coronal view of the ISO Cube (left) and front axial view of the ISO Cube (right).

3.1.2. Treatment Plan

This subsection aims to describe the treatment planning adopted for the experiment. In particular, it consists of a detailed illustration of all the set environments and parameters for the image acquisition processes. This is firstly done for the CT scan, in order to create a 3D representation of the phantom (this is clearly explained in the background chapter), and then for the MV image acquisitions on the LINAC. The second represents the process through which we obtain the images for the program we aim to develop. Before going into the description of the two set environments, we introduce the concept of the DICOM format.

The DICOM format (Digital Imaging and Communications in Medicine) is the international standard for medical images and related information. It defines the formats for medical images that can be exchanged with the data and quality necessary for clinical use [1]. With hundreds of thousands of medical imaging devices in use, DICOM is one of the most widely deployed healthcare messaging Standards in the world. DICOM differs from other image formats in that it groups information into data sets. A DICOM file consists of a header and image data sets, all packed into a single file [28]. We can see a representation in Figure 3.4. The first packets of the file constitute the header. It contains all information regarding the patient, acquisition parameters, image dimensions, environment setup, etc., and is organized as a constant and standardized series of tags. The header data information is encoded within the DICOM file so that it cannot be accidentally separated from the image data [28]. After the header, there is the packet that contains all the pixel-intensity data for the image. These data are stored as a long series of 0s and 1s, which can be reconstructed as the image by using the information from the header [28]. This sequence can represent either a single image, in the case of a single snapshot, or a sequence of images in the case of a multi-snapshot acquisition (as we will immediately see in the case of CT scan).

In order to open a DICOM file (.dcm), visualize the image(s) and read the header, specific software is needed. In this work, we used 3D Slicer 5.0.2 and MicroDicom Viewer 2022.1.

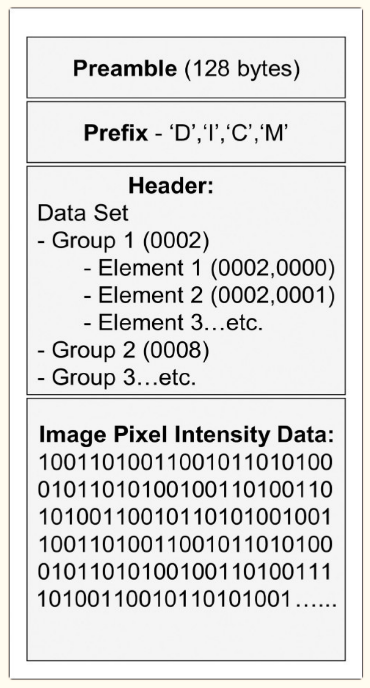

Figure 3.4: DICOM format.

CT Scan

As explained in the background chapter, the first phase of the entire pipeline is the CT scan acquisition in order to obtain a 3D representation of the patient (head phantom for us). In our case, this is done through a SOMATON Definition AS CT Scanner[2] from Siemens. The acquisition is taken having the head phantom placed on the table in the supine position, so looking at the ceiling. In particular, during the acquisition, the distance from the source of the rotating rays to the head phantom is 595mm and 106 snapshots are acquired. These are processed through the CT VB20A software and elaborated in the DICOM format. All this information, as explained before, is contained in the DICOM header, and in Table 3.1 there is a representation of some of the most meaningful tags.

(Group, Element)	**TAG Description**	**VR**	**VM**	**Length**	**Value**
(0002,0000)	File Meta Information Group Length	UL	1	4	186

---

[2] see https://www.siemens-healthineers.com/it/computed-tomography/single-source-ct/somatom-definition-as

(0002,0001)	File Meta Information Version	OB	1	2	00\01
(0008,0005)	Specific Character Set	CS	1	10	ISO_IR 192
(0008,0012)	Instance Creation Date	DA	1	8	20221003
(0008,0013)	Instance Creation Time	TM	1	6	091717
(0008,0020)	Study Date	DA	1	8	20220726
(0008,0022)	Acquisition Date	DA	1	8	20220726
(0008,0023)	Content Date	DA	1	8	20220726
(0008,0060)	Modality	CS	1	2	CT
(0008,0070)	Manufacturer	LO	1	8	SIEMENS
(0008,0080)	Institution Name	LO	1	22	Hopital Institut Curie
(0008,0081)	Institution Address	ST	1	32	Rue d'Ulm
(0008,1010)	Station Name	SH	1	10	CTAWP96293
(0008,1030)	Study Description	LO	1	24	Tête RT_CRANE (Adulte)
(0008,103E)	Series Description	LO	1	28	Crane ss IV 1.0 Hr38 iMAR
(0008,1070)	Operators Name	PN	1	14	Dumas Jean-Luc
(0008,1090)	Manufacturer Model Name	LO	1	22	SOMATOM Definition AS
(0008,1140)	Referenced Image Sequence	SQ	1	106	
(0010,0010)	Patient Name	PN	1	38	HEAD RESINE BILLES HEAD RESINE BILLES
(0010,0020)	Patient ID	LO	1	12	JLD_20220726
(0010,0030)	Patient Birth Date	DA	1	8	19000101
(0010,0032)	Patient Birth Time	TM	1	6	000000
(0010,0040)	Patient Sex	CS	1	2	O
(0018,0015)	Body Part Examined	CS	1	4	HEAD
(0018,0050)	Slice Thickness	DS	1	2	1
(0018,0060)	KVP	DS	1	4	120
(0018,0090)	Data Collection Diameter	DS	1	4	500

(0018,1000)	Device Serial Number	LO	1	6	96293
(0018,1020)	Software Versions	LO	1	14	syngo CT VB20A
(0018,1100)	Reconstruction Diameter	DS	1	4	500
(0018,1110)	Distance Source To Detector	DS	1	6	1085.6
(0018,1111)	Distance Source To Patient	DS	1	4	595
(0018,1120)	Gantry Detector Tilt	DS	1	2	0
(0018,1130)	Table Height	DS	1	4	269
(0018,1140)	Rotation Direction	CS	1	2	CW
(0018,1150)	Exposure Time	IS	1	4	1000
(0018,1151)	X Ray Tube Current	IS	1	4	124
(0018,1152)	Exposure	IS	1	4	225
(0018,1160)	Filter Type	SH	1	4	FLAT
(0018,1170)	Generator Power	IS	1	2	15
(0018,1190)	Focal Spots	DS	1	4	0.9
(0018,1210)	Convolution Kernel	SH	1	6	Hr38s
(0018,5100)	Patient Position	CS	1	4	HFS
(0018,9313)	Data Collection Center Patient	FD	3	24	0\-269\-139.5
(0008,0100)	Code Value	SH	1	6	113690
(0008,0102)	Coding Scheme Designator	SH	1	4	DCM
(0008,0104)	Code Meaning	LO	1	26	IEC Head Dosimetry Phantom
(0020,0010)	Study ID	SH	1	2	1
(0020,0011)	Series Number	IS	1	2	4
(0020,0012)	Acquisition Number	IS	1	2	3
(0020,0013)	Instance Number	IS	1	2	1
(0020,0032)	Image Position Patient	DS	3	34	-249.51171875\-518.51171875\-139.5
(0020,0037)	Image Orientation Patient	DS	6	12	1\0\0\0\1\0

(0020,1041)	Slice Location	DS	1	6	-139.5
(0020,4000)	Image Comments	LT	1	16	SANS IV
(0028,0002)	Samples Per Pixel	US	1	2	1
(0028,0004)	Photometric Interpretation	CS	1	12	MONOCHROME2
(0028,0010)	Rows	US	1	2	512
(0028,0011)	Columns	US	1	2	512
(0028,0030)	Pixel Spacing	DS	2	20	0.9765625\0.9765625
(0028,0100)	Bits Allocated	US	1	2	16
(0028,0101)	Bits Stored	US	1	2	12
(0028,0102)	High Bit	US	1	2	11
(0028,1050)	Window Center	DS	1	2	35
(0028,1051)	Window Width	DS	1	2	80
(0028,1052)	Rescale Intercept	DS	1	6	-1000
(0028,1053)	Rescale Slope	DS	1	2	1
(0028,1054)	Rescale Type	LO	1	2	HU
(3253,0010)	Private Creator	LO	1	34	Varian Medical Systems VISION 3253

Table 3.1: CT Scan DICOM Tags.

DRR Images

Afterward, still referring to the pipeline scheme of the background chapter, the DICOM file of the scanned volume is imported into the Treatment Planning System (Eclipse Varian[3] in our case) where the study of the dosimetry, the delineation of target volumes and organs at risk are effectuated by the radiation oncologist. More importantly, at this stage, we have the generation of DRR images (still under the DICOM format), which will represent our ground truth images. For the current work, the following image acquisition environment has been set up:

---

[3] see https://www.varian.com/products/radiotherapy/treatment-planning/eclipse

Gantry Angle Rotation	**Image Name**
0°	ANT
90°	LAT G
180°	POST
270°	LAT D

Table 3.2: Image Acquisition Gantry Angles.

This means that 4 DRR images will be generated from the TPS performing a virtual irradiation of the 3D head phantom volume, considering 4 different angles of the X-ray beam source. These angles will be 0° (hence considering the beam source vertically on top of the head phantom - coronal view), 90° (hence considering the beam source horizontally at the right of the head phantom - sagittal view), 180° (hence considering the beam source vertically at the bottom of the head phantom - coronal view), and 270° (hence considering the beam source horizontally at the left of the head phantom - sagittal view). These images will be named ANT (Anterior), LAT G (Lateral Gauche), LAT D (Lateral Droit), and POST (Posterior), respectively. This setup has been chosen in order to get a simplified representation of the problem by having 4 equally spaced angles of the entire volume. This will make easier the reconstruction of 3D measurements from 2D perspectives. Notice that in a real situation, the gantry angles might not be perfect as in this case due to the fact that they are chosen based on the best perspective from which the treatment of the target volume is more effective. In Figure 3.5 we can see the 4 DRR cropped images (originally 512x512 each) extracted from the correspondent DICOM files.

(a) ANT - Gantry 0°. (b) LAT G - Gantry 90°.

(c) LAT D - Gantry 270°. (d) POST - Gantry 180°.

Figure 3.5: DRR images from the 4 different gantry angle rotations.

Notice that we can clearly see the 7 different balls randomly positioned inside the head phantom. Moreover, it is extremely important the following fact. During the DRR image generation phase, the radiation oncologist outlines on the TPS the target volumes that he aims to treat. He performs this by tracking and drawing Regions Of Interest (ROIs) around the target spheres, on the 3D reconstructed head phantom volume. The shape of these ROIs will be the ones that during the effective treatment phase, the MLC of the LINAC must model in order to perform the irradiation. In this case, 4 of these 7 random balls have been chosen as target volumes to test the program. The important fact is that during the DRR image generation process, the information about ROIs is kept in the header of correspondent DICOM files and it is not visually deductible from the images themselves. So, DRR DICOM images show the entire head phantom volume, but the header of the files contains the information (and we will see later in which way) that tells us which are the balls we aim to treat during the LINAC irradiation session.

In Table 3.3 we can see the most representative Tags from the header of the DRR ANT DICOM file.

(Group, Element)	TAG Description	VR	VM	Length	Value
(0002,0000)	File Meta Information Group Length	UL	1	4	190
(0002,0001)	File Meta Information Version	OB	1	2	00\01
(0002,0010)	Transfer Syntax UID	UI	1	18	1.2.840.10008.1.2 (Implicit VR Endian)
(0002,0012)	Implementation Class UID	UI	1	24	1.2.246.352.70.2.1.160.3
(0002,0013)	Implementation Version Name	SH	1	8	DCIE 2.2
(0008,0005)	Specific Character Set	CS	1	10	ISO_IR 192
(0008,0008)	Image Type	CS	3	22	DERIVED \SECONDARY \DRR
(0008,0012)	Instance Creation Date	DA	1	8	20230310
(0008,0013)	Instance Creation Time	TM	1	6	162959
(0008,0060)	Modality	CS	1	8	RTIMAGE
(0008,0064)	Conversion Type	CS	1	4	WSD
(0008,0070)	Manufacturer	LO	1	22	Varian Medical Systems
(0008,1090)	Manufacturer Model Name	LO	1	12	ARIA RadOnc
(0008,0100)	Code Value	SH	1	6	113100
(0008,0102)	Coding Scheme Designator	SH	1	4	DCM
(0018,1020)	Software Versions	LO	1	6	15.6.8
(0018,5100)	Patient Position	CS	1	4	HFS
(0028,0002)	Samples Per Pixel	US	1	2	1
(0028,0004)	Photometric Interpretation	CS	1	12	MONOCHROME2
(0028,0010)	Rows	US	1	2	512
(0028,0011)	Columns	US	1	2	512
(0028,0100)	Bits Allocated	US	1	2	16

(0028,0101)	Bits Stored	US	1	2	16
(0028,0102)	High Bit	US	1	2	15
(0028,0103)	Pixel Representation	US	1	2	0
(0028,0303)	Longitudinal Temporal Information Modified	CS	1	8	REMOVED
(0028,1050)	Window Center	DS	1	6	15000
(0028,1051)	Window Width	DS	1	6	30000
(0028,1052)	Rescale Intercept	DS	1	2	0
(0028,1053)	Rescale Slope	DS	1	2	1
(0028,1054)	Rescale Type	LO	1	2	US
(3002,0002)	RT Image Label	SH	1	12	ANT MLC2-DRR
(3002,000A)	Reported Values Origin	CS	1	8	OPERATOR
(3002,000C)	RT Image Plane	CS	1	6	NORMAL
(3002,000D)	X Ray Image Receptor Translation	DS	3	6	0 \0 \0
(3002,000E)	X Ray Image Receptor Angle	DS	1	2	0
(3002,0010)	RT Image Orientation	DS	6	12	1 \0 \0 \0 \-1 \0
(3002,0011)	Image Plane Pixel Spacing	DS	2	20	0.9765625 \0.9765625
(3002,0012)	RT Image Position	DS	2	26	-249.51171875\249.51171875
(3002,0020)	Radiation Machine Name	SH	1	6	LINAC1
(3002,0022)	Radiation Machine SAD	DS	1	4	1000
(3002,0026)	RT Image SID	DS	1	4	1000
(3002,0030)	Exposure Sequence	SQ	1	168	
(FFFE,E000)	Item	1	160		
(0008,1160)	Referenced Frame Number	IS	1	2	1
(3002,0032)	Meterset Exposure	DS	1	2	0
(300A,00B6)	Beam Limiting Device Sequence	SQ	1	92	

(300A,00B8)	RT Beam Limiting Device Type	CS	1	6	ASYMX
(300A,00BC)	Number Of Leaf Jaw Pairs	IS	1	2	1
(300A,011C)	Leaf Jaw Positions	DS	2	6	-45 \41
(300A,00B8)	RT Beam Limiting Device Type	CS	1	6	ASYMY
(300A,00BC)	Number Of Leaf Jaw Pairs	IS	1	2	1
(300A,011C)	Leaf Jaw Positions	DS	2	6	-43 \61
(300A,00F0)	Number Of Blocks	IS	1	2	0
(300A,011E)	Gantry Angle	DS	1	2	0
(300A,0120)	Beam Limiting Device Angle	DS	1	2	0
(300A,0122)	Patient Support Angle	DS	1	2	0
(300A,00B3)	Primary Dosimeter Unit	CS	1	6	MINUTE
(300A,012C)	Isocenter Position	DS	3	50	4.99514716680466 \-306.35928706481 \0.1478465231009
(300C,0002)	Referenced RT Plan Sequence	SQ	1	108	

Table 3.3: DRR ANT DICOM Tags.

Portal Images

At this stage, still following the pipeline description of the background chapter, we need to perform the irradiation of the head phantom on the LINAC. As explained in the other chapter, the phantom is positioned on the table of the LINAC, and beam irradiation is performed with the EPI system after the positioning through the OBI system. The planning for irradiation will follow the one designed in the previous stage for DRR images generation, where we have theoretical positions and targets to follow. So basically the idea is to perform 4 acquisitions of the head phantom from the same angles, shooting the target spheres previously designed (the 4 chosen spheres).

Here is important to recall that the technique used in this work makes use of a single isocenter. This means that one of the spheres is designed as the treatment center, the EPI system is aligned on that, and during the acquisition of the 4 images at different gantry angles, the treatment center sphere will always be at the same location. This will result in having that sphere at the center of each of the 4 different Portal Images.

In Images 3.6, 3.7, 3.8, 3.9 we can see the 4 spheres chosen as target volumes on the DRR images (where the information about the ROIs is kept in the DICOM header) and the correspondent Portal images. It is important here to highlight the fact that in Portal images, we concretely see the reflection of the chosen ROIs for the target spheres during the TPS phase. These shapes are modeled by the MLC of the LINAC, which is able to define custom shapes thanks to its leaves, as explained in the background chapter. Moreover, notice that for simplicity these ROIs have been chosen as simple rectangles around each target sphere. This is an assumption that we made in order to simplify our reconstruction and measurements. In reality, during effective treatment operations, these shapes can assume the most varied form, depending on how they have been modeled by the operator.

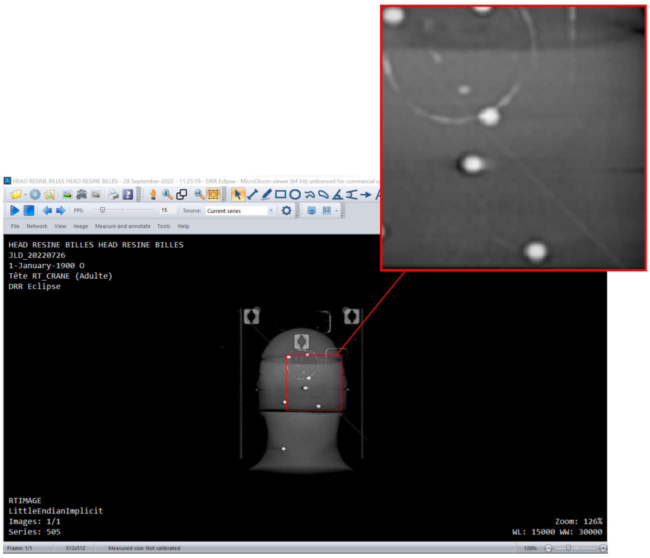

HEAD RESINE BILLES HEAD RESINE BILLES - 28-September-2022 - 11:25:19 - DRR Eclipse - MicroDicom viewer (64 bit) unlicensed for commercial u

HEAD RESINE BILLES HEAD RESINE BILLES
JLD_20220726
1-January-1900 O
Tête RT_CRANE (Adulte)
DRR Eclipse

RTIMAGE
LittleEndianImplicit
Images: 1/1
Series: 505

Zoom: 126%
WL: 15000 WW: 30000

Frame: 1/1
512x512
Measured size: Not calibrated
126%

(a) DRR ANT Image zooming on the 4 target spheres.

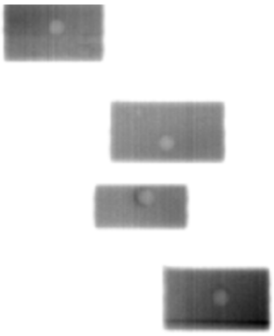

(b) Portal Image ANT.

Figure 3.6: Illustration of the DRR ANT Image with a zoom on the 4 target spheres (a) and the correspondent Portal Image obtained from the EPI system on LINAC (b).

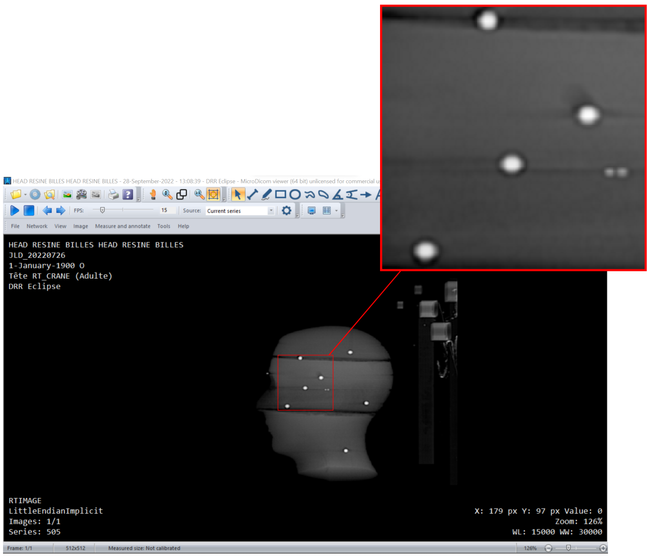

```
HEAD RESINE BILLES HEAD RESINE BILLES
JLD_20220726
1-January-1900 O
Tête RT_CRANE (Adulte)
DRR Eclipse

RTIMAGE
LittleEndianImplicit
Images: 1/1
Series: 505

X: 179 px Y: 97 px Value: 0
Zoom: 126%
WL: 15000 WW: 30000
```

(a) DRR LAT G Image zooming on the 4 target spheres.

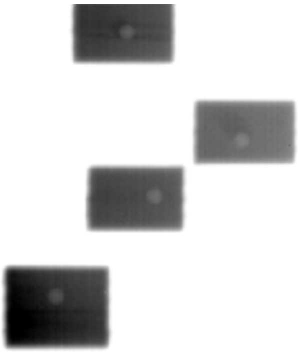

(b) Portal Image LAT G.

Figure 3.7: Illustration of the DRR LAT G Image with a zoom on the 4 target spheres (a) and the correspondent Portal Image obtained from the EPI system on LINAC (b).

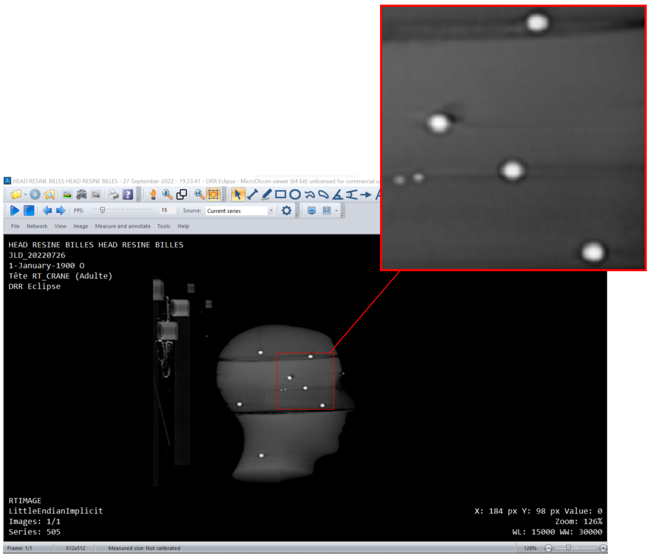

```
HEAD RESINE BILLES HEAD RESINE BILLES
JLD_20220726
1-January-1900 O
Tête RT_CRANE (Adulte)
DRR Eclipse

RTIMAGE
LittleEndianImplicit
Images: 1/1
Series: 505

X: 184 px Y: 98 px Value: 0
Zoom: 126%
WL: 15000 WW: 30000

Measured size: Not calibrated
```

(a) DRR LAT D Image zooming on the 4 target spheres.

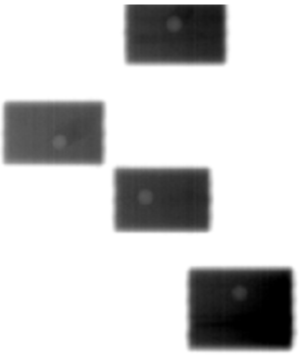

(b) Portal Image LAT D.

Figure 3.8: Illustration of the DRR LAT D Image with a zoom on the 4 target spheres (a) and the correspondent Portal Image obtained from the EPI system on LINAC (b).

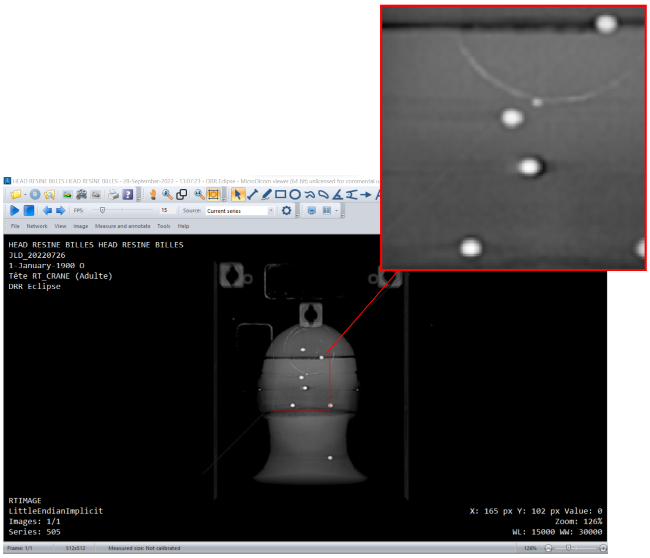
HEAD RESINE BILLES HEAD RESINE BILLES - 28-September-2022 - 13:07:23 - DRR Eclipse - MicroDicom viewer (64 bit) unlicensed for commercial u

FPS: 15
Source: Current series

HEAD RESINE BILLES HEAD RESINE BILLES
JLD_20220726
1-January-1900 O
Tête RT_CRANE (Adulte)
DRR Eclipse

RTIMAGE
LittleEndianImplicit
Images: 1/1
Series: 505

X: 165 px Y: 102 px Value: 0
Zoom: 126%
WL: 15000 WW: 30000

Frame: 1/1
512x512
Measured size: Not calibrated
126%

(a) DRR POST Image zooming on the 4 target spheres.

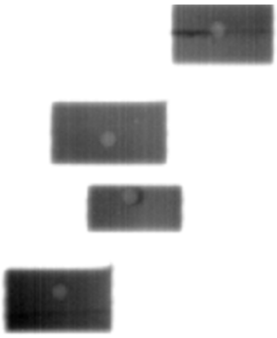

(b) Portal Image POST.

Figure 3.9: Illustration of the DRR POST Image with a zoom on the 4 target spheres (a) and the correspondent Portal Image obtained from the EPI system on LINAC (b).

(Group, Element)	**TAG Description**	**VR**	**VM**	**Length**	**Value**
(0002,0000)	File Meta Information Group Length	UL	1	4	190
(0002,0001)	File Meta Information Version	OB	1	2	00\01

(0002,0013)	Implementation Version Name	SH	1	8	DCIE 2.2
(0008,0005)	Specific Character Set	CS	1	10	ISO_IR 192
(0008,0008)	Image Type	CS	3	24	ORIGINAL\PRIMARY\PORTAL
(0008,0012)	Instance Creation Date	DA	1	8	20230310
(0008,0013)	Instance Creation Time	TM	1	6	114705
(0008,0016)	SOP Class UID	UI	1	30	1.2.840.10008.5.1.4.1.1.481.1
(0008,0060)	Modality	CS	1	8	RTIMAGE
(0008,0064)	Conversion Type	CS	1	2	DI
(0008,0070)	Manufacturer	LO	1	22	Varian Medical Systems
(0008,1090)	Manufacturer Model Name	LO	1	20	Patient Verification
(0012,0063)	Deidentification Method	LO	1	62	De-identified with Varian Medical Systems DICOM Import Export
(0008,0100)	Code Value	SH	1	6	113100
(0008,0102)	Coding Scheme Designator	SH	1	4	DCM
(0008,0104)	Code Meaning	LO	1	42	Basic Application Confidentiality Profile
(0018,1020)	Software Versions	LO	1	8	2.24.0.0
(0018,5100)	Patient Position	CS	1	4	HFS
(0028,0002)	Samples Per Pixel	US	1	2	1
(0028,0004)	Photometric Interpretation	CS	1	12	MONOCHROME2
(0028,0010)	Rows	US	1	2	384
(0028,0011)	Columns	US	1	2	512
(0028,0100)	Bits Allocated	US	1	2	16
(0028,0101)	Bits Stored	US	1	2	16
(0028,0102)	High Bit	US	1	2	15
(0028,0103)	Pixel Representation	US	1	2	0
(0028,1040)	Pixel Intensity Relationship	CS	1	4	LIN
(0028,1041)	Pixel Intensity Relationship Sign	SS	1	2	-1

(0028,1050)	Window Center	DS	1	6	64935
(0028,1051)	Window Width	DS	1	4	803
(0028,1052)	Rescale Intercept	DS	1	2	0
(0028,1053)	Rescale Slope	DS	1	2	1
(0028,1054)	Rescale Type	LO	1	2	US
(3002,0002)	RT Image Label	SH	1	8	MV_0_0a
(3002,0004)	RT Image Description	ST	1	272	6x [MV], 600 [MU/min]
(3002,000A)	Reported Values Origin	CS	1	6	ACTUAL
(3002,000C)	RT Image Plane	CS	1	6	NORMAL
(3002,000D)	X Ray Image Receptor Translation	DS	3	50	0.00226162341957-0.0136117866631-500.05232936976
(3002,000E)	X Ray Image Receptor Angle	DS	1	2	0
(3002,0010)	RT Image Orientation	DS	6	12	1\0\0\0\-1\0
(3002,0011)	Image Plane Pixel Spacing	DS	2	12	0.784\0.784
(3002,0012)	RT Image Position	DS	2	16	-200.312\150.136
(3002,0020)	Radiation Machine Name	SH	1	6	LINAC1
(3002,0022)	Radiation Machine SAD	DS	1	4	1000
(3002,0026)	RT Image SID	DS	1	16	1500.05232936976
(3002,0029)	Fraction Number	IS	1	2	0
(0008,1160)	Referenced Frame Number	IS	1	2	1
(0018,0060)	KVP	DS	1	4	6000
(0018,1150)	Exposure Time	IS	1	4	398
(3002,0032)	Meterset Exposure	DS	1	16	1.5312563566638
(300A,00B8)	RT Beam Limiting Device Type	CS	1	6	ASYMX
(300A,00BC)	Number Of Leaf Jaw Pairs	IS	1	2	1
(300A,011C)	Leaf Jaw Positions	DS	2	34	-44.999964167379\41.0000624782342

(300A,00B8)	RT Beam Limiting Device Type	CS	1	6	ASYMY
(300A,011E)	Gantry Angle	DS	1	16	359.98672837168
(300A,0120)	Beam Limiting Device Angle	DS	1	16	0.00155520565716
(300A,0122)	Patient Support Angle	DS	1	12	359.94921875
(300A,0128)	Table Top Vertical Position	DS	1	16	-171.86720140152
(300A,0129)	Table Top Longitudinal Position	DS	1	16	779.437164052381
(300A,012A)	Table Top Lateral Position	DS	1	16	3.36400218519572
(300A,0140)	Table Top Pitch Angle	FL	1	4	359.37598
(300A,0144)	Table Top Roll Angle	FL	1	4	0.66177607
(300A,00B3)	Primary Dosimeter Unit	CS	1	2	MU
(300A,012C)	Isocenter Position	DS	3	6	0\0\0
(3273,0010)	Private Creator	LO	1	34	Varian Medical Systems VISION 3273

Table 3.4: Portal Image ANT DICOM Tags.

3.2. Methods

This section will be the most articulated part of the document. Here we will analyze the workflow that has been followed in order to implement the program, together with its technical details and theoretical concepts at its basis. We start by listing the technical tools that have been adopted, and then we move to the data-set preparation and preprocessing, before facing spheres recognition, MLC irradiation fields reconstruction, and their displacement measurements.

3.2.1. Tools

Programming Language	**Version**
Python	3.9.7

Table 3.5: Programming Language.

Library	**Version**
dicom2nifti	2.4.7
h5py	3.6.0
hdf5	1.10.6
keras	2.8.0
matplotlib	3.5.1
nibabel	3.2.2
numpy	1.20.3
opencv	4.5.2
pandas	1.4.1
pillow	9.0.1
pydicom	2.2.2
scikit-image	0.18.3
scikit-learn	1.0.2
scipy	1.7.3
simpleitk	2.2.1

Table 3.6: Libraries.

3.2.2. Dataset Preparation

DICOM Files Management

The original images, in DICOM format, have been placed in two folders, one for the DRRs - theoretical images - and one for the Portal images - LINAC acquired images. In this section, we will make the assumption that all the DICOM files belonging to DRR images and Portal images are processed together as a batch of images. So from now on, each command or execution has to be considered to be executed for all the DICOM files placed in the two folders.

In order to read DICOM files, the main library is *pydicom*[4], which makes it easier to read these complex files into natural pythonic structures for easy manipulation. With function *dcmread()*, we are wrapping the DICOM (.dcm) file inside a data-set object (ds in this case). The data-set object embeds the DICOM file content in a map-like structure, where each attribute with its content is indexed by the correspondent TAG.

```
ds = pydicom.dcmread(filename)
```

In the next piece of code we can see an example of dataset object structure:

```
>>> ds
Dataset.file_meta -------------------------------
(0002, 0000) File Meta Information Group Length  UL: 190
(0002, 0001) File Meta Information Version       OB: b’\x00\x01’
(0002, 0002) Media Storage SOP Class UID         UI: RT Image
   Storage
(0002, 0003) Media Storage SOP Instance UID      UI
   :1.2.246.352.221.558631713755189952613829384598186209471
(0002, 0010) Transfer Syntax UID                 UI: Implicit VR
   Little Endian
(0002, 0012) Implementation Class UID            UI:
   1.2.246.352.70.2.1.160.3
(0002, 0013) Implementation Version Name         SH: ’DCIE 2.2’
-------------------------------------------------
(0008, 0005) Specific Character Set              CS: ’ISO_IR 192’
(0008, 0008) Image Type                          CS: [’DERIVED’, ’
   SECONDARY’, ’DRR’]
...
```

We can see how the structure is similar to the one represented in Figure 3.4, where each entry is characterized by the following structure:

$$tag^{5} \quad TAG\_Description \quad VR^{6} \quad : value^{7} \tag{3.1}$$

In order to access the specific value of each entry, you can use the dot notation:

```
>>> Dataset_object.TAG_Description
```

---

[4] https://pydicom.github.io/pydicom/stable/index.html

Pixel Values Transformations

The most important attribute in this case is *pixel_array*, which will access the uncompressed pixel data of the image as a *numpy.ndarray*. As an example:

```
>>> Dataset_object.pixel_array
array([[175, 180, 166, ..., 203, 207, 216],
       [186, 183, 157, ..., 181, 190, 239],
       [184, 180, 171, ..., 152, 164, 235],
       ...,
       [906, 910, 923, ..., 922, 929, 927],
       [914, 954, 938, ..., 942, 925, 905],
       [959, 955, 916, ..., 911, 904, 909]], dtype=int16)
```

In this case, we see that DRR images have a shape of 512x512 and a *float64* dtype, while the Portal images have a shape of 384x512 and *float64* dtype.

However, these accessed values will represent raw pixel data values that need to be converted to a specific (and possibly unitless) physical quantity. As will be seen in this subsection, the original accessed pixel data will undergo different processes for pixel value transformation.

The physical quantity that we will consider is the Hounsfield Unit (HU). It is a relative quantitative measurement of radio density used by radiologists in the interpretation of CT images. The absorption/attenuation coefficient of radiation within a tissue is used during CT reconstruction to produce a grayscale image. The physical density of tissue is proportional to the absorption/attenuation of the X-ray beam [10]. In Figure 3.10 it is possible to catch some examples of HU values related to different types of matter.

In order to perform this conversion to HU, we adopt the *apply_modality_lut()* function. This first pixel value transformation operation is always applied when a data-set requires multiple grayscale transformations, as reported from the documentation. It allows the transformation of manufacturer-dependent pixel values into manufacturer-independent pixel values [3]. We apply it for both DRR and Portal images data.

```
arr = ds.pixel_array
hu = apply_modality_lut(arr, ds)
```

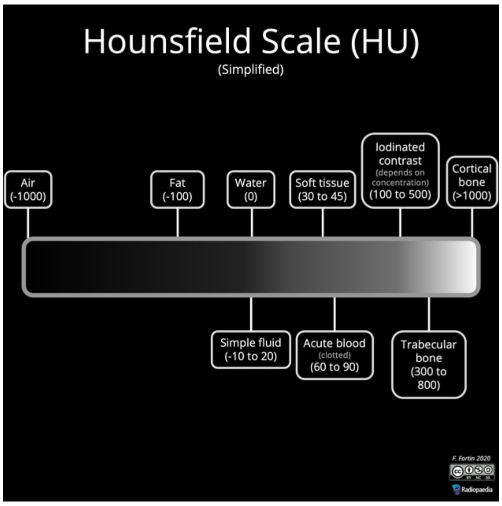

Figure 3.10: Hounsfield Unit.

At this point, two more concepts related to HU are necessary to be introduced: Window Width (WW) and Window Level (WL). The WW is the measure of the range of HUs (grayscale) that an image contains. A wider WW, therefore, will display a wider range of HUs. As a consequence, the transition of dark to light structures will occur over a larger transition area to that of a narrow WW. The WL instead is the midpoint of the range of the HUs displayed.

In particular, when presented with WW and WL, it is possible to perform the second pixel value operation using the function *apply_ voi_ lut()*.

```python
data_hu = apply_voi_lut(apply_modality_lut(ds.pixel_array,ds),ds)
```

This allows the transformation of the modality pixel values (output of the previous transformation) into pixel values that are meaningful for print or display. This operation is a linear function and operates as follows:

$$\begin{aligned} &\text{if } (x <= c - 0.5 - (w-1)/2), \text{then } y = y_{min} \\ &\text{else if } (x > c - 0.5 + (w-1)/2), \text{then } y = y_{max} \\ &\text{else } y = ((x - (c - 0.5))/(w-1) + 0.5) * (y_{max} - y_{min}) + y_{min} \end{aligned} \tag{3.2}$$

where x is the input value, y is the the output value that ranges from y_{min} to y_{min}, c is the WL, and w is the WW, as reported from [2].

It is important to remark that this transformation is applied only to Portal images: they are characterized by effective WW and WL values since they are generated from real irradiation and their values are meaningful for the display representation. On the other side, considering that DRR images are virtually generated images, the spectrum of their modality pixel values doesn't require to be windowed and centered, since it will consist of the complete range of values. Notice also that all this information is kept inside the header of each DICOM file. For example, just search at Table 3.4 for the correspondent values of window width and window center tags.

At this stage, we are able to work with our batches, one of DRR and one of Portal images.

```
>>> print(portal_images_batch.shape)
(4, 384, 512)
>>> print(drr_images_batch.shape)
(4, 512, 512)
```

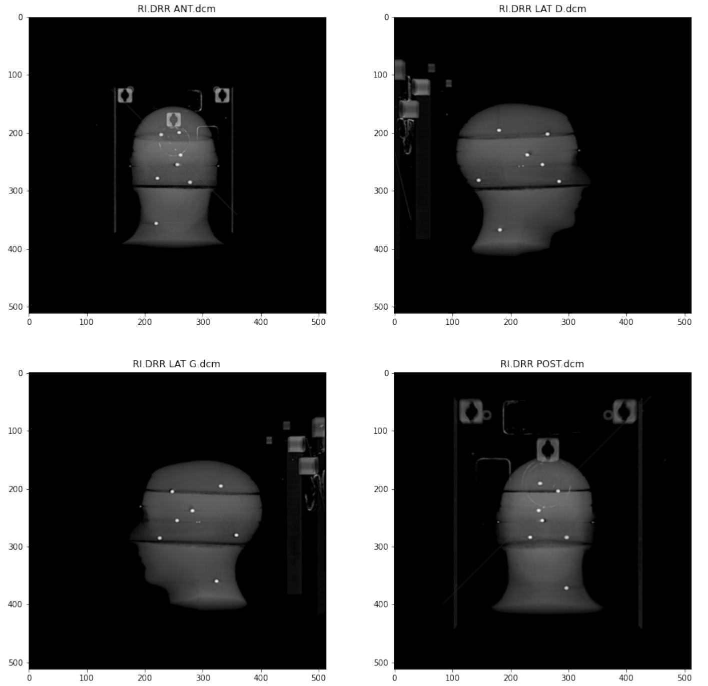

Figure 3.11: DRR images batch.

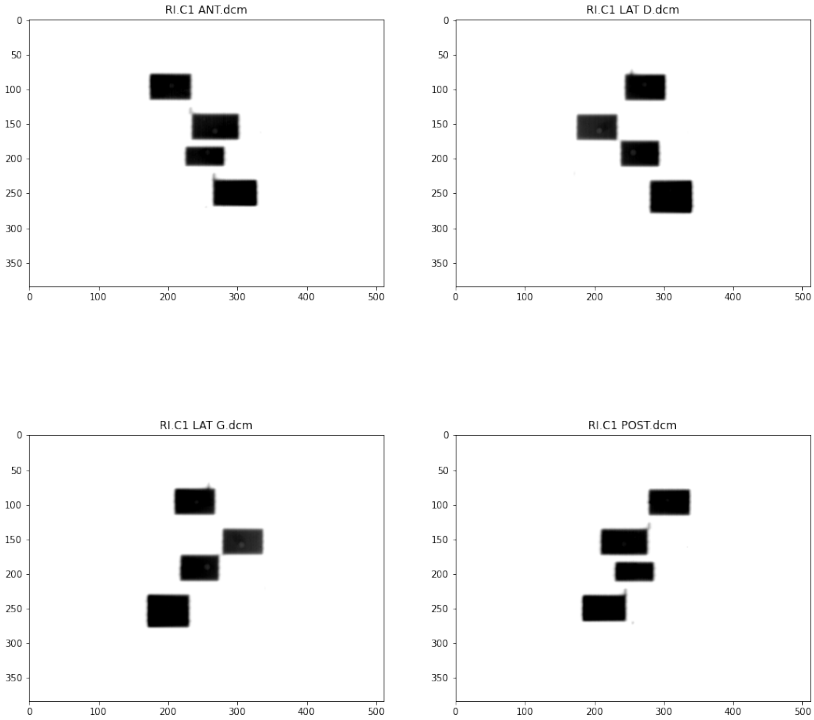

Figure 3.12: Portal images batch.

3.2.3. Preprocessing

The aim of the preprocessing phase is to improve the quality of images so that we can analyze them in a better way, according to our purposes. In our case, all the steps are applied for both DRR and Portal images batches, apart from the first step of resampling-pixel spacing, which is necessary to be applied only for DRR images, as we will immediately see. These steps comprehend windowing, which is used in order to enhance the essential spheres for our recognition, and superscaling, which increases the information content of images.

Resampling - Pixel Spacing

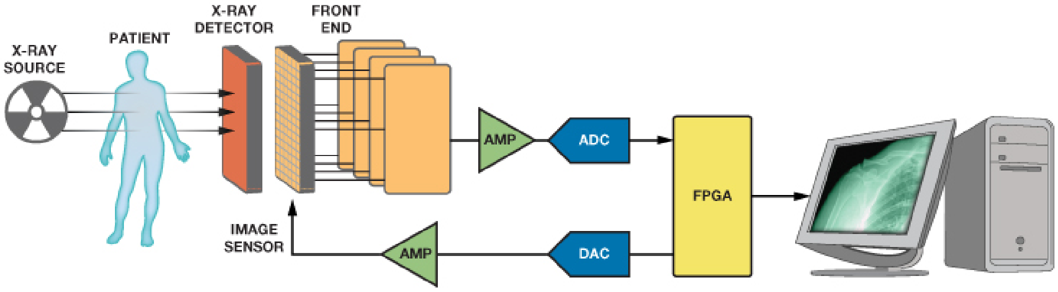

Figure 3.13: Image reconstruction process.

Before diving into the effective point, it is necessary to first introduce some technical concepts regarding the image reconstruction process. As we can see from Figure 3.13, the X-ray flat panel detector is responsible for the digital image reconstruction in conjunction with a film receptor and an analog-digital converter. If we then have a look at Figure 3.14, it is clear how the digital panel detector assumes a grid-like shape and how the irradiated body is then separated into small individual components. These samples are the voxels (volume elements) which are represented in the image by corresponding pixels (picture elements). Generally, each tissue voxel is represented by a specific pixel in the image. The face dimension of the voxel, which closely relates to the corresponding pixel, is determined by the ratio of two factors, the physical size of the imaged area, the field of view (FOV), and matrix size which is the number of voxels/pixels across each dimension of the image [26]. The FOV can be defined as the physical dimension of the area being imaged at the location within the body [26]. For what concerns the image matrix size, on the other side, most images are square matrices with equal dimensions in each direction with sizes that are binary multiples (such as 512x512, 1024x1024). However, there are still cases in which it is more convenient to use rectangular matrices. In our context, since we are working with 2D projection images, the pixel assumes the fundamental role. Its dimension depends on the ratio between FOV and image matrix size.

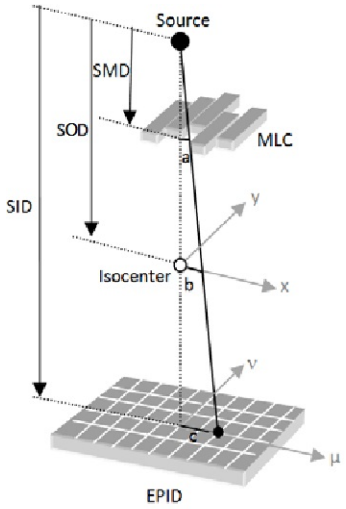

Figure 3.14: Flat panel detector.

In particular, a central concept that must be highlighted is pixel spacing. It is defined as the physical distance between the centers of each two-dimensional pixel, specified by two numeric values. The first value is the row spacing in *mm*, that is the spacing between the centers of adjacent rows, or vertical spacing. The second value is the column spacing in *mm*, that is the spacing between the centers of adjacent columns, or horizontal spacing. If we have a look at Figure 3.15a it is clearly understandable.

A second fundamental concept is magnification. This phenomenon occurs in X-ray imaging because the X-rays are divergent or spread out from the X-ray source. Therefore, the object will appear larger on the panel detector than the true object size. Magnification in radiotherapy is defined as (Image Size/Object Size) and is equal to the (SID/SOD) which is the Source to Image Distance divided by the Source to Object Distance (Figure 3.15b).

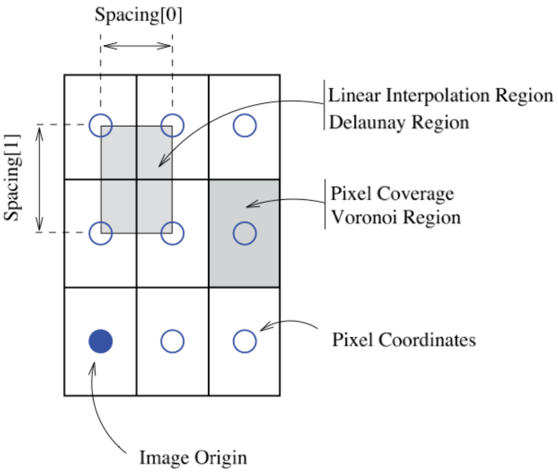

(a) Pixel spacing.

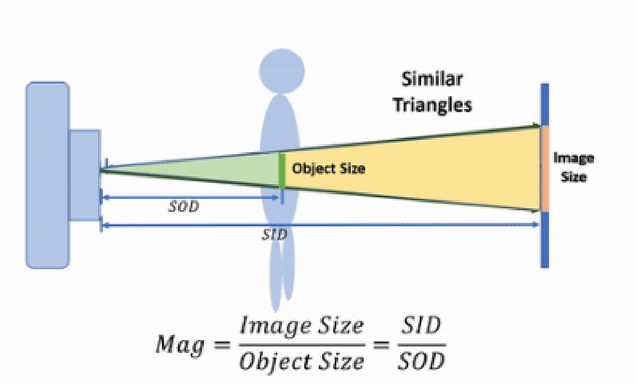

$$Mag = \frac{Image\ Size}{Object\ Size} = \frac{SID}{SOD}$$

(b) Magnification.

Figure 3.15: Pixel spacing and magnification.

At this point, we are able to proceed considering our case. If we look back at Tables 3.4 and 3.3, we can see in the DICOM tags how the DRR images and Portal Images have different values of Image Plane Pixel Spacing, in particular, it is (0.9765625, 0.9765625) for DRR images, and (0.784, 0.784) for Portal images. This means that the distances between two couples of pixels in the two types of images have a different physical meaning in mm, thus the DRRs and the Portal images are not comparable. Our aim is that the two types of images could be comparable, in order to perform measurements on them.

Why does this happen? If we look at the DICOM Tags of the images, we can see that the RT Image SID value is different. In particular, the DRR images have been virtually generated considering a Source-to-image distance of $1000mm$, while the actual Portal images have been taken with a Source-to-image distance of $1500mm$. This unavoidably implies a different magnification and a different value of pixel spacing. It is necessary to bring them to the same SID in order to be able to compare them. More specifically, we decided to bring the Portal images' SID value to the one of DRR images, obtaining a new value of pixel spacing (smaller). At this point, we recomputed the DRR images by using the new pixel spacing. In this way, the DRR images will get the dimensions that they would have if they were generated with the same pixel spacing as Portal images at the same SID. This operation is called resampling. By doing the opposite, thus evaluating the new pixel spacing for DRR images and applying it to Portal images, we would have obtained a reduction in the dimensions of Portal images, causing a loss of information which is preferable to avoid.

The first step is to compute the value of pixel spacing that the Portal images would have if taken at $1000mm$ (DRR SID). We consider the following equation:

$$\begin{gathered} Portal\ Image\ Pixel\ Spacing\ : Portal\ Image\ SID \\ = \\ New\ Portal\ Image\ Pixel\ Spacing\ : DRR\ Image\ SID \end{gathered} \tag{3.3}$$

By inverting the proportion, we can calculate the new value of pixel spacing for Portal images. Now, by exploiting the Simple ITK Library [8], we are able to perform the resampling of DRR images.

```python
def resize_image(itkImage, newSpacing, originSpacing,
   resampleMethod=sitk.sitkLinear):
    newSpacing = np.array(newSpacing, float)
    resampler = sitk.ResampleImageFilter()
    originSize = itkImage.GetSize()
    factor = originSpacing / newSpacing
    newSize = originSize * factor
    newSize = newSize.astype(int)
    resampler.SetReferenceImage(itkImage)
    resampler.SetOutputSpacing(newSpacing.tolist())
    resampler.SetSize(newSize.tolist())
    resampler.SetTransform(sitk.Transform(2, sitk.sitkIdentity))
```

---

[8] https://simpleitk.org/

```
    resampler.SetInterpolator(resampleMethod)
    itkImageResampled = resampler.Execute(itkImage)

    DRR_sitk_nifti_scaled_array = sitk.GetArrayFromImage(
   itkImageResampled)
    return DRR_sitk_nifti_scaled_array.squeeze(),
   itkImageResampled
```

Specifically, *newSpacing* corresponds to the newly computed value of Pixel Spacing and *originSpacing* to the original DRR Pixel Spacing. Notice that through this process we are simply performing a resampling of the DRR images considering a new Pixel Spacing. In particular, this upsampling is performed using Linear Interpolation, chosen in order to have a compromise between accuracy and computational efficiency.

At the end of this stage, by applying the upper function to the DRR batch, all the images will obtain a new shape:

```
>>> print(drr_images_resampled_batch.shape)
(4, 956, 956)
```

Windowing

The second step is windowing. As we introduced in the paragraph regarding pixel value transformations, we know that our DICOM images are characterized by two properties: Window Width (WW) and Window Level (WL). The objective in this phase is to find the right balance between the two of them in order to isolate as much as possible the spheres of interest, by filtering out all the unnecessary elements of images. These values may vary depending on the types of images. In our case, they were found by experiment.

If we recall, at the end of the pixel value transformation, our images were defined by their HU range and their specific values of WW and WL. By modifying the latter, we are introducing a grayscale transformation in the range of HU values, which needs to be reflected in the displayed image. We consider the following function:

```
def window_image(img, window_center, window_width, rescale=True):
    img_min = window_center - window_width / 2
    img_max = window_center + window_width / 2
    img[img<img_min] = img_min
    img[img>img_max] = img_max
    if rescale:
```

```
        img = (img - img_min) / (img_max - img_min) * 255.0
    return img
```

The first four lines are necessary in order to calculate the upper and lower gray levels i.e. values over the upper grey level will be white and values below the lower level will be black. In this way, we are able to customize the HU ranges over which our images are displayed. In the last line, we then simply perform a rescaling moving to the 0-255 grayscale, so that all the images are standardized.

Regarding the DRR images batch, we considered a window width of 20000 and a window level of 25000 for all the images, while for the Portal images batch, we added 300 to the window width and subtracted 450 from the window level for each image (since in this case all the images present different values from each other). In general, we can say that when we are looking at an area with predominantly different tissue densities, a wide window is used. If we have tissues with almost similar densities, we use a narrow window, and subtle changes in tissue density (small window) are magnified over the whole grayscale range. On the other side, when the Window Level is decreased the images will be brighter and vice versa.

In Figures 3.16 and 3.17, we are able to catch the effect of windowing operations on both batches of images.

On the left column, we have the images before windowing while on the right one, each correspondent image after the operation. Notice that for what concerns DRR images, on the left column, they have a 512x512 shape, while on the right one a 956x956 shape. This is because here it is not displayed the intermediate step we illustrated before for which DRR images are upsampled from 512x512 to 956x956. The shapes of Portal images remain the same since they are not affected by resampling.

Notice also that after this stage, in DRR images we removed the majority of tissue of the head phantom and almost only the spheres are visible. On the other side, Portal images clearly present the targeted balls in each irradiation field.

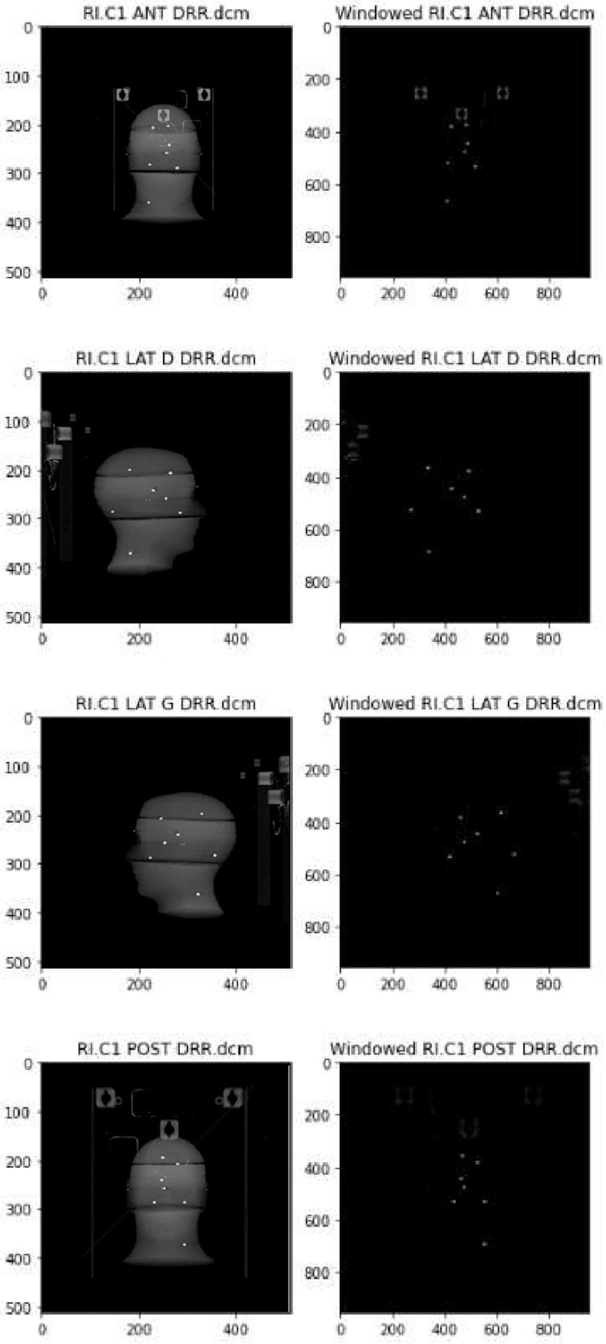

RI.C1 ANT DRR.dcm

Windowed RI.C1 ANT DRR.dcm

RI.C1 LAT D DRR.dcm

Windowed RI.C1 LAT D DRR.dcm

RI.C1 LAT G DRR.dcm

Windowed RI.C1 LAT G DRR.dcm

RI.C1 POST DRR.dcm

Windowed RI.C1 POST DRR.dcm

Figure 3.16: Windowed DRR images batch.

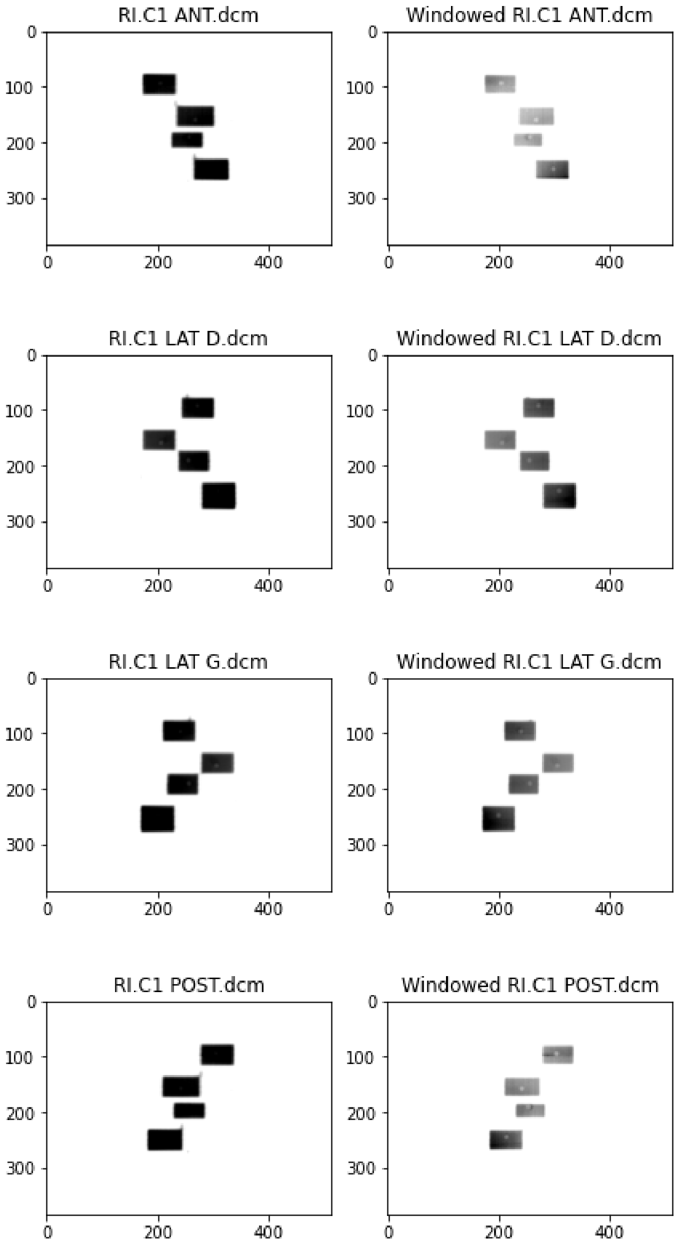

Figure 3.17: Windowed Portal images batch.

Superscaling

This step is the last one of the preprocessing phase and it is used in order to enhance the details of the spheres by increasing image resolution. This can be useful since our purpose is to perform geometrical measurements on the spheres and the irradiation fields of the images, thus having a higher-resolution image will allow us to perform more refined quantifications and improve the accuracy of our algorithm.

However, we have to consider that the information added in the new high-resolution images, is nothing new that was not present before. The process could be based on interpolation or on AI. In the first case, the colors of new pixels are estimated based on the color of the existing ones following certain mathematical algorithms, while in the second one, the AI algorithm is able to learn patterns on training data and based on that, guess the new pixels.

We followed both approaches: the first one using bicubic interpolation, and the second one using Enhanced Super Resolution Generative Adversarial Network (ES-RGAN) [31].

- **Bicubic Interpolation**

  In this case, we take 16 pixels around the pixel to be interpolated (4x4 neighborhood) as compared to the 4 pixels (2x2 neighborhood) we take into account for bilinear interpolation. Considering a 4x4 surface, we can find the values of the interpolated pixels using this formula:

  $$p(x,y) = \sum_{i=0}^{3} \sum_{j=0}^{3} a_{ij} x^i y^j \tag{3.4}$$

  The interpolation problem consists of determining the 16 coefficients a_{ij}. These coefficients can be determined from the p(x, y) values which are attained from the matrix of pixels and partial derivatives of individual pixels.

  Considering Figure 3.18, it is a (4,0) x (0,4) square with each square representing a pixel. It has a total of 25 pixels (5 x 5). The black dots represent the data being interpolated, which totals 25 dots. The colors indicate function values, so in this example, we see they are not radially symmetric. This allows for smoother resampling with little image artifacts [27].

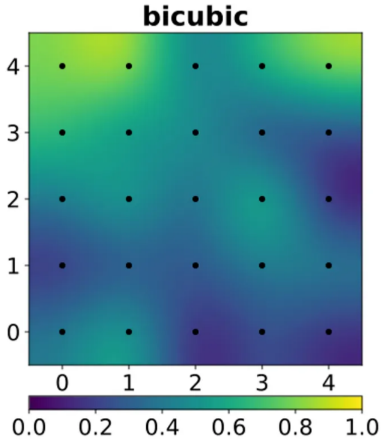

Figure 3.18: Bicubic Interpolation.

- **ESRGAN**

  This network, with its extension Real-ESRGAN [29], represents the state-of-the-art for what concerns image super-resolution tasks. It has been developed following the previously created model SRGAN, by improving it from three aspects:

  1. Adopt a deeper model using Residual-in-Residual Dense Block (RRDB) without batch normalization layers.
  2. Employ Relativistic average GAN instead of the vanilla GAN.
  3. Improve the perceptual loss by using the features before activation.

  To train the model different datasets have been used: DIV2K [9], Flickr2K [10], and OutdoorSceneTraining (OST) [11].

---

[9] https://data.vision.ee.ethz.ch/cvl/DIV2K/

[10] https://www.kaggle.com/datasets/daehoyang/flickr2k

[11] [30]

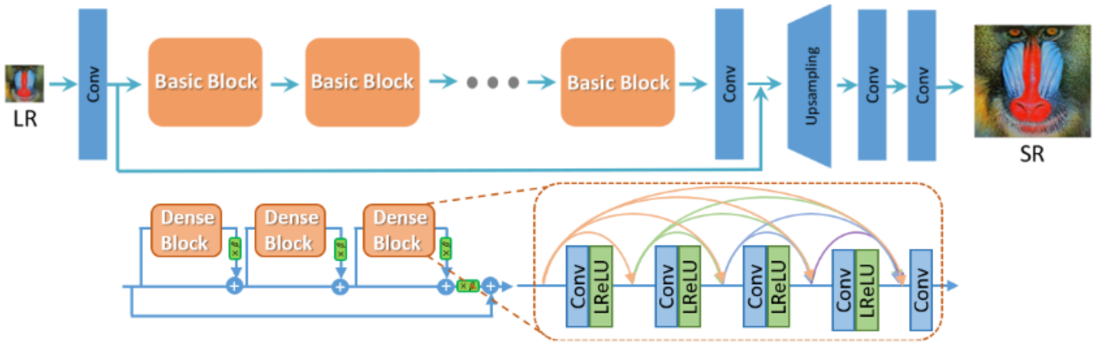

Figure 3.19: ESRGAN.

To compute bicubic interpolation, we exploited the resize function from OpenCV library using cv2.INTER_CUBIC parameter. For using ESRGAN instead, we downloaded the pre-trained model from https://github.com/xinntao/Real-ESRGAN and performed the inference script illustrated. In both cases, we used an x8 scale factor. This factor was empirically chosen by following the desired amount of precision in our measurements.

To perform the upscaling, the first method takes always less than 0.1 seconds for each image, while the inference of ESRGAN takes on average from 5 to 10 seconds per image. We will see later that our recognition/identification algorithm will make no difference for the upscaled images in one of the two ways, the result will be identical. This is the reason why we then decided to continue our computations with bicubic interpolated images since they require less computational effort.

In Figure 3.20 we can see the different upsampling methods on the ANT DRR image (bicubic interpolation at the center and ESRGAN on the right side). In this case, since the original image (on the left side) has a 956x956 shape, the resulting upscaled image will have a 7648x7648 shape. For what concerns the Portal images, they originally had a 384x512 shape, thus the upscaling will result in a 3072x4096 shape.

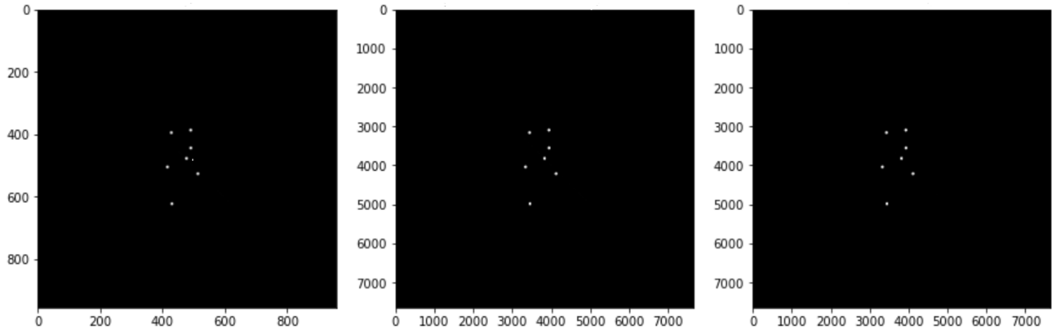

Figure 3.20: ANT DRR: Original Image, Bicubic Interpolation, ESRGAN.

3.2.4. Sphere Selection and Identification

As we explained in the introduction chapter, the first goal of this work is to calculate the geometric accuracy of positioning between correspondent spheres in DRR and Portal images. In particular, in this paragraph, we will face the problem of multiple sphere selection and identification (in both DRR and Portal images). The next one will later present the shift quantification.

The phase of sphere selection is the only step that is not fully automated in the developed program. It is still under human interaction. In particular, provided the batch of images from the previous steps, the idea is that the medical physicist in charge of this operation has to select the interested spheres from Portal images through a specific User Interface (UI). This process is done by simply "drawing" rectangles around each sphere in order to contain them.

As done until now, also the next subsections will be presented in the same order in which all the computations are performed. Specifically, sphere selection and identification are firstly performed on Portal images and then automatized on DRR images.

Portal Images

1. **Sphere Selection**

   In order to perform sphere selection, we exploited the *selectROI()* method offered by OpenCV. With this method, we can precisely and manually select the area(s) of interest we need from Portal images and hence we can perform many tasks for that specific area(s). In particular, in our case, we are going to perform different crops around each selected sphere for each of the 4 Portal images. The function is going to return different arrays (one for each crop) of different values. For each array, these values are: [the X-coordinate of the top-left point of the selected ROI, the Y-coordinate of the top-left point of the selected ROI, the width of the selected ROI, and the height of the selected ROI].

This process is performed on 384x512 Portal images so that the UI is not computationally weighted, and then the ROIs coordinates are scaled up to the 3072x4096 superscaled version to perform the crops. The result is shown in Figure 3.21: 4 crops (one for each sphere) for each Portal Image.

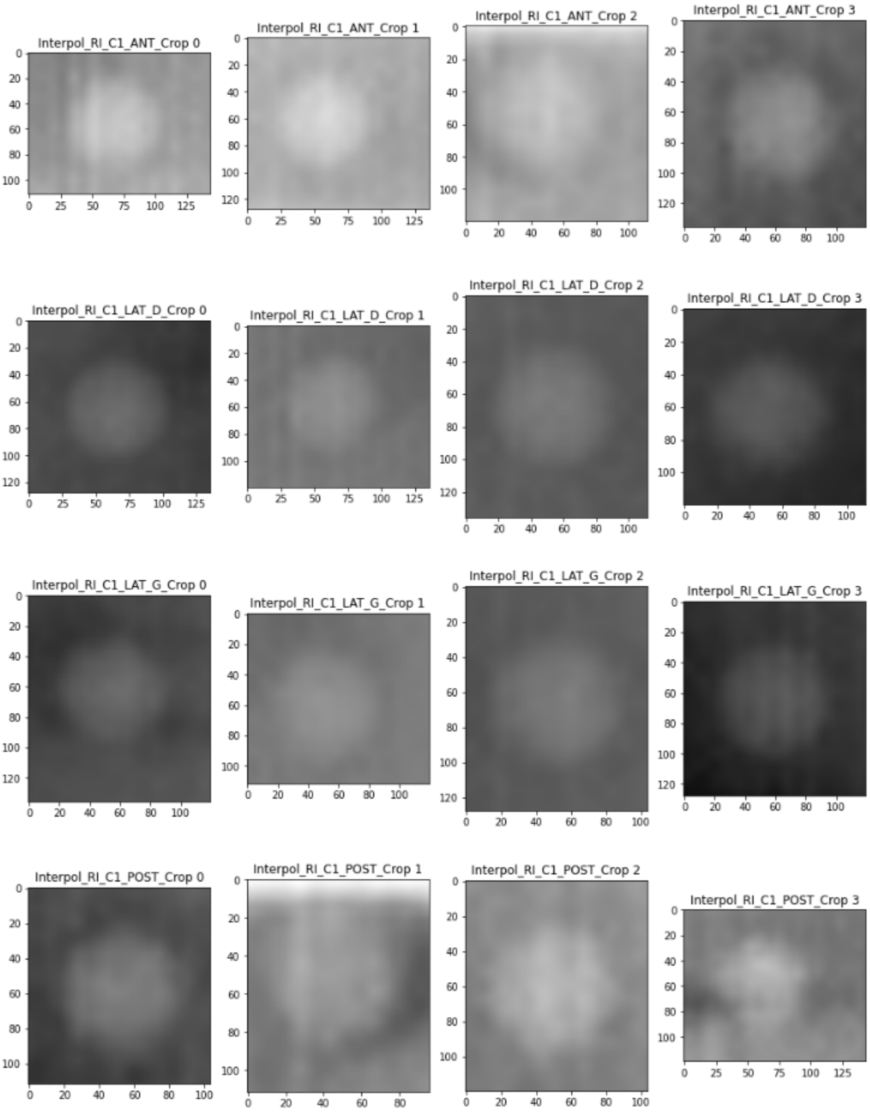

Figure 3.21: ROIs cropped from Portal images.

2. **Circle Identification**

At this point, we are able to perform our sphere recognition. This will consist of a standard circle detection on our cropped images. To do so, we exploit the Hough Circle Transform.

Hough Circle Transform is a feature extraction technique used for detecting circles in images, considered an extension of the more basic Hough Line Transform [11]. In a 2-dimensional space, a circle is defined by

$$(x-a)^2 + (y-b)^2 = r^2 \tag{3.5}$$

where *(a, b)* is the center of the circle and r is the radius. The circle candidates are produced by “voting” in the Hough parameter space and then selecting local maxima in an accumulator matrix.

If we consider a fixed radius, the parameter space would be reduced to 2 dimensions, thus for each point in the (x, y), it can be defined as a circle centered at (x, y) in the (a, b) space. The intersection point of all such circles in the parameter space would correspond to the center point of the original circle. In Picture 3.22 for example, we consider 4 points on the circle of the original image (left). The correspondent Hough Transform is shown in the right image.

For each of the 4 points (x, y), can be defined a circle in the Hough parameter space centered at (x, y) with radius r. An accumulator matrix is used for tracking the intersection point. In the parameter space, the voting number of points through which the circle passes would be increased by one. Then the local maxima point (the red point in the center of the right figure) can be found. The position (a, b) of the maxima would be the center of the original circle [18].

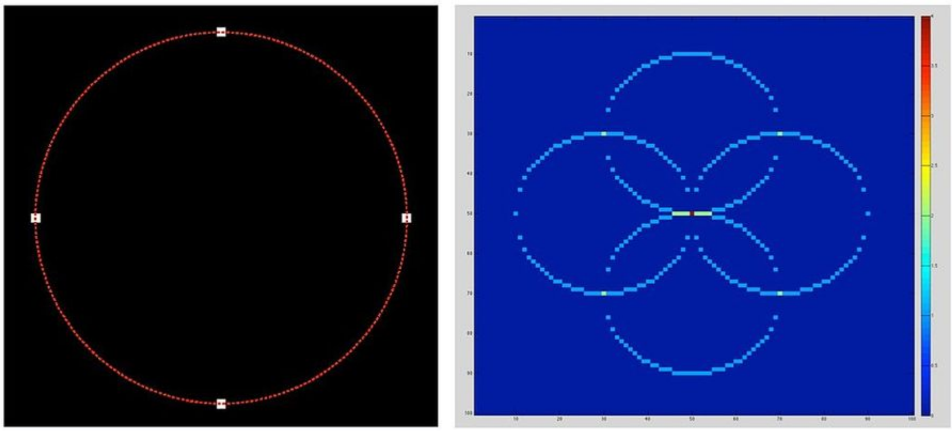

Figure 3.22: Hough Circle Transform.

In cases in which we do not know the radius value, we face a 3 dimensions parameter space, and the algorithm for filling the accumulator would be inefficient. This is the reason why we adopted the Hough Gradient Method offered by OpenCV. Here, instead of drawing the full circle in the parameter space, we only increment the accumulator cells in the gradient direction of each edge pixel. This method consists of two steps: finding all the plausible candidates for the circle centers and, for each candidate center, finding the best radius.

The edge image is calculated using the Canny edge detector [8], and the gradient is computed using the Sobel operator for each edge pixel. For each edge pixel, we increment the accumulator cells that lie in both directions of the gradient. Then we select all those accumulator cells that are both local maxima and above a certain threshold. All these accumulator cells are plausible candidates for circle centers. Once we obtain the center candidates, we have to find the best radius for each candidate. The parameter space is now reduced to 1 dimension. To fill this 1-dimensional accumulator array, for each candidate center, we just calculate its distance from all edge pixels(and increment the corresponding accumulator cell. The best radius will be the one that is best supported by the edge pixels. Repeat this for each candidate center.

Before applying the Hough Gradient Method, we blurred the images in order to reduce the noise.

```
median_blur = cv2.blur(crop_temp, (11,11))
detected_circles = cv2.HoughCircles(median_blur, cv2.
    HOUGH_GRADIENT, 1, 140, param1=15, param2=10, minRadius
    =27, maxRadius=50)
```

We can see an example of the result in Picture 3.23, which refers to the 4 crops of ANT Portal image.

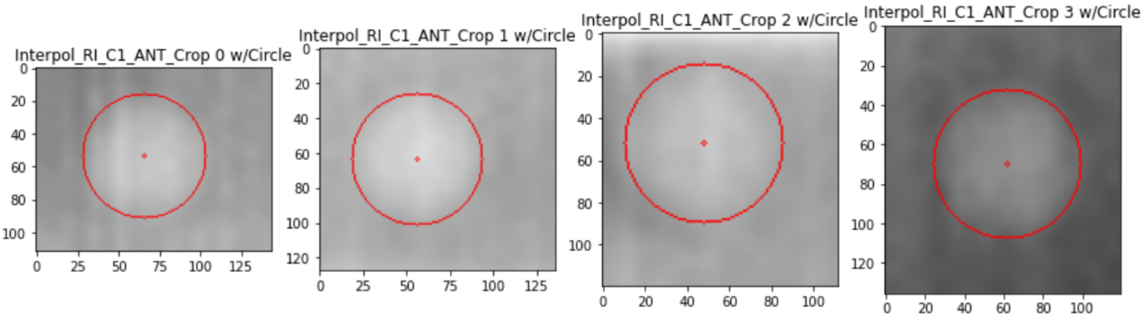

Figure 3.23: Result of Hough Circle Transform for ANT Portal image crops.

The circle identification is performed on single crops in order to avoid the processing of an entire 3072x4096 image. In this way, we save the local coordinates of the circles' centers from the crops, and then we convert them to superscaled image coordinates. The process is done by simply multiplying x8 the upper-left corner of each crop and adding the horizontal and vertical displacement of the center of each circle from the crops. In this way, we bring back each detected circle on the correspondent Portal image, as we can see in Figure 3.24, which still represents the example of the ANT Portal image.

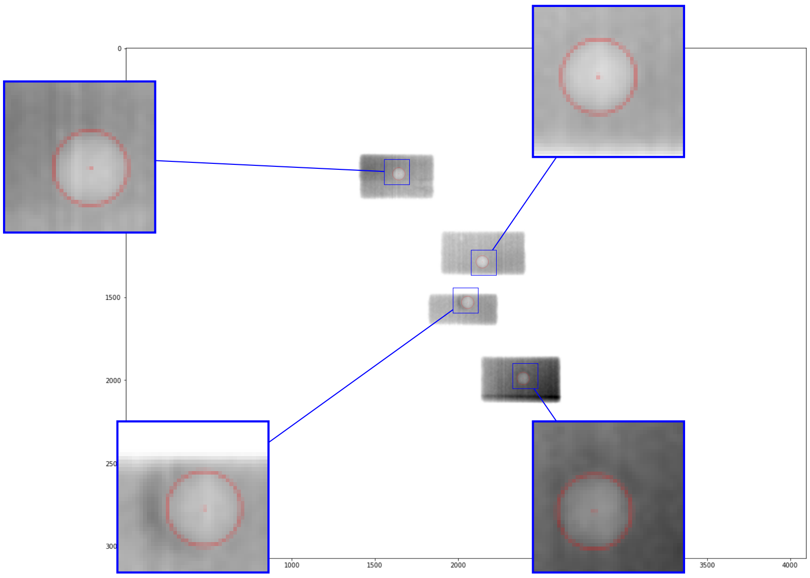

Figure 3.24: ANT Portal image identified spheres.

DRR

Regarding DRR images, here we want to completely automatize the sphere selection and identification in order to speed up the process and not rely on the user. For this reason, we exploit the previous knowledge we obtained about crops' coordinates, after ROIs selection by the user on Portal images.

The first step that must be done, if we want to use those coordinates, is to make them comparable with DRR images. In particular, we know that Portal images have a 3072x4096 shape while DRR ones have a 7648x7648 shape. So, we need to bring them to the same shape. This process is called image padding, or border padding, and it consists of adding extra rows or columns to the edges of an image. In this way, the size of the image is increased, but the original content remains unchanged.

In our case, the rows and columns differences between the two shapes are 4576 (i.e. 7648 - 3072) and 3552 (i.e. 7648 - 4096). Thus, we added 2288 (i.e. 4576/2) rows to the top and to the bottom and 1776 (i.e. 3552/2) columns to the right and to the left of DRR images.

At this point, it is obvious that since we want to detect the spheres in DRR images, the crop coordinates we found before on Portal images are useful only if the correspondent spheres are almost aligned (or if the difference in position is not so large). Here we made a strong assumption. As explained in the introduction chapter, the step at which our program aims to be helpful already presumes a first alignment of the phantom through the OBI system. Any shift that is present can be caused by many factors, for example, a misalignment between OBI and EPI system, or couch rotation problems. Here we assume that this misalignment is not particularly pronounced so as to not exceed 5mm, which is a quite large shift in our context.

This assumption has been made because, as stated before, we want to exploit the knowledge of Portal images' crop coordinates. In particular, in order to create new crops from DRR images, we decided to enlarge the previous crops by a window of 30 pixels per side. We can see the result in Figure 3.25.

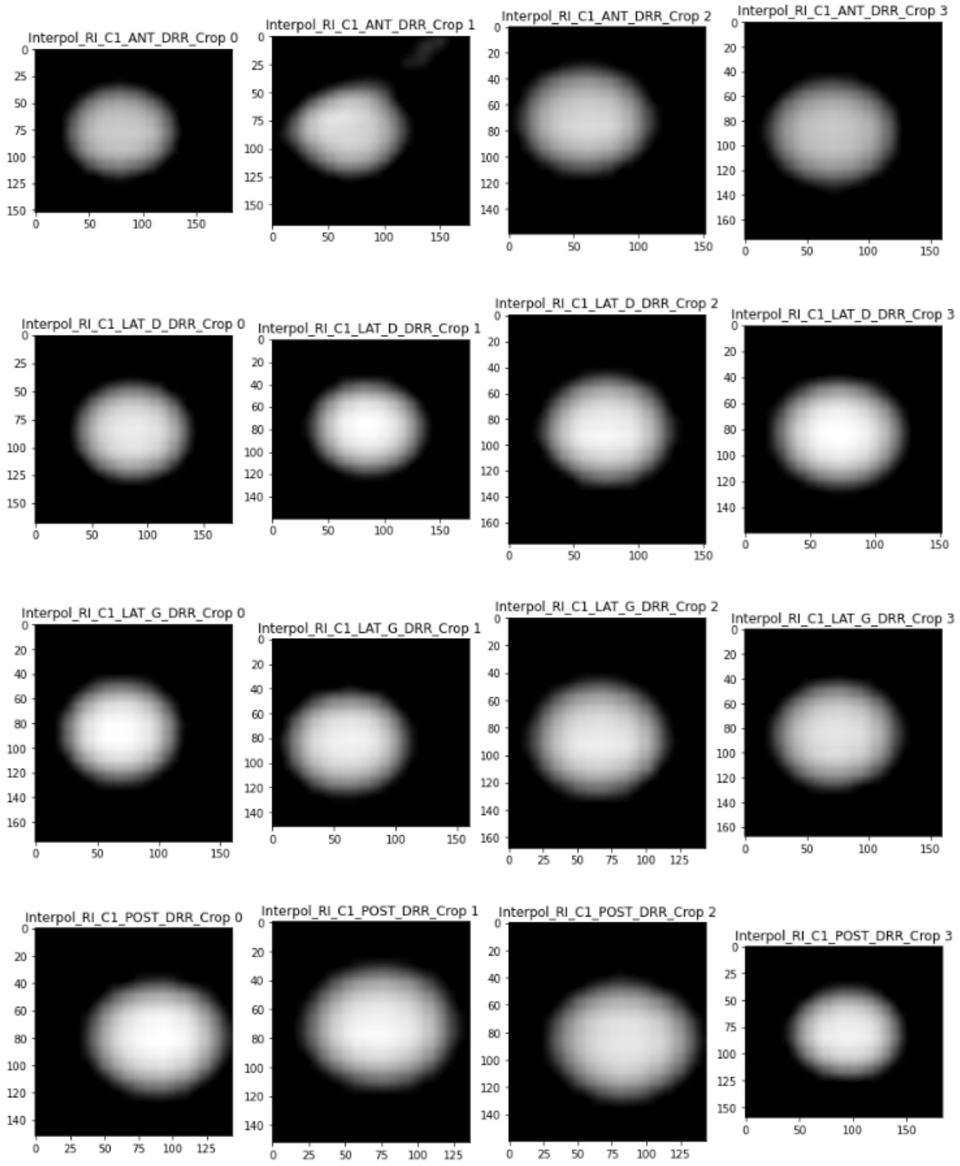

Figure 3.25: ROIs cropped from DRR images.

The next steps are exactly the same as for Portal images: on these crops, we first recognized each sphere - still by exploiting Hough Circle Transform, Figure 3.26 - and then we brought back the ROIs coordinates on the correspondent superscaled DRR images, Figure 3.27.

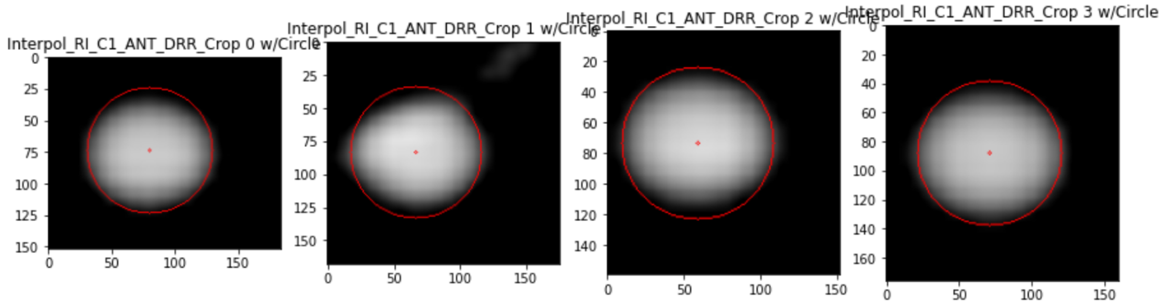

Figure 3.26: Result of Hough Circle Transform for ANT DRR image crops.

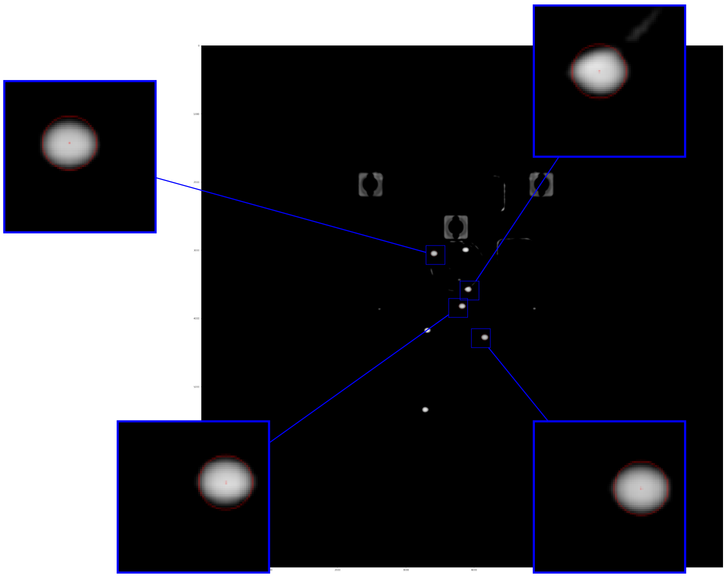

Figure 3.27: ANT DRR Image - identified spheres.

3.2.5. Sphere Shift Measurements

In this section, we are going to evaluate the shifts between each corresponding sphere on DRR and Portal images. This is done by first performing a superimposition of the two correspondent multi-modal images (DRR and Portal) and then measuring the distances between the centers of each correspondent circle as a 2D Euclidian distance.

As specified in the background chapter, this process is applied once the registration has already been performed. It is a way of measuring its effectiveness with respect to the EPI system.

Recalling some terms used during registration applications, we can think of the central sphere (single isocenter) as our fiducial point, since it is the point used for superimposition. The process can be thought of as a point-based registration where we have two sets of 2D points obtained by feature extraction. However, without performing any rigid or non-rigid transformation we want to measure the target registration error for each sphere, which represents the accuracy of the EPI system during treatment irradiation.

Since our objective is to superimpose the two images, in order to be effective, they must have the same shape. It is then necessary to compute image padding. Consequently, we first build 7648x7648 blank images. Then, we build a frame around the shape of the Portal images - which are the smaller ones - with white pixels, so that they will have the same shape as the DRR images. After that, we place Portal images at the center of these frames. The final result will be a batch of 7648x7648 Portal images, with exactly the same content as before.

```
img = np.zeros([7648, 7648, 3], dtype=np.uint8)
img.fill(255)
img[0:2288, :] = [255, 255, 255]
img[2288 + 3072:7648 , :] =  [255, 255, 255]
img[:, 0:1776] = [255, 255, 255]
img[:, 1776 + 4096:7648] =  [255, 255, 255]
img[2288:7648 - 2288, 1776:7648 - 1776] = epid_image
```

Now it is possible to superimpose the different couples of DRR and Portal images and measure the shifts. We can see in the next Figures, the 4 couples through blended images. The results of the shifts will be presented in the next chapter.

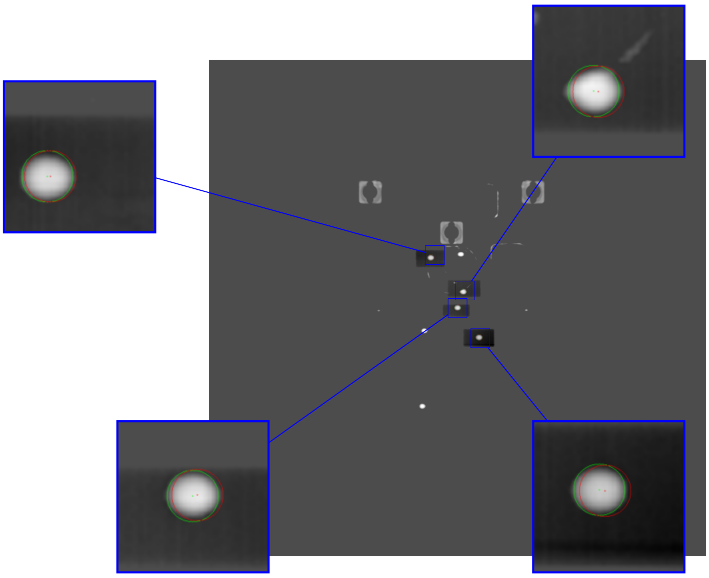

Figure 3.28: Blended ANT DRR and ANT Portal images.

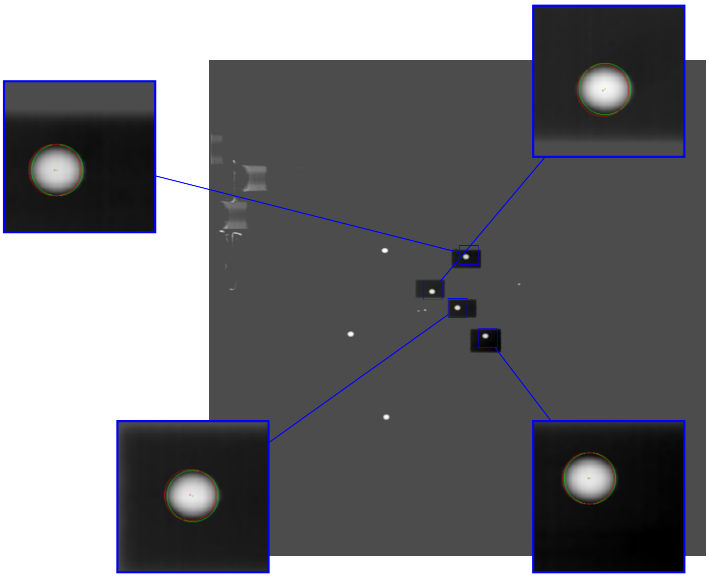

Figure 3.29: Blended LAT D DRR and LAT D Portal images.

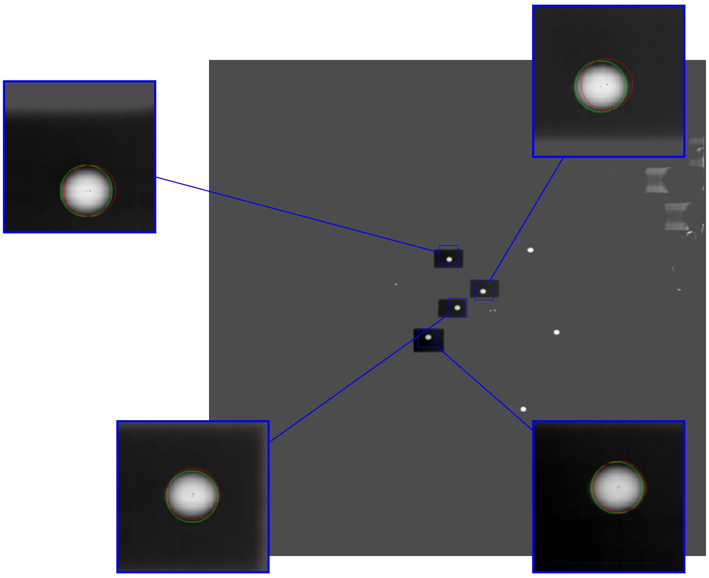

Figure 3.30: Blended LAT G DRR and LAT G Portal images.

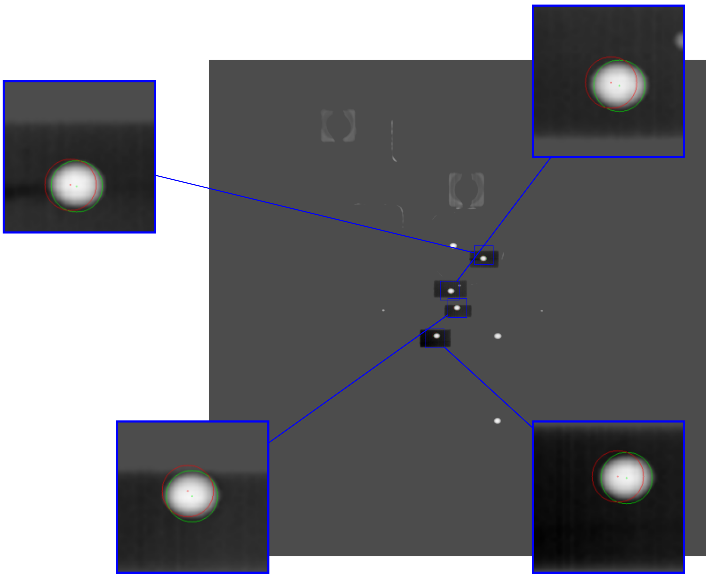

Figure 3.31: Blended POST DRR and POST Portal images.

As we can see from these Figures, we decided to color the identified circles of DRR images (representing the ground truth positions) in green, and those of Portal images in red.

To check the effectiveness of our recognition algorithm, we compare the centers of the spheres identified by the algorithm with the centers measured by hand by a medical physics operator. We report the results in the next chapter.

Before applying this sequence of steps and these techniques, we also tried to implement the same approach on another type of phantom, whose sphere distances were known a priori. We did it in order to test the efficiency of these methods and the accuracy of measurements.

As described in the Materials chapter, we used the ISO Cube Phantom for this purpose. It is constituted of two 6.35 mm diameter spheres with fixed defined positions by construction (Figure 3.2). The objective is to apply the same sequence of steps we described for spheres' preprocessing, identification, and measurement on DRR and Portal images. The idea is to compare the measured distances with the real ones known by construction, in order to see the consistency and the effectiveness of our methods.

This is done because, inside the Head Phantom, the spheres are manually positioned, thus there are no precise known distances among them. Even the theoretical DRR positions need to be trusted. We chose the ISO Cube Phantom since the resulting images from DRR generation and Portal imaging, are strictly similar to those of Head Phantom due to material composition. Thus, we expect that the shape identification algorithms will perform with the same precision.

In the following Figures, we show the original ISO Cube Phantom batches of DRR and Portal images.

(a) ANT - Gantry 0°.

(b) LAT G - Gantry 90°.

(c) LAT D - Gantry 270°.

(d) POST - Gantry 180°.

Figure 3.32: ISO Cube Phantom DRR images from the 4 different gantry angles.

(a) ANT - Gantry 0°.

(b) LAT G - Gantry 90°.

(c) LAT D - Gantry 270°.

(d) POST - Gantry 180°.

Figure 3.33: ISO Cube Phantom DRR images from the 4 different gantry angles.

We do not describe in detail all the steps of preprocessing and sphere identification, since they have already been explained for Head Phantom and they are identically re-implemented for these new batches of images with the same purpose.

What is interesting here is the comparison of the measured distances between identified central and off-center spheres with the ground-truth spheres' distances, for each image. In the next chapter, we report the adopted metrics as well as the results.

3.2.6. DRR - Irradiation Field Reconstruction

This chapter will explain the process of irradiation field reconstruction for DRR images. As introduced in the Background chapter, the irradiation fields are those rectangles visible in Portal images around each target sphere caused by treatment beams modeled by the MLC. In our case, from the definition of Multi-Target SRT/SRS, the objective is to define a single irradiation field around each single sphere. The desired shape of the irradiation field is reflected in images thanks to the precision of MLC leaves and their capacity to reproduce custom shapes. The X-ray beams will pass only through the open section created by the leaves, irradiating the target.

In DRR images, the irradiation fields are not visible on images, since the images are digitally generated in their complete extension, thus it is impossible to perform shape recognition as we did for the sphere shift measurement. Here, the information about irradiation fields is contained inside the DICOM header files. It is necessary to reconstruct the shape of irradiation fields starting from this information.

We will now illustrate the tags we exploited in order to obtain the necessary information:

BeamLimitingDeviceSequence[2].LeafPositionBoundaries tag allows to get boundaries of beam limiting device (collimator) leaves (in *mm*), i.e. Y-axis offsets from the isocenter of the treatment for each leaf pair, their vertical thickness. It contains N+1 values, where N is the number of leaf/jaw pairs. In our case, we have 60 leaves.

```
leaf_position_boundaries = BeamSequence[beam_sequence_num].BeamLimitingDeviceSequence[2].LeafPositionBoundaries

>>> print(leaf_position_boundaries)
[-200, -190, -180, -170, -160, -150, -140, -130, -120, -110, -100, -95, -90, -85, -80, -75, -70, -65, -60, -55, -50, -45, -40, -35, -30, -25, -20, -15, -10, -5, 0, 5, 10, 15, 20, 25, 30, 35, 40, 45, 50, 55, 60, 65, 70, 75, 80, 85, 90, 95, 100, 110, 120, 130, 140, 150, 160, 170, 180, 190, 200]
```

If we observe Figure 3.34, we can see the positioning of MLC leaves in order to create the shape of the target. The isocenter is given by the intersection of the X and Y-axis, thus assuming that each leaf has a thickness of 10 *mm*, the *LeafPositionBoundaires* tag would obtain a value like [-45, -35, -25, -15, -5, 0, +5, +15, +25, +35].

BeamLimitingDevicePositionSequence[2].LeafJawPositions tag allows us to get positions of beam limiting device (collimator) leaf pairs (in *mm*), i.e. X-axis offsets from the isocenter for each leaf, the horizontal offset from the closed position. It contains 2N values, where N is the number of leaves. In our case, for leaves we have 120 values.

```
leaf_jaw_positions = BeamSequence[beam_sequence_num].ControlPointSequence[0].BeamLimitingDevicePositionSequence[2].LeafJawPositions
>>> print(leaf_jaw_positions)
```

```
[0, 0, 0, 0, 0, 0, 0, 0, 0, -0.24, 0, 0, 0, 0, 0, 0, 0.21, 0.21,
   0.21, 0.21, -3.27, 0.04, 5.87, 5.87, 5.87, 5.87, 5.87, -51.54,
    -14.99, -14.99, -14.99, -50.75, -10.28, -10.28, -10.28,
   -10.28, -11.77, -52.38, -42.02, -42.02, -42.02, -42.02, -1.2,
   -1.2, 0, 0, 0, 0, 0, 0, 0, 0, 0, 0, 0, 0, 0, 0, 0, 0, 0, 0, 0,
    0, 0, 0, 0, 0, 0, -0.24, 0, 0, 0, 0, 0, 0, 0.21, 0.21, 0.21,
   0.21, -3.27, 0.04, 37.61, 37.61, 37.61, 37.61, 5.87, -51.54,
   13.17, 13.17, 13.17, -50.75, 24.09, 24.09, 24.09, 24.09,
   -11.77, -52.38, -11.77, -11.77, -11.77, -11.77, -1.2, -1.2, 0,
    0, 0, 0, 0, 0, 0, 0, 0, 0, 0, 0, 0, 0, 0, 0]
```

BeamLimitingDevicePositionSequence[0].LeafJawPositions and **BeamLimitingDevicePositionSequence[1].LeafJawPositions** tags, allow us to get positions of jaw pairs (in *mm*), i.e. X-axis and Y-axis offsets from the isocenter for jaws, the horizontal and vertical offset from the closed position. They contain 2 values each.

```
jaw_position_x = beam_sequence[beam_sequence_num].
   ControlPointSequence[0].BeamLimitingDevicePositionSequence[0].
   LeafJawPositions

jaw_position_y = beam_sequence[beam_sequence_num].
   ControlPointSequence[0].BeamLimitingDevicePositionSequence[1].
   LeafJawPositions

>>> print(jaw_position_x)
[-45, 41]
>>> print(jaw_position_y)
[-43, 61]
```

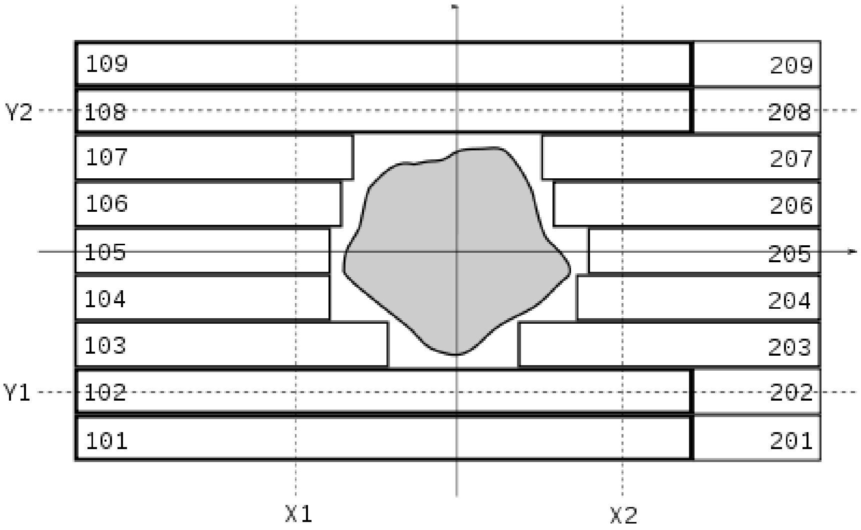

Figure 3.34: MLC leaf pairs positions.

In our case, the values of *LeafPositionBoundaries* would remain the same for each image, since they are taken from the same LINAC, thus the physical characteristics of MLC are the same. What changes is the *LeafJawPositions* tag, since for each image we have different opening positions for leaves and jaws due to the fact that the irradiation fields for the spheres will not be the same. In the upper case, we reported the coordinates of each leaf and jaw for the ANT case. Again, as we also previously said, if we have a look at Portal images, we can see that around each ball we have an irradiation field. For each image, we have a total of 4 irradiation fields. We then expect *LeafJawPositions* tags to present 4 intervals of values interludes by closed position values (sequences of 0's).

In order to reconstruct the irradiation fields of each image, we associated the first half of *LeafJawPositions* values with *LeafPositionBoundaries* in the same way as the second half of *LeafJawPositions* values and *LeafPositionBoundaries*. The first half represents the sequence of left leaves, while the second half the right ones. We then computed X coordinates by subtracting (adding) the values of the first half (second half) from the image center coordinates. By doing this, and converting *mm* distances into pixel values, we build a pair of coordinates for each extreme of the leaves. In this way, we are able to locate the extremes of each irradiation field. We also reconstructed the field made by the jaws, and for each Leaf field, we checked that it was not further modeled by jaws fields. In those cases, we computed the new irradiation fields as the more restricting ones given by the combination of jaws and leaves extremes.

In the next Figures, we also display the computed irradiation fields on DRR images, while in the next chapter, we will report the pixel coordinates for each irradiation field, expressed in a 7648x7648 setting.

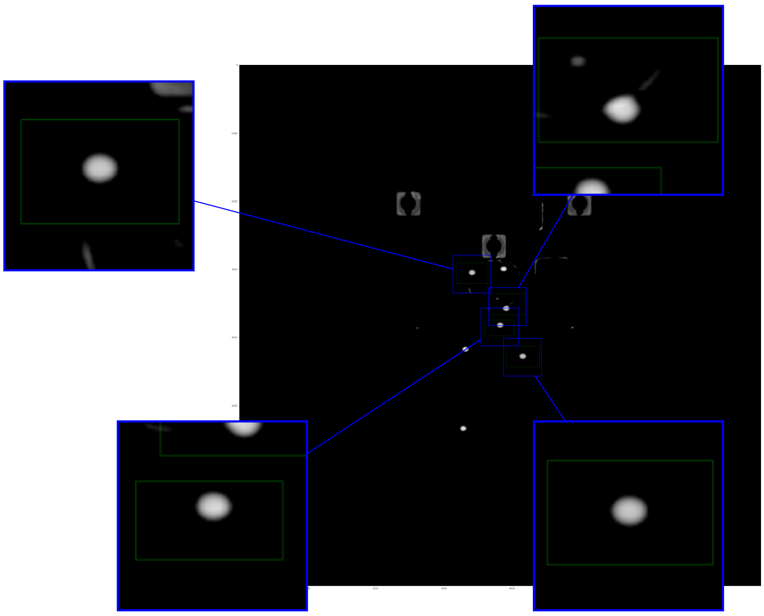

Figure 3.35: ANT DRR image irradiation fields.

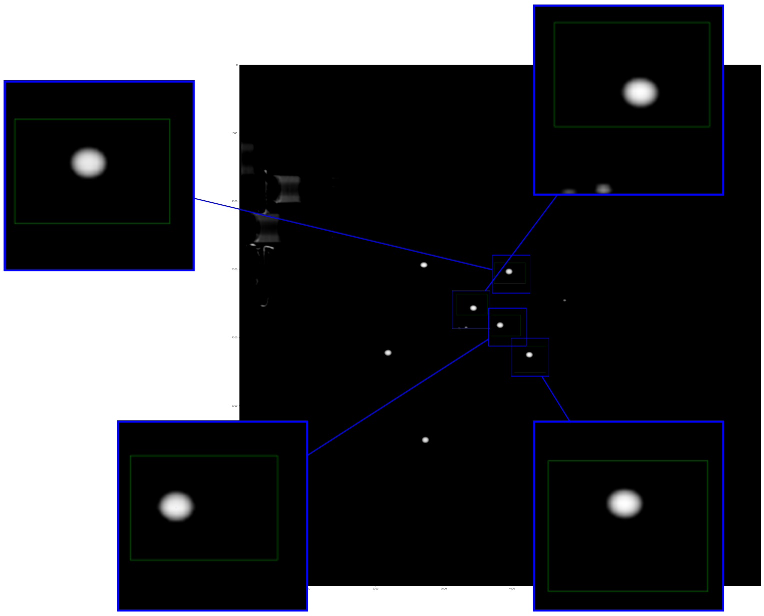

Figure 3.36: LAT D DRR image irradiation fields.

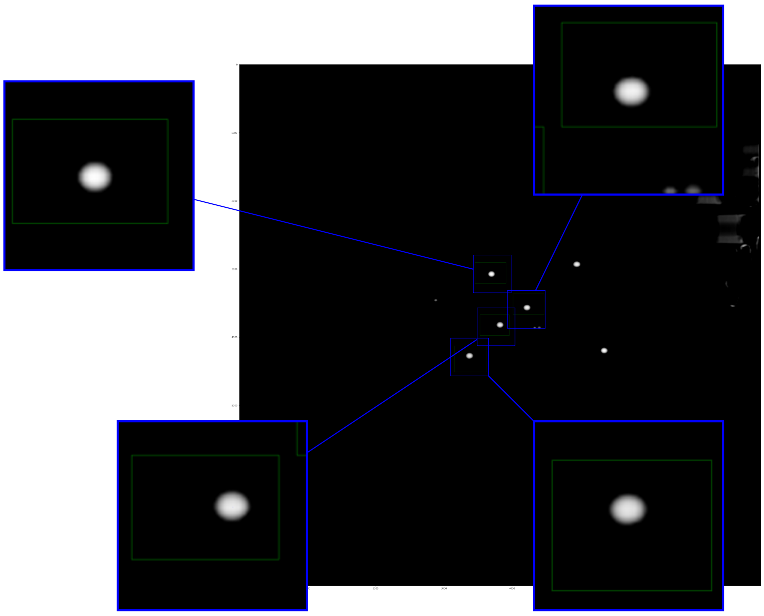

Figure 3.37: LAT G DRR image irradiation fields.

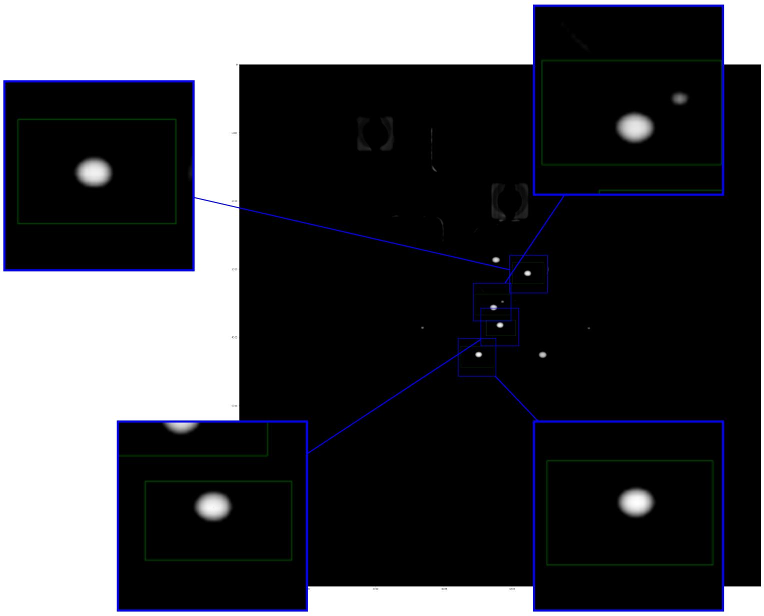

Figure 3.38: POST DRR image irradiation fields.

3.2.7. Portal Image - Irradiation Field Identification

For what concerns Portal images, on the other side, it is necessary to recognize the irradiation fields from images. As we explained in the previous subsection, they are directly reflected on images through the open section on LINAC MLC. The background concepts are really similar to those we explained for sphere identification and circle recognition. However, there is a missing concept that still needs to be introduced.

This concept is referred to as the penumbra effect. If we consider Figure 3.15b, its representation refers to an ideal situation: in this case, our X-rays are coming from one point source. Since the X-rays travel in straight lines, if the edge of the irradiation object is well defined, then the edge in the image will also be well defined as all the X-rays are coming from the same location. If we have a perfect point for our focal spot, it is going to look sharp on our image as measured at the detector, because there will be a crisp line delineating both sides of this structure as shown in the figure.

In reality, since there is a finite size of each focal spot, the X-rays are actually coming out over a 2D region and not just a single point. Considering Figure 3.39, we can image X-rays originating from the top and the bottom of the source, the representation here takes into consideration only one dimension. This shows you that if we want to image an edge, the edge is not going to be perfectly crisp because the image will have a gradual transition rather than the sharp transition that occurred in Figure 3.15b. This effect occurs on each edge of the 2D region.

The X-rays passing through the target object are coming from the whole region of the focal spot. The blurring effect then depends upon the size of the focal spot: the larger the focal spot size is, the more blurring that will occur on the detector. The blurring region is typically called the penumbra of the X-ray beam, and the region that is fully blocked behind the object is termed the umbra. Another example can be observed in Figure 3.40.

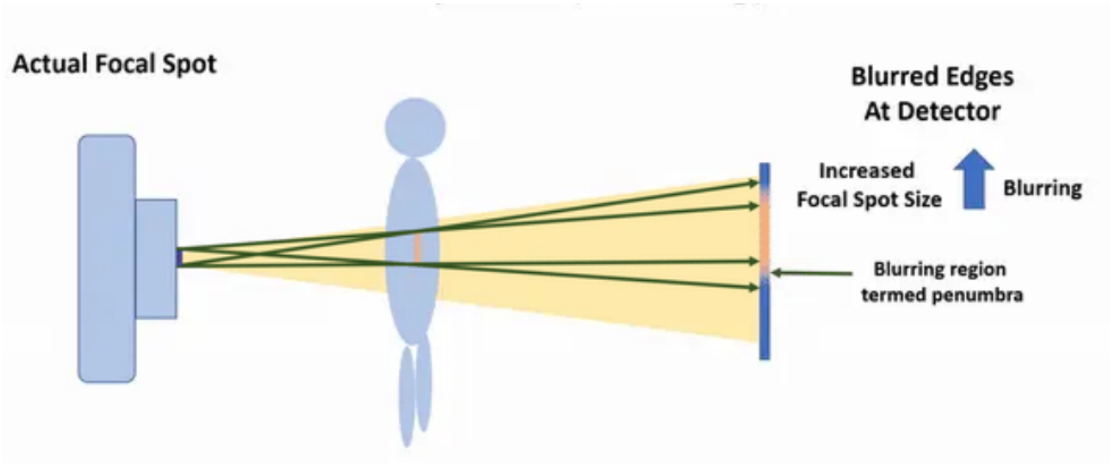

Figure 3.39: Geometric Unsharpness.

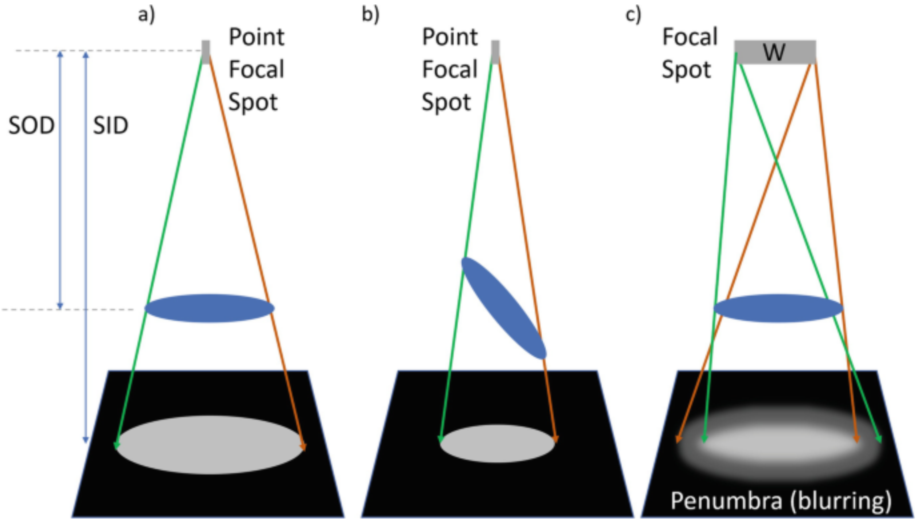

Figure 3.40: Penumbra Effect.

After this theoretical background, we can start to highlight the main steps we followed for irradiation field identification.

The first relevant point is that starting with the batch of Portal images before the preprocessing phase, the windowing phase was not applied. The reason is that by applying windowing, we are affecting the edges of irradiation fields. They will result tighter or larger depending on how we select WW and WL, differing from their original shape. It would modify the original content of the batch of Portal images. In this case, we need to work on the original content: the target spheres are not visible, but we are interested in the recognition of irradiation fields' edges.

The original batch of Portal images is then simply superscaled, getting a 4x3072x4096 shape. At this point, if we look at the superscaled images, it is clearly evident the penumbra effect. Before performing irradiation field identification, it is necessary to establish the window size for each irradiation field, i.e. we need to decide the sensitivity to the blurred image of the shape recognition algorithm. It is obvious that if we consider the beginning of the internal blur for shape recognition, this would lead to strongly different results with respect to the case in which we consider the external perimeter of the blurring effect on images.

We perform here an assumption that is always made, even if approximately, when the same process is performed by hand by the medical physicist in charge. If we consider the set of intensity values (0-255 range) for each Portal image, we set a threshold on the half values of these ranges, and we standardize all the values under the threshold to 0 as pixel intensity.

```
thresh_value = ((np.max(image) - np.min(image) ) / 2)
result = (image > thresh_value) * image
```

The results are displayed in Figure 3.41.

The following step is the simple removal of intensity pixels with a non-zero value. This is done by iterating over the batch of images and setting to 255 the pixels where the intensity is different from 0 while keeping them 0 if they already are 0. By doing this, we delineate the edges over which we are going to perform shape recognition.

To perform irradiation field detection, we exploit OpenCV library and Canny Edge detection method. In this case, we find the contours of each irradiation field and we define bounding boxes around them, based on the maximum external points of each detected contour.

```
median_blur = cv2.medianBlur(portal_image , 5)
canny_output = cv2.Canny(median_blur , 50, 100)
contours , _ = cv2.findContours(canny_output , cv2.RETR_EXTERNAL ,
    cv2.CHAIN_APPROX_SIMPLE)

for c in contours:
          cv2.drawContours(portal_image ,[c],0,(255,0,0),1)
          rot_rect = cv2.minAreaRect(c)
          box = cv2.boxPoints(rot_rect)
          box = np.int0(box)
          cv2.drawContours(portal_image ,[box],0,(255,0,0),1)
```

We can see for example the result of the detected irradiation fields for ANT Portal Image in Figure 3.43. Both the field contours and bounding box are depicted in red, but it is still clearly visible the differentiation. The bounding boxes of each irradiation field will be the ones used for the comparison with DRR images' irradiation fields.

We will report the pixel coordinates for each detected bounding box i.e. irradiation fields in the next chapter.

(a) ANT Portal image thresholded. (b) LAT G Portal image thresholded.

(c) LAT D Portal image thresholded. (d) POST Portal image thresholded.

Figure 3.41: Batch of thresholded Portal images.

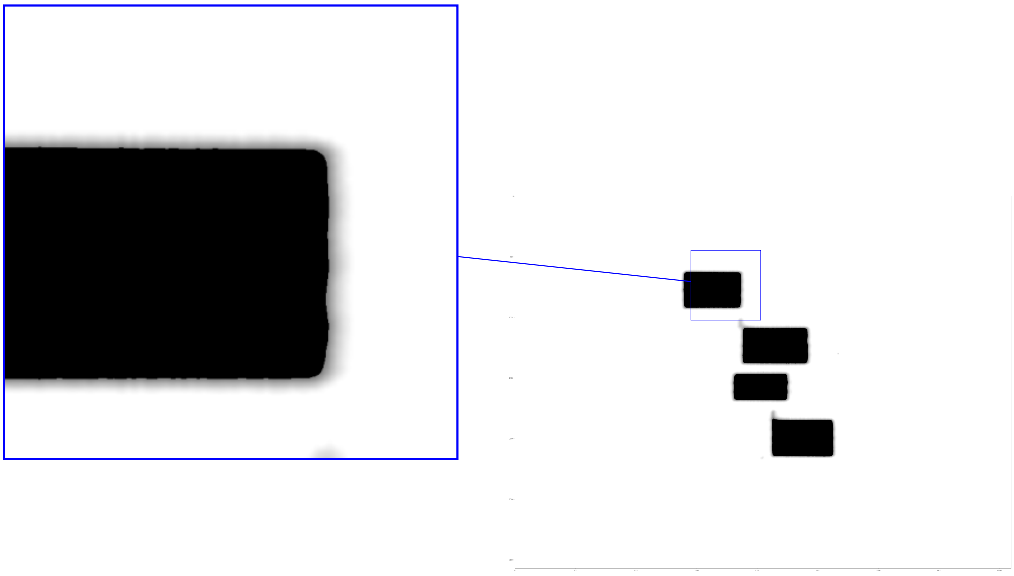

Figure 3.42: ANT Portal image thresholded - zoom.

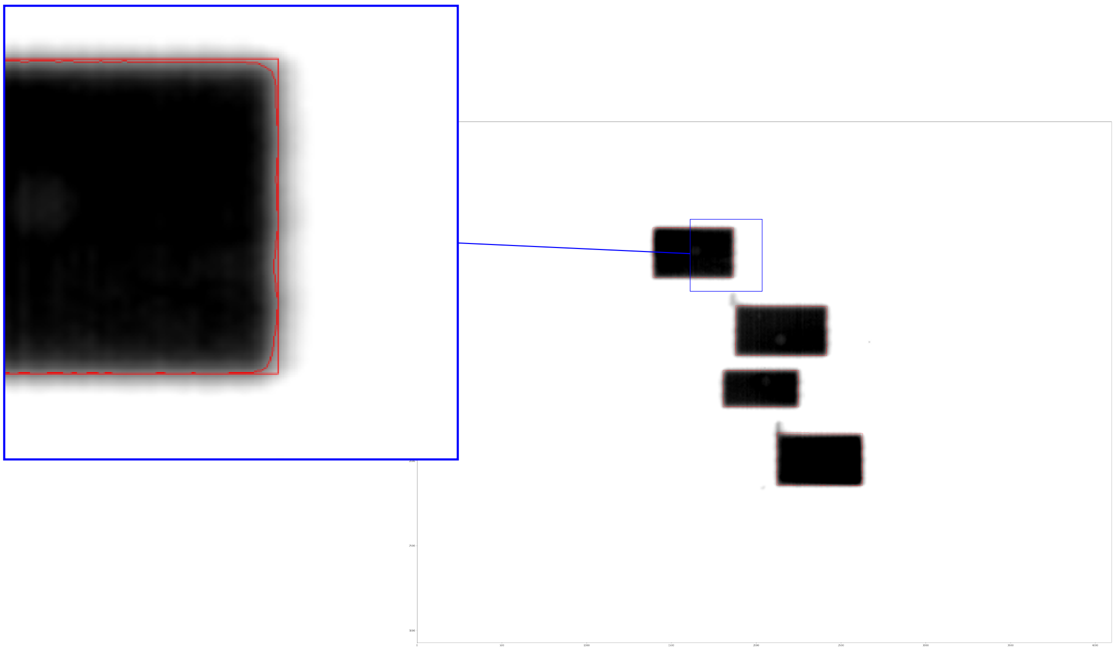

Figure 3.43: ANT Portal image detected irradiation fields.

3.2.8. Irradiation Field Shift Measurements

In this section, we are going to evaluate the shifts between each corresponding irradiation field on DRR and Portal Images. The process follows the same one adopted for sphere shift measurement: couples of corresponding DRR and Portal images are superimposed and then the distances between each bounding box are measured.

In order to compare the two different types of images, it is still necessary to bring them to the same shape. Thus, we simply compute new bounding box coordinates for Portal images by adding horizontal and vertical offset values with respect to DRR Images i.e. 1776 and 2288, in particular to their X-axis and Y-axis coordinates, respectively. We will then have all the irradiation field coordinates in a 7648x7648 shape setting.

Also, we perform image padding (exactly as in sphere shift measurements) to allow the superimposition of images. We create a frame around Portal images so that they will have the same shape as DRR images, i.e. 7648x7648.

```
img = np.zeros([hh, ww, 3], dtype=np.uint8)
img.fill(255)
img[0:2288, :] = [255, 255, 255]
img[2288 + 3072:7648, :] =  [255, 255, 255]
img[:, 0:1776] = [255, 255, 255]
img[:, 1776 + 4096:7648] =  [255, 255, 255]
img[2288:7648 - 2288, 1776:7648 - 1776] = epid_image
```

Now it is possible to superimpose the different couples of DRR and Portal images and measure the shifts. We can see in the next Figures the 4 couples through blended images. In green, we represented the ground truth irradiation fields for DRR images, while in red the ones of Portal images. The metric and the results for shift measurements will be presented in the next chapter.

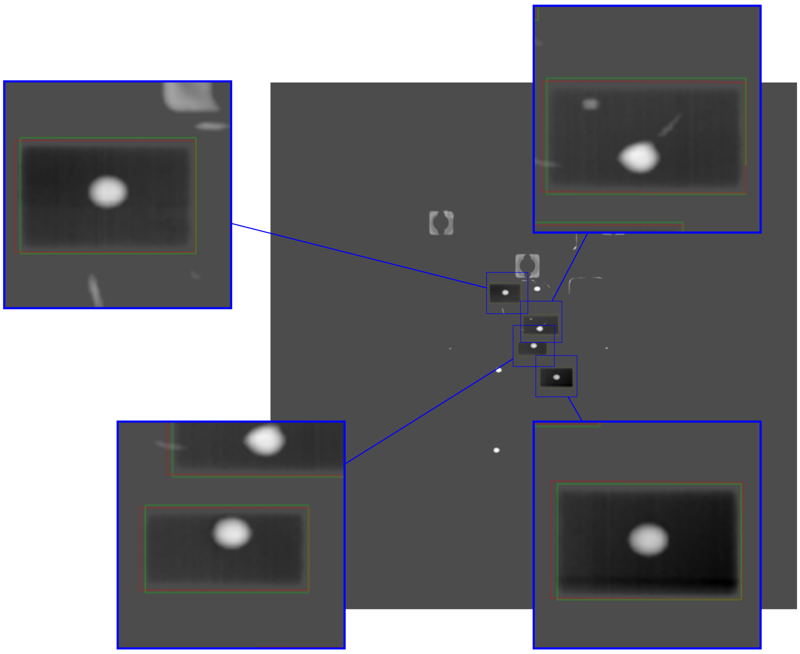

Figure 3.44: Blended ANT DRR and ANT Portal images - irradiation fields.

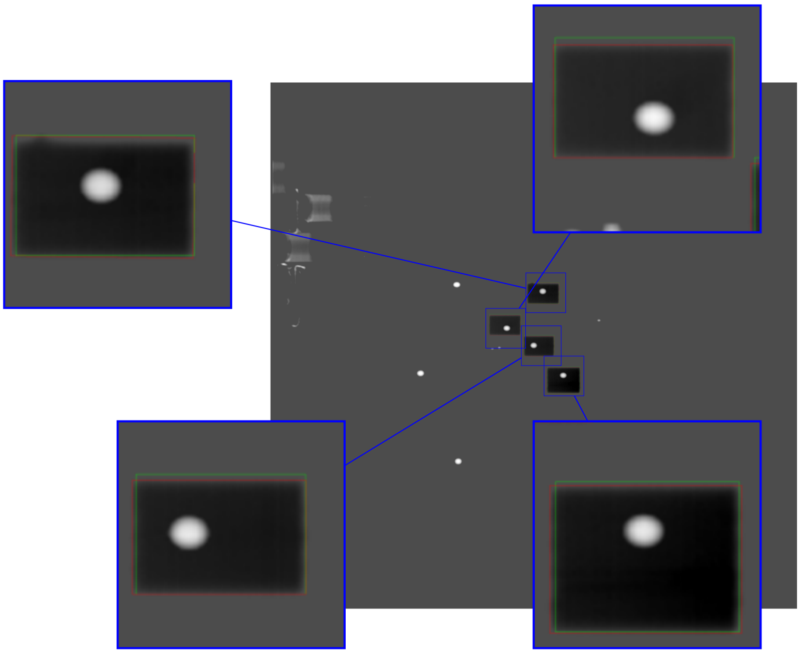

Figure 3.45: Blended LAT D DRR and LAT D Portal images - irradiation fields.

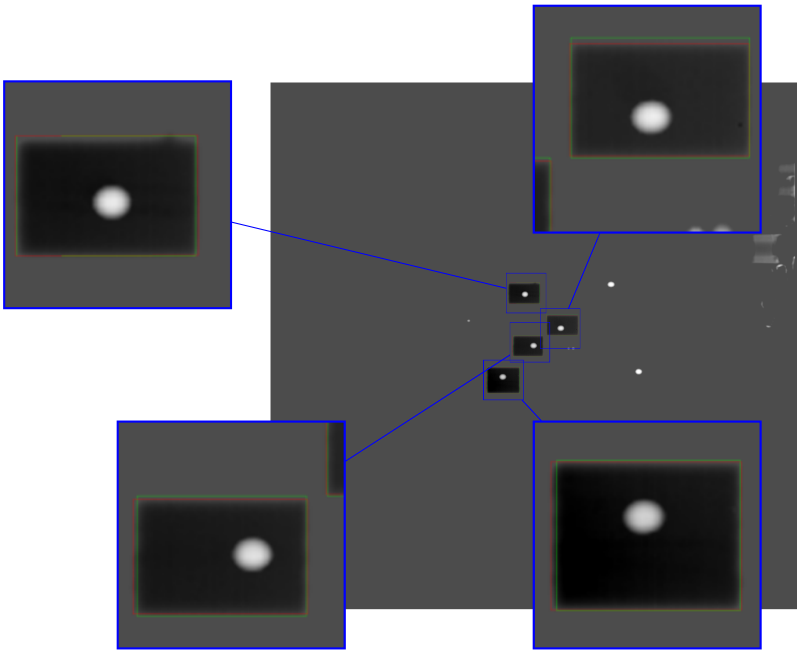

Figure 3.46: Blended LAT G DRR and LAT G Portal images - irradiation fields.

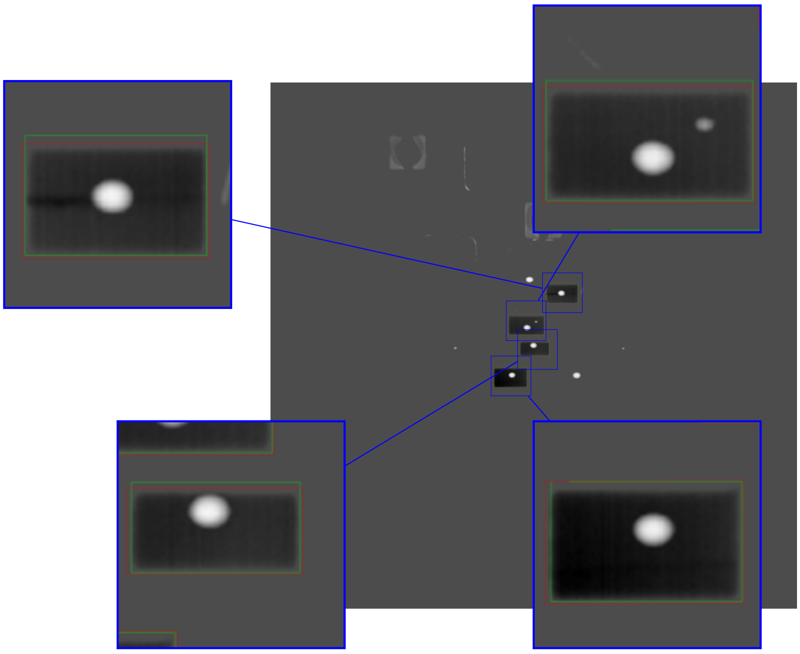

Figure 3.47: Blended POST DRR and POST Portal images - irradiation fields.

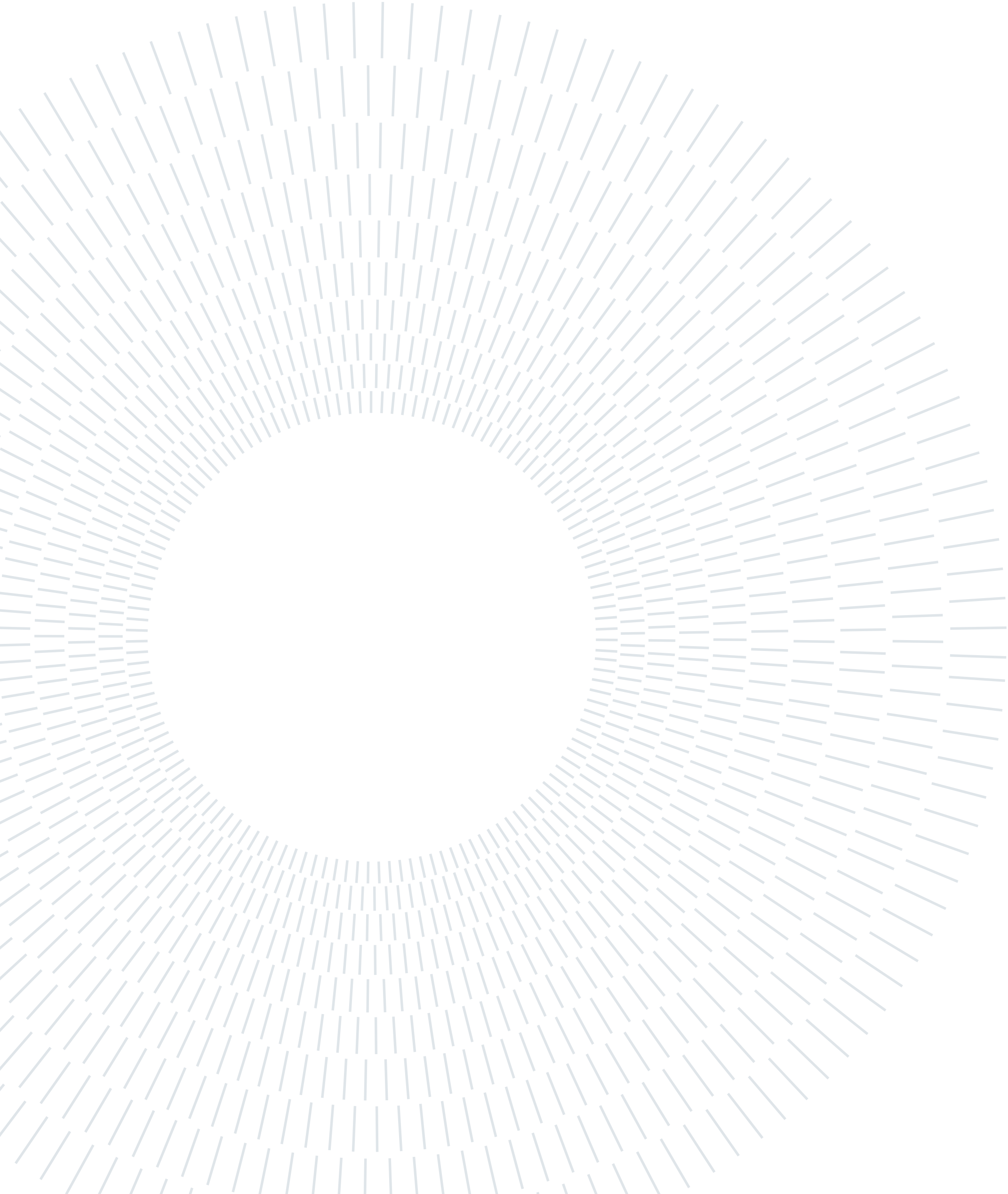

4 Results and Discussion

This chapter will present the results for the different phases of the workflow we described in the previous section.

4.1. Sphere Detection Evaluation

The first aim of the project is to quantify the shifts between corresponding spheres in DRR and Portal images. As already described, the process of circle identification is performed in both DRR images and Portal images. In DRR images, the positions of the spheres are expected to be the ground truth ones, while in Portal images they are detected through the EPI system. We report in Tables 4.1 and 4.2 the pixel coordinates of the detected sphere centers in both DRR and Portal images, ordered by their distance from the image center.

ANT DRR Image	**Coordinates of sphere centers**
	(3823, 3822), (3911, 3575), (4155, 4276), (3412, 3046)
LAT D DRR Image	**Coordinates of sphere centers**
	(3823, 3822), (3432, 3571), (4253, 4254), (3955, 3034)
LAT G DRR Image	**Coordinates of sphere centers**
	(3822, 3823), (4216, 3566), (3374, 4272), (3697, 3074)
POST DRR Image	**Coordinates of sphere centers**
	(3822, 3822), (3728, 3564), (3509, 4253), (4226, 3065)

Table 4.1: Coordinates of detected sphere centers - DRR Images.

ANT Portal Image	**Coordinates of sphere centers**
	(3832, 3820), (3920, 3576), (4166, 4278), (3418, 3046)
LAT D Portal Image	**Coordinates of sphere centers**
	(3818, 3820), (3428, 3574), (4250, 4254), (3950, 3034)
LAT G Portal Image	**Coordinates of sphere centers**
	(3824, 3818), (4228, 3562), (3378, 4270), (3704, 3074)
POST Portal Image	**Coordinates of sphere centers**
	(3814, 3812), (3712, 3558), (3492, 4250), (4214, 3062)

Table 4.2: Coordinates of detected sphere centers - Portal Images.

To check the effectiveness of the shape identification algorithm, we compared these centers with the centers measured by hand by a skilled medical physicist operator through 3D Slicer. This comparison has been made just to test the accuracy, it is clear that from a practical point of view, it would not be useful to manually identify spheres, since the purpose of the project is to automatize and speed up the entire process. The results are shown in Tables 4.3 and 4.4. The subsequent Figures display all the comparisons between the two methods, divided into X and Y-coordinates separately for each sphere in each DRR image.

ANT DRR Image	Coordinates of sphere centers
	(3824, 3824), (3913.625, 3572.0625), (4152.625, 4272.125), (3410.75, 3047.25)
LAT D DRR Image	**Coordinates of sphere centers**
	(3824, 3824), (3435.625, 3570.0625), (4255.1875, 4257.1875), (3956.4375, 3032.3125)
LAT G DRR Image	**Coordinates of sphere centers**
	(3824, 3824), (4214.375, 3570.0625), (3375.875, 4272.125), (3700.5, 3075.125)
POST DRR Image	**Coordinates of sphere centers**
	(3824, 3824), (3730.375, 3565.0635), (3510.3125, 4257.1875), (4227.3125, 3062.1875)

Table 4.3: Coordinates of sphere centers manually labeled - DRR Images.

ANT Portal Image	Coordinates of sphere centers
	(3830.8, 3820.8), (3924.64, 3572.72), (4167.52, 4273.6), (3420.24, 3046.4)
LAT D Portal Image	**Coordinates of sphere centers**
	(3822.72, 3819.84), (3434.16, 3568.88), (4253.44, 4254.8), (3951.16, 3034.32)
LAT G Portal Image	**Coordinates of sphere centers**
	(3829.92, 3816.96), (4229.44, 3562.64), (3380.4, 4271.68), (3702.64, 3069.36)
POST Portal Image	**Coordinates of sphere centers**
	(3815.28, 3820.4), (3716.4, 3556.56), (3496.08, 4247.28), (4216.96, 3057.36)

Table 4.4: Coordinates of sphere centers manually labeled - Portal Images.

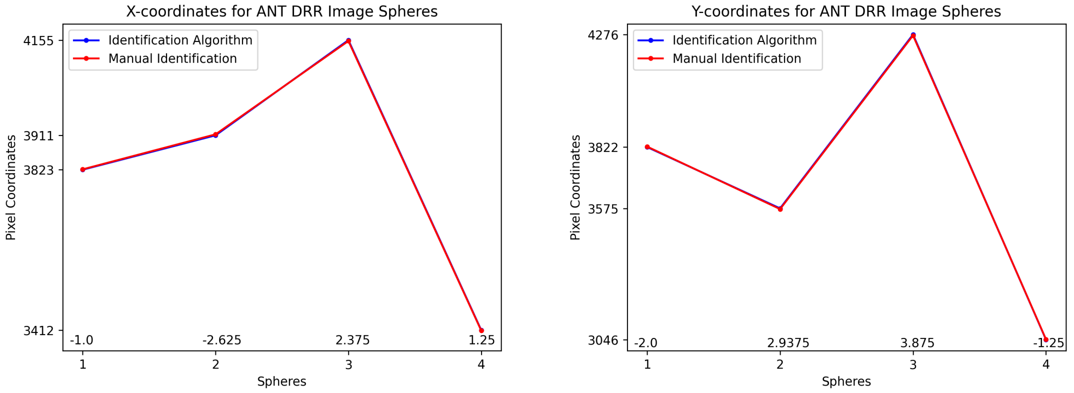

(a) X-coordinates for ANT DRR Image Spheres.

(b) Y-coordinates for ANT DRR Image Spheres.

Figure 4.1: Comparison between identification algorithm and manual identification for X and Y-coordinates in ANT DRR Image Spheres.

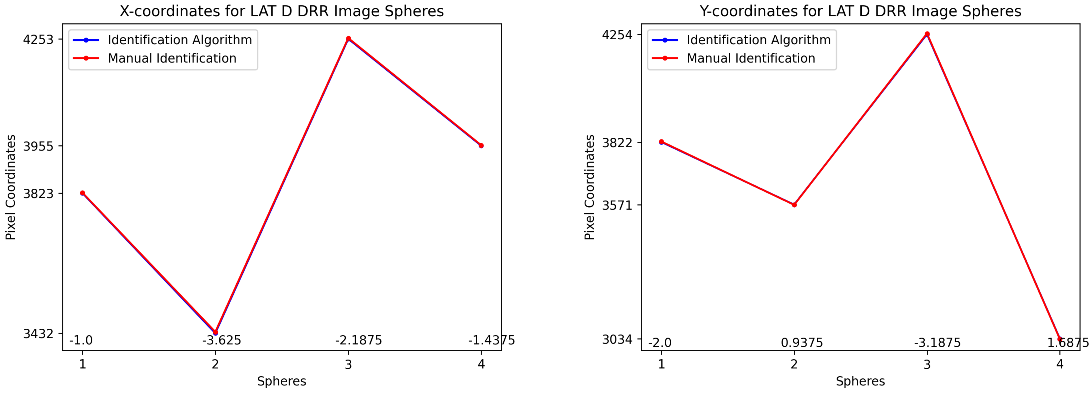

(a) X-coordinates for LAT D DRR Image Spheres.

(b) Y-coordinates for LAT D DRR Image Spheres.

Figure 4.2: Comparison between identification algorithm and manual identification for X and Y-coordinates in LAT D DRR Image Spheres.

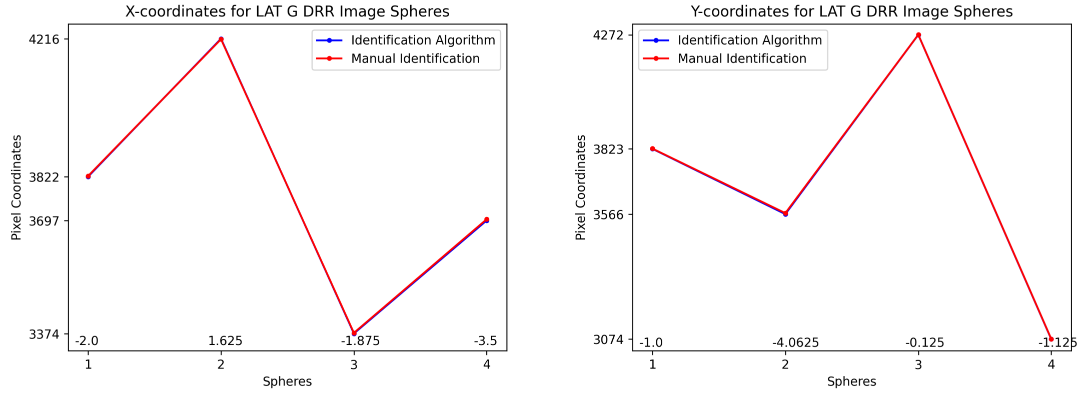

(a) X-coordinates for LAT G DRR Image Spheres.

(b) Y-coordinates for LAT G DRR Image Spheres.

Figure 4.3: Comparison between identification algorithm and manual identification for X and Y-coordinates in LAT G DRR Image Spheres.

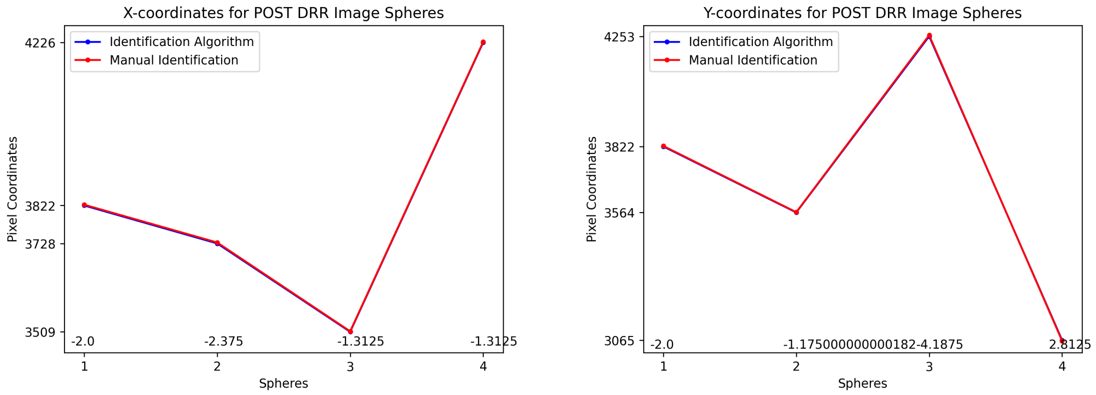

(a) X-coordinates for POST DRR Image Spheres.

(b) Y-coordinates for POST DRR Image Spheres.

Figure 4.4: Comparison between identification algorithm and manual identification for X and Y-coordinates in POST DRR Image Spheres.

In Table 4.5, we present the 2D Euclidean distances in pixel coordinates and millimeters as the difference between the two different identification methods, for each DRR Image and for each sphere. This will give an idea of the accuracy between the two methods. We can notice that in general we never exceed $0.3mm$ of difference between the two methods. These results certainly depend thanks to high contrast that characterizes DRR Images. It is easier for the algorithm as well as for the operator to clearly identify spheres and their centers, without facing artifacts or sources of imperfections. In particular, we have $0.20395mm$, $0.197mm$, $0.198725mm$, and $0.21185mm$ as 2D difference mean values for ANT, LAT D, LAT G, and POST DRR images, respectively.

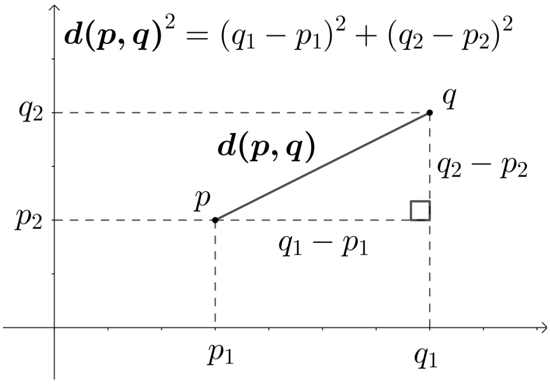

Figure 4.5: 2D Euclidean Distance.

ANT DRR Image	**Difference [*pixels coordinates*]**	**Difference [*mm*]**
	Sphere 1 = 2.2360	Sphere 1 = 0.1460
	Sphere 2 = 3.93948	Sphere 2 = 0.2574
	Sphere 3 = 4.5449	Sphere 3 = 0.2969
	Sphere 4 = 1.76777	Sphere 4 = 0.1155
LAT D DRR Image	**Difference [*pixels coordinates*]**	**Difference [*mm*]**
	Sphere 1 = 2.2360	Sphere 1 = 0.1460
	Sphere 2 = 3.7442	Sphere 2 = 0.2446
	Sphere 3 = 3.8659	Sphere 3 = 0.2526
	Sphere 4 = 2.2167	Sphere 4 = 0.1448
LAT G DRR Image	**Difference [*pixels coordinates*]**	**Difference [*mm*]**
	Sphere 1 = 2.2360	Sphere 1 = 0.1460
	Sphere 2 = 4.3754	Sphere 2 = 0.2859
	Sphere 3 = 1.8792	Sphere 3 = 0.1228
	Sphere 4 = 3.6764	Sphere 4 = 0.2402
POST DRR Image	**Difference [*pixels coordinates*]**	**Difference [*mm*]**
	Sphere 1 = 2.8284	Sphere 1 = 0.1848
	Sphere 2 = 2.6497	Sphere 2 = 0.1731
	Sphere 3 = 4.3884	Sphere 3 = 0.2867
	Sphere 4 = 3.1037	Sphere 4 = 0.2028

Table 4.5: Difference between manually identified and algorithm identified spheres for each DRR image as 2D Euclidean distance.

The same results are displayed also for Portal images. In Figures 4.6, 4.7, 4.8 and 4.9 we present the comparisons between the two methods for sphere identification in each Portal image. Table 4.6 presents the 2D Euclidian distances between the two different identification methods for each sphere in each Portal image. In this case, we have mean values of $0.229525mm$, $0.285275mm$, $0.234975mm$, and $0.38435mm$ for Portal images. The differences between the methods are still good but a bit higher with respect to the previous case. This is mainly caused by the lower signal-to-noise ratio as well as artifacts and physical factors during image acquisition present in Portal images.

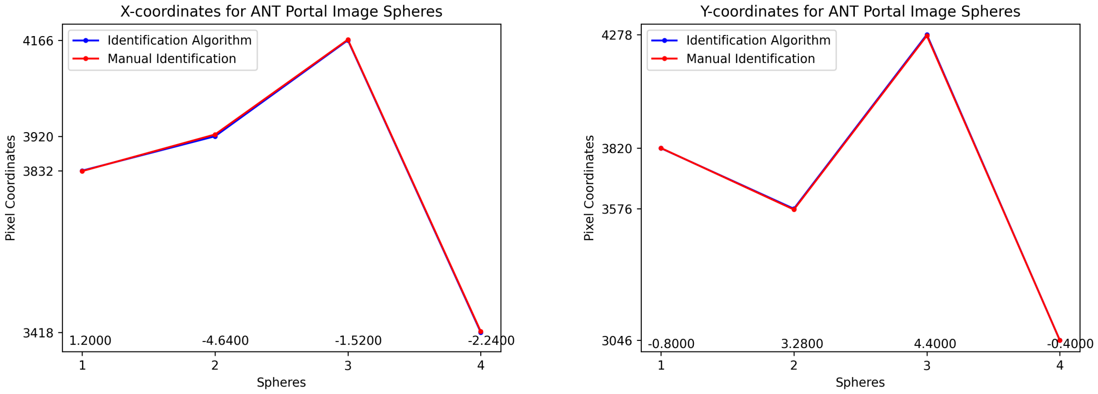

(a) X-coordinates for ANT Portal Image Spheres.

(b) Y-coordinates for ANT Portal Image Spheres.

Figure 4.6: Comparison between identification algorithm and manual identification for X and Y-coordinates in ANT Portal Image Spheres.

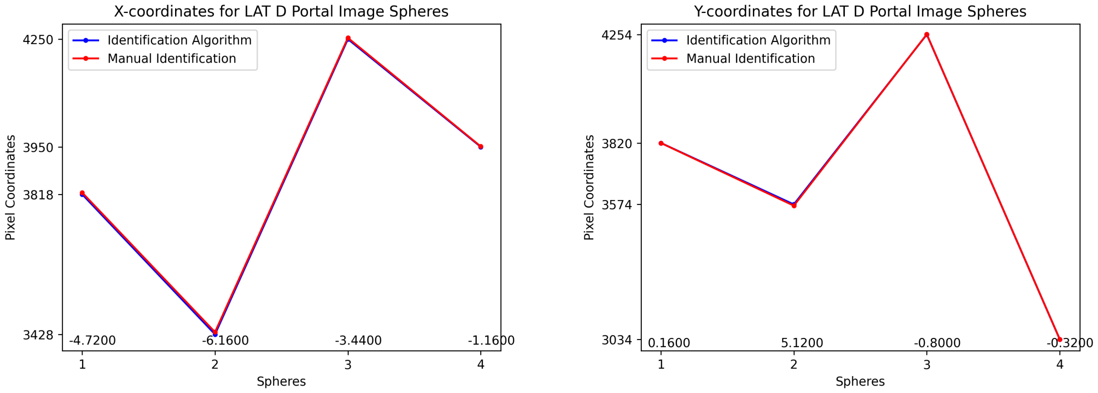

(a) X-coordinates for LAT D Portal Image Spheres.

(b) Y-coordinates for LAT D Portal Image Spheres.

Figure 4.7: Comparison between identification algorithm and manual identification for X and Y-coordinates in LAT D Portal Image Spheres.

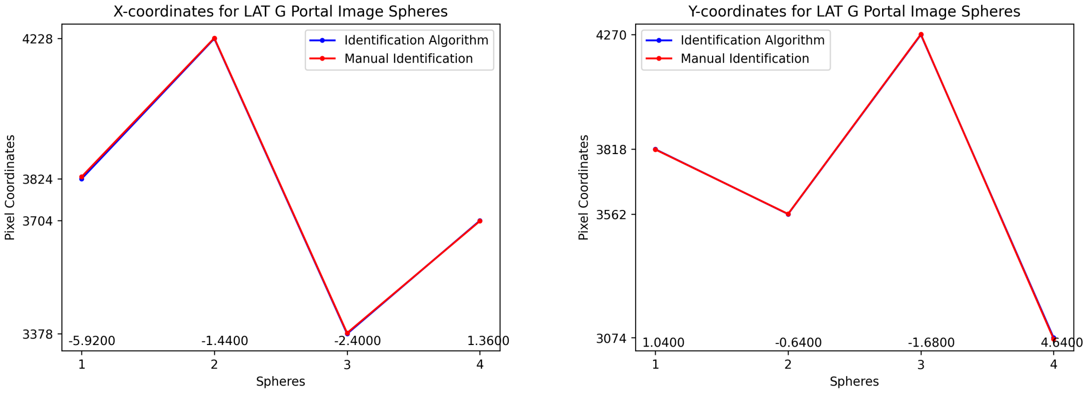

(a) X-coordinates for LAT G Portal Image Spheres.

(b) Y-coordinates for LAT G Portal Image Spheres.

Figure 4.8: Comparison between identification algorithm and manual identification for X and Y-coordinates in LAT G Portal Image Spheres.

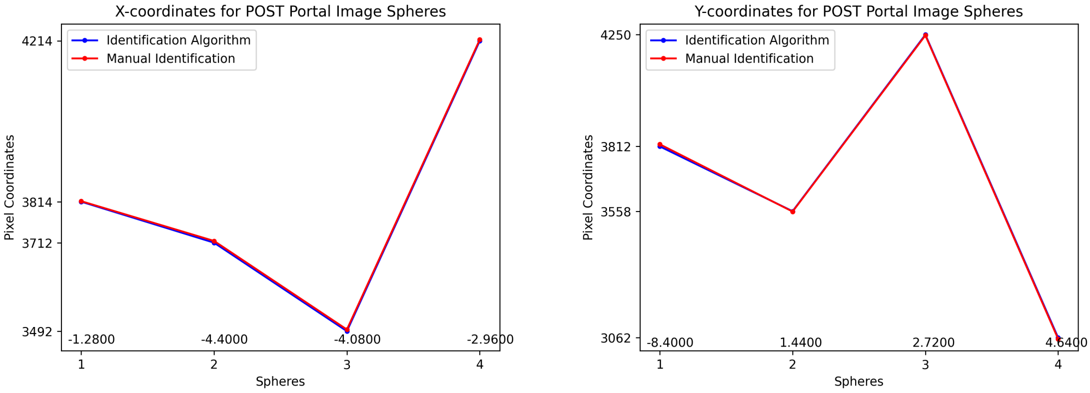

(a) X-coordinates for POST Portal Image Spheres.

(b) Y-coordinates for POST Portal Image Spheres.

Figure 4.9: Comparison between identification algorithm and manual identification for X and Y-coordinates in POST Portal Image Spheres.

ANT Portal Image	**Difference [*pixels coordinates*]**	**Difference [*mm*]**
	Sphere 1 = 1.44222 Sphere 2 = 5.68225 Sphere 3 = 4.65515 Sphere 4 = 2.27543	Sphere 1 = 0.0942 Sphere 2 = 0.3712 Sphere 3 = 0.3041 Sphere 4 = 0.1486
LAT D Portal Image	**Difference [*pixels coordinates*]**	**Difference [*mm*]**
	Sphere 1 = 4.72271 Sphere 2 = 8.00999 Sphere 3 = 3.53179 Sphere 4 = 1.20332	Sphere 1 = 0.3085 Sphere 2 = 0.5233 Sphere 3 = 0.2307 Sphere 4 = 0.0786
LAT G Portal Image	**Difference [*pixels coordinates*]**	**Difference [*mm*]**
	Sphere 1 = 6.01065 Sphere 2 = 1.57581 Sphere 3 = 2.92957 Sphere 4 = 4.83520	Sphere 1 = 0.3927 Sphere 2 = 0.1029 Sphere 3 = 0.1914 Sphere 4 = 0.3159
POST Portal Image	**Difference [*pixels coordinates*]**	**Difference [*mm*]**
	Sphere 1 = 8.49696 Sphere 2 = 4.62964 Sphere 3 = 4.90354 Sphere 4 = 5.50374	Sphere 1 = 0.5551 Sphere 2 = 0.3024 Sphere 3 = 0.3203 Sphere 4 = 0.3596

Table 4.6: Difference between manually identified and algorithm identified spheres for each Portal image as 2D Euclidean distance.

4.2. Sphere Displacement Evaluation

We present here the results for what concerns the first objective of this work: the measurement of displacements between corresponding spheres in DRR and Portal images. We evaluated these displacements firstly considering the results coming from the identification algorithm, and then considering manual annotation. We measured the displacements through 2D Euclidean distance of pixel coordinates for each pair of spheres in superimposed DRR and Portal images. The displacements represent the accuracy of the registration phase and the alignment of the EPI system with the OBI system and all the other LINAC components.

ANT Images	**Displacement [mm]**
	Sphere 1 = 0.6023
	Sphere 2 = 0.5916
	Sphere 3 = 0.7304
	Sphere 4 = 0.3918
LAT D Images	**Displacement [mm]**
	Sphere 1 = 0.3518
	Sphere 2 = 0.3266
	Sphere 3 = 0.1956
	Sphere 4 = 0.3267
POST Images	**Displacement [mm]**
	Sphere 1 = 0.3518
	Sphere 2 = 0.8264
	Sphere 3 = 0.2921
	Sphere 4 = 0.4573
LAT G Images	**Displacement [mm]**
	Sphere 1 = 0.83664
	Sphere 2 = 1.1163
	Sphere 3 = 1.1277
	Sphere 4 = 0.8081

Table 4.7: Measured displacements between correspondent spheres in DRR and Portal images - identification algorithm.

ANT Images	**Displacement [mm]**
	Sphere 1 = 0.5843
	Sphere 2 = 0.4895
	Sphere 3 = 0.9544
	Sphere 4 = 0.4806
LAT D Images	**Displacement [mm]**
	Sphere 1 = 0.4711
	Sphere 2 = 0.5139
	Sphere 3 = 0.3977
	Sphere 4 = 0.4347
POST Images	**Displacement [mm]**
	Sphere 1 = 1.0205
	Sphere 2 = 0.8612
	Sphere 3 = 1.2852
	Sphere 4 = 0.8698
LAT G Images	**Displacement [mm]**
	Sphere 1 = 0.3919
	Sphere 2 = 1.0343
	Sphere 3 = 0.1963
	Sphere 4 = 0.2401

Table 4.8: Measured displacements between correspondent spheres in DRR and Portal images - manual annotation.

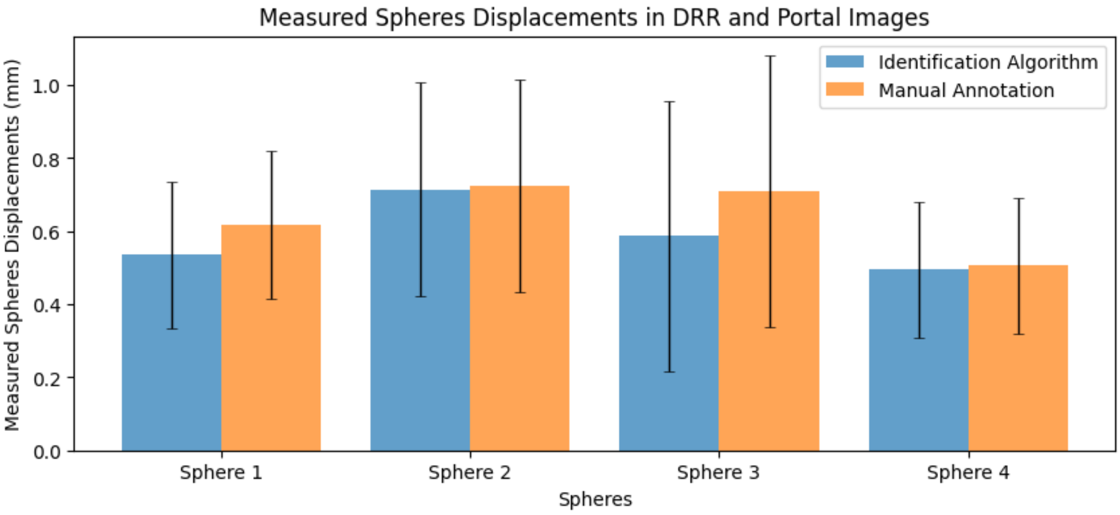

Figure 4.10: Measured Spheres Displacements in DRR and Portal images.

Figure 4.10 shows the displacements' distribution for each sphere, by comparing the two different methods for sphere identification. Overall, we can see how the two methods lead to similar results for each sphere among different images. Moreover, it is clear how all the values are strictly below the threshold of $1.5mm$, which is considered the maximum allowed displacement for this standard of RT operation. In particular, for what concerns the identification algorithm, the peaks involve Sphere 2 and Sphere 3 in LAT G images with $1.1163mm$ and $1.1277mm$, while considering the manual annotation, we have Sphere 1 and Sphere 3 in POST images - with $1.0205mm$ and $1.2852mm$ - and Sphere 2 in LAT G images - with $1.0343mm$.

4.3. Irradiation Field Displacement Evaluation

In this section, we present the results linked to the second main purpose of this project: the measurement of displacements between corresponding irradiation fields in DRR and Portal images. As explained in the methods chapter, the principle of measurement follows the one previously presented. Thus, couples of corresponding irradiation fields, belonging to paired spheres, are superimposed and their distances are then computed.

In order to compute the distances, we use two metrics. The first one is the Intersection over Union (IoU), which quantifies the degree of overlap between the ground truth box and the detected one. IoU values range from 0 to 1. Where 0 means no overlap and 1 means perfect overlap (Figure 4.11). The second one, on the other hand, simply measures the displacements between each corresponding edge of correspondent irradiation fields. The maximum allowed displacement for each edge is still $1.5mm$, as in the case of spheres. It represents the desired threshold of geometrical accuracy for single isocenter and multi-target therapies in our Institute.

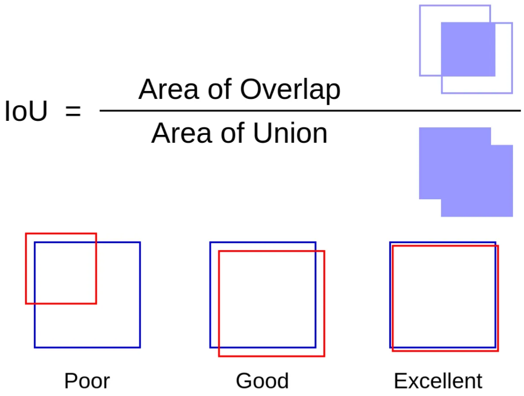

Figure 4.11: Intersection over Union.

Moreover, here we only consider the reconstructed coordinates from DICOM tags as ground truth irradiation fields, and the algorithm-identified coordinates as the detected irradiation fields. It is different from the previous case where we also reported the annotated coordinates. This happens because we do not need to check the effectiveness of reconstructed coordinates. They are given as metadata and not computed through a developed algorithm. In Tables 4.9, 4.10, 4.11, 4.12 we report the pixel coordinates of each irradiation field for all DRR images, reconstructed from the information contained in DICOM headers. In Tables 4.13, 4.14, 4.15, 4.16 we present the pixel coordinates of each irradiation field for all Portal images, computed through the shape recognition algorithm.

Irradiation Field 1	
Corner	**Pixel Coordinates**
Top Right	(4399.6833480367, 4130.133128442808)
Top Left	(3913.8500731979643, 4130.133128442808)
Bottom Left	(3913.8500731979643, 4436.266256885617)
Bottom Right	(4399.6833480367, 4436.266256885617)
Irradiation Field 2	
Corner	**Pixel Coordinates**
Top Right	(4025.588665079589, 3747.466717889298)
Top Left	(3594.553220232115, 3747.466717889298)
Bottom Left	(3594.553220232115, 3977.066564221404)
Bottom Right	(4025.588665079589, 3977.066564221404)
Irradiation Field 3	
Corner	**Pixel Coordinates**
Top Right	(4192.7373532093625, 3364.8003073357877)
Top Left	(3666.6475719803966, 3364.8003073357877)
Bottom Left	(3666.6475719803966, 3670.933435778596)
Bottom Right	(4192.7373532093625, 3670.933435778596)
Irradiation Field 4	
Corner	**Pixel Coordinates**
Top Right	(3643.8406539114076, 2905.6006146715754)
Top Left	(3180.81429714166, 2905.6006146715754)
Bottom Left	(3180.81429714166, 3211.7337431143837)
Bottom Right	(3643.8406539114076, 3211.7337431143837)

Table 4.9: DRR ANT Image Irradiation Fields Coordinates.

Irradiation Field 1

Corner	Pixel Coordinates
Top Right	(4496.115283496185, 4130.133128442808)
Top Left	(4028.190796671353, 4130.133128442808)
Bottom Left	(4028.190796671353, 4512.799538996318)
Bottom Right	(4496.115283496185, 4512.799538996318)

Irradiation Field 2

Corner	Pixel Coordinates
Top Right	(4121.102201153745, 3670.933435778596)
Top Left	(3689.4544900493856, 3670.933435778596)
Bottom Left	(3689.4544900493856, 3977.066564221404)
Bottom Right	(4121.102201153745, 3977.066564221404)

Irradiation Field 3

Corner	Pixel Coordinates
Top Right	(3635.881192571894, 3364.8003073357877)
Top Left	(3180.81429714166, 3364.8003073357877)
Bottom Left	(3180.81429714166, 3670.933435778596)
Bottom Right	(3635.881192571894, 3670.933435778596)

Irradiation Field 4

Corner	Pixel Coordinates
Top Right	(4192.7373532093625, 2905.6006146715754)
Top Left	(3737.5173912149066, 2905.6006146715754)
Bottom Left	(3737.5173912149066, 3211.7337431143837)
Bottom Right	(4192.7373532093625, 3211.7337431143837)

Table 4.10: DRR LAT D Image Irradiation Fields Coordinates.

Irradiation Field 1

Corner	**Pixel Coordinates**
Top Right	(3734.1499268020357, 4130.133128442808)
Top Left	(3248.316651963299, 4130.133128442808)
Bottom Left	(3248.316651963299, 4436.266256885617)
Bottom Right	(3734.1499268020357, 4436.266256885617)

Irradiation Field 2

Corner	**Pixel Coordinates**
Top Right	(4053.446779767885, 3747.466717889298)
Top Left	(3622.411334920411, 3747.466717889298)
Bottom Left	(3622.411334920411, 3977.066564221404)
Bottom Right	(4053.446779767885, 3977.066564221404)

Irradiation Field 3

Corner	**Pixel Coordinates**
Top Right	(3981.3524280196034, 3364.8003073357877)
Top Left	(3455.2626467906375, 3364.8003073357877)
Bottom Left	(3455.2626467906375, 3670.933435778596)
Bottom Right	(3981.3524280196034, 3670.933435778596)

Irradiation Field 4

Corner	**Pixel Coordinates**
Top Right	(4467.18570285834, 2905.6006146715754)
Top Left	(4004.1593460885924, 2905.6006146715754)
Bottom Left	(4004.1593460885924, 3211.7337431143837)
Bottom Right	(4467.18570285834, 3211.7337431143837)

Table 4.11: DRR POST Image Irradiation Fields Coordinates.

Irradiation Field 1	
Corner	**Pixel Coordinates**
Top Right	(3619.809203328647, 4130.133128442808)
Top Left	(3151.8847165038146, 4130.133128442808)
Bottom Left	(3151.8847165038146, 4512.799538996318)
Bottom Right	(3619.809203328647, 4512.799538996318)

Irradiation Field 2	
Corner	**Pixel Coordinates**
Top Right	(3958.5455099506144, 3670.933435778596)
Top Left	(3526.897798846255, 3670.933435778596)
Bottom Left	(3526.897798846255, 3977.066564221404)
Bottom Right	(3958.5455099506144, 3977.066564221404)

Irradiation Field 3	
Corner	**Pixel Coordinates**
Top Right	(4467.18570285834, 3364.8003073357877)
Top Left	(4012.118807428106, 3364.8003073357877)
Bottom Left	(4012.118807428106, 3670.933435778596)
Bottom Right	(4467.18570285834, 3670.933435778596)

Irradiation Field 4	
Corner	**Pixel Coordinates**
Top Right	(3910.4826087850934, 2905.6006146715754)
Top Left	(3455.2626467906375, 2905.6006146715754)
Bottom Left	(3455.2626467906375, 3211.7337431143837)
Bottom Right	(3910.4826087850934, 3211.7337431143837)

Table 4.12: DRR LAT G Image Irradiation Fields Coordinates.

Irradiation Field 1	
Corner	**Pixel Coordinates**
Top Right	(4404, 4126)
Top Left	(3896, 4122)
Bottom Left	(3896, 4432)
Bottom Right	(4402, 4435)

Irradiation Field 2	
Corner	**Pixel Coordinates**
Top Right	(4027, 3754)
Top Left	(3580, 3754)
Bottom Left	(3580, 3971)
Bottom Right	(4027, 3971)

Irradiation Field 3	
Corner	**Pixel Coordinates**
Top Right	(4195, 3376)
Top Left	(3655, 3373)
Bottom Left	(3653, 3666)
Bottom Right	(4193, 3669)

Irradiation Field 4	
Corner	**Pixel Coordinates**
Top Right	(3642, 2913)
Top Left	(3167, 2913)
Bottom Left	(3167, 3208)
Bottom Right	(3642, 3208)

Table 4.13: ANT Portal Image Irradiation Fields Coordinates.

Irradiation Field 1

Corner	Pixel Coordinates
Top Right	(4502, 4140)
Top Left	(4013, 4140)
Bottom Left	(4013, 4516
Bottom Right	(4502, 4516)

Irradiation Field 2

Corner	Pixel Coordinates
Top Right	(4122, 3686)
Top Left	(3680, 3686)
Bottom Left	(3680, 3977)
Bottom Right	(4122, 3977)

Irradiation Field 3

Corner	Pixel Coordinates
Top Right	(3633, 3384)
Top Left	(3176, 3384)
Bottom Left	(3176, 3671)
Bottom Right	(3633, 3671)

Irradiation Field 4

Corner	Pixel Coordinates
Top Right	(4194, 2912)
Top Left	(3729, 2907)
Bottom Left	(3725, 3213)
Bottom Right	(4190, 3219)

Table 4.14: LAT D Portal Image Irradiation Fields Coordinates.

Irradiation Field 1

Corner	**Pixel Coordinates**
Top Right	(3737, 4126)
Top Left	(3231, 4130)
Bottom Left	(3233, 4442)
Bottom Right	(3739, 4439)

Irradiation Field 2

Corner	**Pixel Coordinates**
Top Right	(4060, 3760)
Top Left	(3611, 3760)
Bottom Left	(3611, 3980)
Bottom Right	(4060, 3980)

Irradiation Field 3

Corner	**Pixel Coordinates**
Top Right	(3986, 3379)
Top Left	(3447, 3379)
Bottom Left	(3447, 3675)
Bottom Right	(3986, 3675)

Irradiation Field 4

Corner	**Pixel Coordinates**
Top Right	(4474, 2926)
Top Left	(3996, 2926)
Bottom Left	(3996, 3219)
Bottom Right	(4474, 3219)

Table 4.15: POST Portal Image Irradiation Fields Coordinates.

<table>
<tr><th colspan="2">Irradiation Field 1</th></tr>
<tr><th>Corner</th><th>Pixel Coordinates</th></tr>
<tr><td>Top Right</td><td>(3623, 4134)</td></tr>
<tr><td>Top Left</td><td>(3137, 4134)</td></tr>
<tr><td>Bottom Left</td><td>(3137, 4511)</td></tr>
<tr><td>Bottom Right</td><td>(3623, 4511)</td></tr>
<tr><th colspan="2">Irradiation Field 2</th></tr>
<tr><th>Corner</th><th>Pixel Coordinates</th></tr>
<tr><td>Top Right</td><td>(3962, 3680)</td></tr>
<tr><td>Top Left</td><td>(3517, 3680)</td></tr>
<tr><td>Bottom Left</td><td>(3517, 3972)</td></tr>
<tr><td>Bottom Right</td><td>(3962, 3972)</td></tr>
<tr><th colspan="2">Irradiation Field 3</th></tr>
<tr><th>Corner</th><th>Pixel Coordinates</th></tr>
<tr><td>Top Right</td><td>(4466, 3380)</td></tr>
<tr><td>Top Left</td><td>(4009, 3380)</td></tr>
<tr><td>Bottom Left</td><td>(4009, 3667)</td></tr>
<tr><td>Bottom Right</td><td>(4466, 3667)</td></tr>
<tr><th colspan="2">Irradiation Field 4</th></tr>
<tr><th>Corner</th><th>Pixel Coordinates</th></tr>
<tr><td>Top Right</td><td>(3916, 2904)</td></tr>
<tr><td>Top Left</td><td>(3451, 2906)</td></tr>
<tr><td>Bottom Left</td><td>(3452, 3212)</td></tr>
<tr><td>Bottom Right</td><td>(3917, 3210)</td></tr>
</table>

Table 4.16: LAT G Portal Image Irradiation Fields Coordinates.

ANT Image	
Irradiation Field	**IoU**
Irradiation Field 1	0.93154
Irradiation Field 2	0.91315
Irradiation Field 3	0.93351
Irradiation Field 4	0.93297

LAT D Image	
Irradiation Field	**IoU**
Irradiation Field 1	0.92551
Irradiation Field 2	0.92937
Irradiation Field 3	0.92200
Irradiation Field 4	0.94946

POST Image	
Irradiation Field	**IoU**
Irradiation Field 1	0.94054
Irradiation Field 2	0.89807
Irradiation Field 3	0.91958
Irradiation Field 4	0.88496

LAT G	
Irradiation Field	**IoU**
Irradiation Field 1	0.94907
Irradiation Field 2	0.92649
Irradiation Field 3	0.92908
Irradiation Field 4	0.97445

Table 4.17: IoU metrics for each irradiation field in all images.

ANT Images	
Irradiation Field	**Edge Displacement [mm]**
Irradiation Field 1	Top = 0.53134, Bottom = 0.27871, Left = 0.11661, Right = 0.28201
Irradiation Field 2	Top = 0.42682, Bottom = 0.39633, Left = 0.95077, Right = 0.09229
Irradiation Field 3	Top = 0.73168, Bottom = 0.32230, Left = 0.89161, Right = 0.14782
Irradiation Field 4	Top = 0.48340, Bottom = 0.24392, Left = 0.90250, Right = 0.12025
LAT D Images	
Irradiation Field	**Edge Displacement [mm]**
Irradiation Field 1	Top = 0.64461, Bottom = 0.20908, Left = 0.99243, Right = 0.38445
Irradiation Field 2	Top = 0.98431, Bottom = 0.04348, Left = 0.61767, Right = 0.05865
Irradiation Field 3	Top = 1.25433, Bottom = 0.04348, Left = 0.31452, Right = 0.18823
Irradiation Field 4	Top = 0.41807, Bottom = 0.47471, Left = 0.81777, Right = 0.17883
POST Images	
Irradiation Field	**Edge Displacement [mm]**
Irradiation Field 1	Top = 0.27002, Bottom = 0.37459, Left = 1.13131, Right = 0.31680
Irradiation Field 2	Top = 0.81881, Bottom = 0.19164, Left = 0.74551, Right = 0.42812
Irradiation Field 3	Top = 0.92768, Bottom = 0.26567, Left = 0.53980, Right = 0.30363
Irradiation Field 4	Top = 1.33271, Bottom = 0.47471, Left = 0.53305, Right = 0.44551
LAT G Images	
Irradiation Field	**Edge Displacement [mm]**
Irradiation Field 1	Top = 0.25262, Bottom = 0.11756, Left = 0.97243, Right = 0.20845

LAT G Images	
Irradiation Field	**Edge Displacement [mm]**
Irradiation Field 2	Top = 0.59232, Bottom = 0.33100, Left = 0.64663, Right = 0.22568
Irradiation Field 3	Top = 0.99301, Bottom = 0.25697, Left = 0.20375, Right = 0.07746
Irradiation Field 4	Top = 0.10456, Bottom = 0.11326, Left = 0.27848, Right = 0.42578

Table 4.18: Edge displacement for each irradiation field in all paired images.

In Table 4.18, we present all the displacements between corresponding edges of coupled irradiation fields on paired DRR and Portal images. In particular, the irradiation fields are ordered from their lower to their higher Y-axis coordinates i.e. Irradiation Field 1 represents the bottom one by looking at the image, while Irradiation Field 4 the higher one. Also, the edge displacements have been computed by considering the maximum value between the differences of the paired coordinates of the extremes for each edge. For example, if we consider the Irradiation Field 1 for ANT Images, we exploit the following formulas:

$$\begin{split}\max\{&|DRR\_first\_point\_X\_coordinate - Portal\_first\_point\_X\_coordinate|,\\ &|DRR\_second\_point\_X\_coordinate - Portal\_second\_point\_X\_coordinate|\}\end{split} \tag{4.1}$$

$$\begin{split}\max\{&|DRR\_first\_point\_Y\_coordinate - Portal\_first\_point\_Y\_coordinate|,\\ &|DRR\_second\_point\_Y\_coordinate - Portal\_second\_point\_Y\_coordinate|\}\end{split} \tag{4.2}$$

The first one is used when we need to measure the Left or the Right displacement since they involve X-coordinates. The second one is when we have to compute the Top or Bottom displacement since they involve Y-coordinates. We use the max function so that we take into consideration the worst case among the two extremes of each edge. We can see how in general all the displacements fall in the desired threshold of $1.5mm$. There are a few peaks of $1.33271mm$ and $1.25433mm$, while all the other cases are below $1mm$.

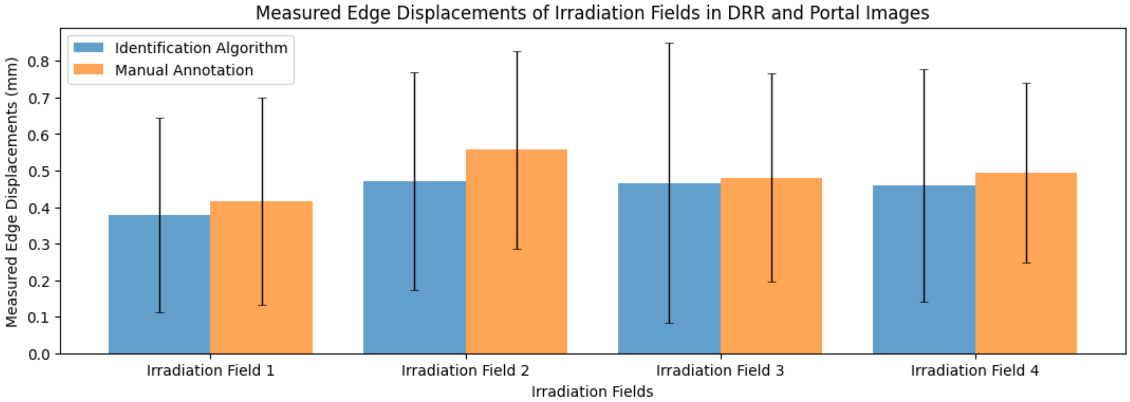

Figure 4.12: Measured averaged edge displacements for each irradiation field between DRR and Portal Images.

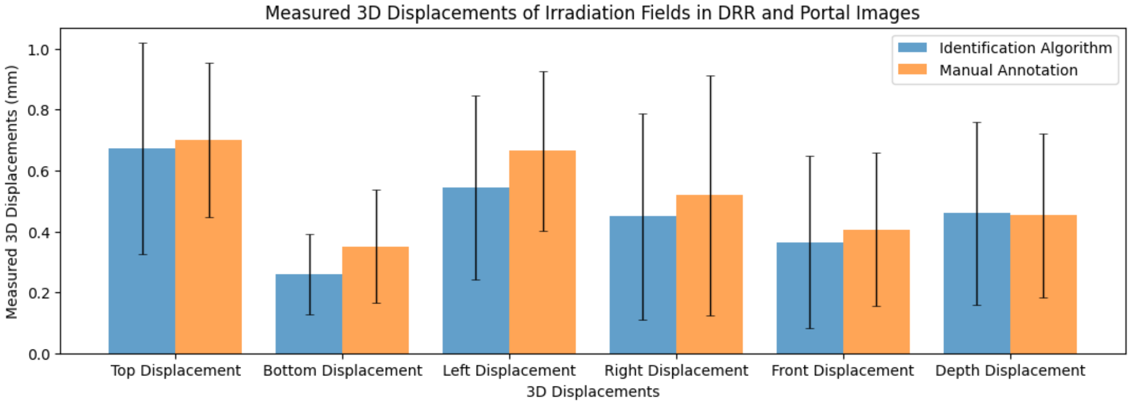

Figure 4.13: Measured 3D displacements averaging all irradiation fields of DRR and Portal Images.

Figure 4.12 shows the measured displacements for each irradiation field among all DRR and Portal images compared with the manual annotation process. They have been computed by averaging all the edge shifts (Top, Bottom, Left, Right) from all paired images. The results are reported in mm, obtained by converting pixel coordinates displacements. Figure 4.13 instead, implements the averaged displacements from a 3D perspective. We know that all 2D irradiation fields are projections of the 3D volume (Figure 4.14). In particular, Top, Bottom, Left, Right, Front, and Depth displacements, refer to the namesake 3D volume faces considering the anterior point of view. For example, Top displacement is given by the average of all Top edge displacements from Table 4.18, since they all refer to the Top face of the 3D volume. Again, Front displacement for example is given by averaging Left edge displacements from LAT G images and Right edge displacements from LAT D images, since they are related to the Front face of the volume, still from Table 4.18.

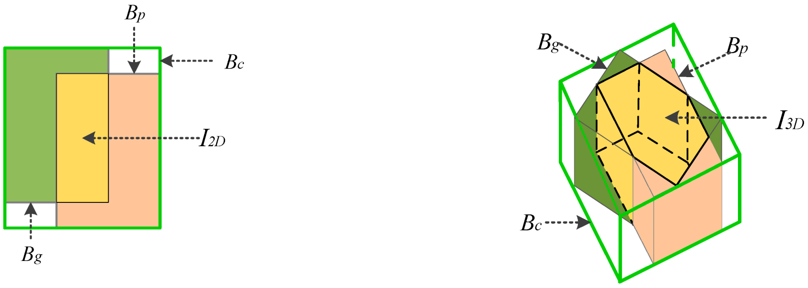

(a) 2D **(b)** 3D

Figure 4.14: 2D displacements of 3D volume.

Moreover, performances of the automatized process through our developed program were timed, and compared with the manually-performed process. Table 4.19, shows their mean values and the total time for each method, divided into their phases.

For what concerns the manual process, we considered the execution of expert medical physicians and we took average values for each phase. In this case, the more time-consuming phases are the sphere and irradiation field detections as well as the computation of their displacements. Superscaling and irradiation field reconstruction are not considered since they are proper features of the developed program. Sphere selection also is not taken into consideration since it refers to the phase of manually selecting bounding boxes around each Portal image sphere, still proper of the automatized process.

With regard to the automatized process, the two time-requiring phases are sphere selection and irradiation field detection. The first one is due to the fact that it is still the only manual step required, while the second one, on the other hand, is caused by the necessity to perform image processing on 7648x7648 dimensions.

It is clear that from a computational point of view, the procedure executed by our developed program is way faster than the manual process, allowing us to speed up the entire pipeline of execution by 88%.

Phases	**Developed Program**	**Manual Process**
Dataset Preparation	$5.4785 sec$	$2 min$
Resampling	$0.2947 sec$	$2 min$
Windowing	$5.6667 sec$	$3 min$
Superscaling	$17.8995 sec$	-
Spheres Selection	$1 min$	-
Spheres Detection	$15.3017 sec$	$4 min$
Spheres Displacements	$0.1587\ sec$	$4 min$
Irradiation Fields Reconstruction	$0.2866 sec$	-
Irradiation Fields Detection	$74.8430 sec$	$5 min$
Irradiation Fields Displacements	$0.0713 sec$	$5 min$
Total Time	$\approx 3 min$	$\approx 25 min$

Table 4.19: Total time required for the entire pipeline.

5 | Conclusions

In this work, a new automatic method was developed for measuring the displacements of multiple cranial phantom sphere targets and their irradiation fields on 2D Portal images, relative to their theoretical positions in 2D DRR images. In particular, the need for this solution arises from the problem that in IGRT SRT/SRS QA processes, the analysis is still manually performed by a medical physicist operator due to two main factors: firstly, MV images are subjected to significant noise and low contrast resolution, because of the high dose emitted. In addition, this type of treatment is characterized by a single isocenter and multiple targets, a rather new irradiation technique within our institute, which still needs automatized verification tests.

We first implemented a method for automatic image management, capable of extracting the necessary information from DICOM headers, standardizing images from different HUs, and preparing them for batch processes. We then realized the pipeline of preprocessing which, in order, performs the following operations: resampling, necessary to bring DRR and Portal images to the same SID value; windowing, important for filtering out unnecessary artifacts from images and standing out sphere targets; superscaling, used to increase image resolution by an x8 factor.

After that, we implemented a procedure for sphere shape recognition by exploiting a GUI and Hough Transform method, and sphere displacement between DRR and Portal paired images, after 2D/2D multi-modal superimposition. The results show that for each sphere the average shifts among all 4 paired images are below $0.8mm$, far below the $1.5mm$ tolerance. Similar results have been found by comparing our method with the displacement measurement after manual annotation for sphere identification.

We developed an automatic approach for theoretical irradiation fields reconstruction on DRR images, by analyzing DICOM metadata information about MLC and jaws, and irradiation field identification on Portal images, by exploiting Canny Edge detection method. We assessed how the average displacements between correspondent irradiation fields on matched images are below 0.7 mm, still much better than $1.5mm$ threshold.

Finally, we compared the developed program and the manual process in terms of procedural delays. The manual method, whose measurements have been considered performed by an expert medical physicist, takes approximately $25min$, while the automatic procedure required about $3min$, allowing a speed-up of 88%.

This process of automatic evaluation sits after the OBI registration phase in QA geometrical accuracy pipeline. It aims to be an end-to-end test for MV system as well as LINAC treatment head. In particular, the measured sphere displacements will represent misalignments between OBI and EPI systems or treatment couch correction problems, while irradiation field shifts could also depend on MLC or jaws mechanical calibration inaccuracies. It is a follow-up task to further investigate with specific tests and identify the source of error.

6 | Future Developments

The implemented automatic method makes use of four different gantry-angle images i.e. ANT, LAD D, LAT G, and POST. The four different gantry-angle images have been chosen since they are the minimum projections through which we are able to obtain 3D complete information about the volume while saving X-ray emission at the same time. However, this allows for an ad-hoc case study of this situation. In the future, still considering the study performed on sphere targets, it would be interesting to have a larger data set of the same projections in order to build a deep learning model for sphere identification. In this way, the time utilized for sphere selection would be removed and the overall process would see a further speed up. Also, having 2D projections from other gantry angles - for example oblique perspectives - could be an interesting integration for the program.

Additionally, in this work, several simplifications have been performed, which facilitate obtaining accurate results. For example, the spheres were located distantly among them, this made it easier to identify them through the Hough Transform. In the future, they could be positioned by partially overlapping, resulting in more similarity to a real case of close metastasis. Also, the composition material of the cranial phantom was rather homogenous, resulting in clear images after DRR reconstruction and MV irradiation. A phantom with different internal structures could be used in order to get closer to a real case where internal brain composition is highly heterogeneous. In this direction, a study on the ideal values for windowing - depending on the different materials - could be performed by building machine learning models. Moreover, the choice of having rectangular irradiation fields was also made in order to simplify the entire process. The recognition through bounding boxes is eased. Having irradiation fields adapted to target shapes would also represent a follow-up step.

This work lays the foundation for more advanced automatic measurement processes.

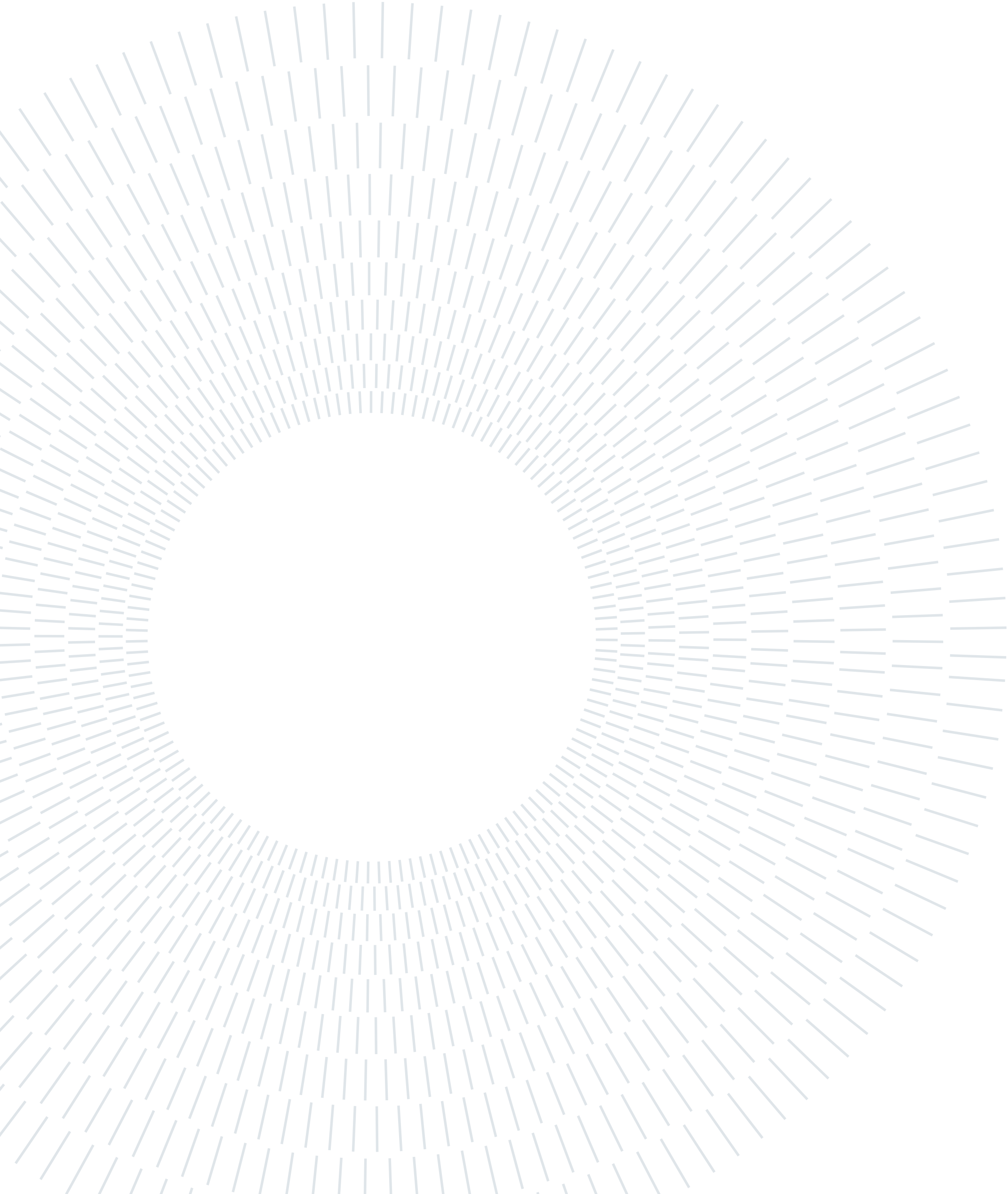

Acknowledgements

I would like to thank myself, my family, my friends, and everyone who loves me.

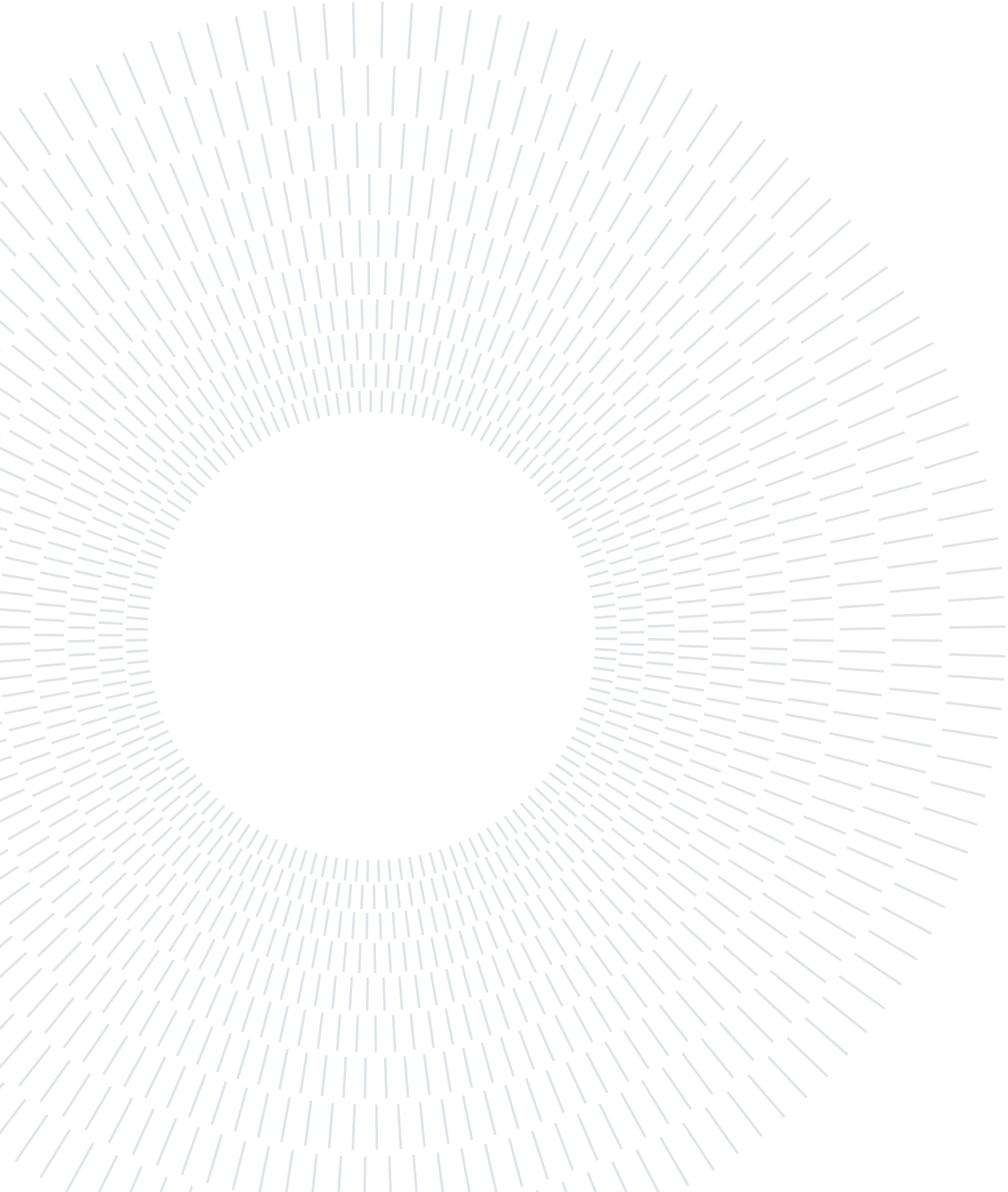

Bibliography

[1] DICOM. URL `https://www.dicomstandard.org`.

[2] C.11.2 VOI LUT module, . URL `https://dicom.nema.org/medical/dicom/current/output/chtml/part03/sect_C.11.2.html#sect_C.11.2`.

[3] Working with DICOM LUT | raster, medical, document help, . URL `https://www.leadtools.com/help/sdk/v21/dh/to/working-with-dicom-lut.html`.

[4] *Radiation Oncology Physics*. Non-serial Publications. INTERNATIONAL ATOMIC ENERGY AGENCY, Vienna, 2005. ISBN 92-0-107304-6. URL `https://www.iaea.org/publications/7086/radiation-oncology-physics`.

[5] S. M. Anjam, N. Banaee, H. Rahmani, and H. A. Nedaie. Determination of geometric accuracy of radiotherapy fields by port film and DRR using Matlab graphical user interface. *Medical & Biological Engineering & Computing*, 57(1): 259–269, Jan. 2019. ISSN 1741-0444. doi: 10.1007/s11517-018-1852-x.

[6] J.-P. Bissonnette. Quality Assurance of Image-Guidance Technologies. *Seminars in Radiation Oncology*, 17(4):278–286, 2007. ISSN 1053-4296. doi: https://doi.org/10.1016/j.semradonc.2007.07.002. URL `https://www.sciencedirect.com/science/article/pii/S1053429607000598`.

[7] N. G. Burnet, S. J. Thomas, K. E. Burton, and S. J. Jefferies. Defining the tumour and target volumes for radiotherapy. *Cancer Imaging*, 4(2):153–161, Oct. 2004. ISSN 1740-5025. doi: 10.1102/1470-7330.2004.0054. URL `https://www.ncbi.nlm.nih.gov/pmc/articles/PMC1434601/`.

[8] J. Canny. A computational approach to edge detection. PAMI-8(6):679–698. ISSN 1939-3539. doi: 10.1109/TPAMI.1986.4767851. Conference Name: IEEE Transactions on Pattern Analysis and Machine Intelligence.

[9] L. Court, H. Wang, D. Aten, D. Brown, H. MacGregor, M. du Toit,

M. Chi, S. Gao, A. Yock, M. Aristophanous, and P. Balter. Illustrated instructions for mechanical quality assurance of a medical linear accelerator. *Journal of Applied Clinical Medical Physics*, 19(3): 355–359, 2018. ISSN 1526-9914. doi: 10.1002/acm2.12265. URL `https://onlinelibrary.wiley.com/doi/abs/10.1002/acm2.12265`. _eprint: https://onlinelibrary.wiley.com/doi/pdf/10.1002/acm2.12265.

[10] T. D. DenOtter and J. Schubert. Hounsfield unit. In *StatPearls*. StatPearls Publishing. URL `http://www.ncbi.nlm.nih.gov/books/NBK547721/`.

[11] R. O. Duda and P. E. Hart. Use of the hough transformation to detect lines and curves in pictures. 15(1):11–15. ISSN 0001-0782. doi: 10.1145/361237.361242. URL `https://dl.acm.org/doi/10.1145/361237.361242`.

[12] J.-L. Dumas, M. Fawzi, H. Masset, S. Losa, R. Dal, N. Pierrat, and L. d. Marzi. Independent 6D quality assurance of stereotactic radiotherapy repositioning on linacs. *Cancer/Radiothérapie*, 24(3):199–205, 2020. ISSN 1278-3218. doi: https://doi.org/10.1016/j.canrad.2020.01.005. URL `https://www.sciencedirect.com/science/article/pii/S1278321820300500`.

[13] S. Gao, W. Du, P. Balter, P. Munro, and A. Jeung. Evaluation of IsoCal geometric calibration system for Varian linacs equipped with on-board imager and electronic portal imaging device imaging systems. *Journal of Applied Clinical Medical Physics*, 15(3):4688, May 2014. ISSN 1526-9914. doi: 10.1120/jacmp.v15i3.4688.

[14] S. Goyal and T. Kataria. Image Guidance in Radiation Therapy: Techniques and Applications. *Radiology Research and Practice*, 2014:e705604, Dec. 2014. ISSN 2090-1941. doi: 10.1155/2014/705604. URL `https://www.hindawi.com/journals/rrp/2014/705604/`. Publisher: Hindawi.

[15] E. Graulieres, S. Kubler, E. Martin, and R. Ferrand. Positioning accuracy of a single-isocenter multiple targets SRS treatment: A comparison between Varian TrueBeam CBCT and Brainlab ExacTrac. *Physica Medica: European Journal of Medical Physics*, 80:267–273, Dec. 2020. ISSN 1120-1797, 1724-191X. doi: 10.1016/j.ejmp.2020.10.022. URL `https://www.physicamedica.com/article/S1120-1797(20)30265-9/fulltext`. Publisher: Elsevier.

[16] M. Guckenberger, W. W. Baus, O. Blanck, S. E. Combs, J. Debus, R. Engenhart-Cabillic, T. Gauer, A. L. Grosu, D. Schmitt, S. Tanadini-Lang,

and C. Moustakis. Definition and quality requirements for stereotactic radiotherapy: consensus statement from the DEGRO/DGMP Working Group Stereotactic Radiotherapy and Radiosurgery. *Strahlentherapie Und Onkologie: Organ Der Deutschen Rontgengesellschaft ... [et Al]*, 196(5):417–420, May 2020. ISSN 1439-099X. doi: 10.1007/s00066-020-01603-1.

[17] W. Guo, R. Müller-Polyzou, Z. Chen, N. Meier, and A. Georgiadis. Patient positioning in radiotherapy. In *2020 IEEE International Symposium on Medical Measurements and Applications (MeMeA)*, pages 1–6, 2020. doi: 10.1109/MeMeA49120.2020.9137355.

[18] A. S. Hassanein, S. Mohammad, M. Sameer, and M. E. Ragab. A survey on hough transform, theory, techniques and applications, 2015.

[19] U.-J. Hwang, K. Jo, Y. K. Lim, J. W. Kwak, S. H. Choi, C. Jeong, M. Y. Kim, J. H. Jeong, D. Shin, S. B. Lee, J.-H. Park, S. Y. Park, and S. Kim. A new method and device of aligning patient setup lasers in radiation therapy. *Journal of Applied Clinical Medical Physics*, 17(1):49–61, Jan. 2016. ISSN 1526-9914. doi: 10.1120/jacmp.v17i1.5527.

[20] M. Kumar, M. Shanavas, A. Sidappa, and M. Kiran. Cone beam computed tomography - know its secrets. *Journal of international oral health: JIOH*, 7 (2):64–68, Feb. 2015. ISSN 0976-7428.

[21] K. A. Langmack. Portal imaging. *The British Journal of Radiology*, 74(885):789–804, Sept. 2001. ISSN 0007-1285. doi: 10.1259/bjr.74.885.740789. URL `https://www.birpublications.org/doi/10.1259/bjr.74.885.740789`. Publisher: The British Institute of Radiology.

[22] R. Leahy, R. Clackdoyle, and F. Noo. Chapter 26 - computed tomography. In A. Bovik, editor, *The Essential Guide to Image Processing*, pages 741–776. Academic Press, Boston, 2009. ISBN 978-0-12-374457-9. doi: https://doi.org/10.1016/B978-0-12-374457-9.00026-3. URL `https://www.sciencedirect.com/science/article/pii/B9780123744579000263`.

[23] W. Lutz, K. R. Winston, and N. Maleki. A system for stereotactic radiosurgery with a linear accelerator. *International Journal of Radiation Oncology, Biology, Physics*, 14(2):373–381, Feb. 1988. ISSN 0360-3016. doi: 10.1016/0360-3016(88)90446-4. URL `https://www.redjournal.org/article/0360-3016(88)90446-4/abstract`. Publisher: Elsevier.

[24] D. Newell and E. Tiesinga. The International System of Units (SI), 2019 Edition. *NIST*, Aug. 2019. URL `https://www.nist.gov/publications/international-system-units-si-2019-edition`. Last Modified: 2021-03-16T05:00-04:00 Publisher: David Newell, Eite Tiesinga.

[25] F. Sciacca. Organs at risk | Radiology Reference Article | Radiopaedia.org. URL `https://radiopaedia.org/articles/organs-at-risk?lang=us`.

[26] P. Sprawls. OPTIMIZING MEDICAL IMAGE CONTRAST, DETAIL AND NOISE IN THE DIGITAL ERA.

[27] V. T. Bicubic interpolation techniques for digital imaging. URL `https://medium.com/hd-pro/bicubic-interpolation-techniques-for-digital-imaging-7c6d86dc35dc`.

[28] D. R. Varma. Managing DICOM images: Tips and tricks for the radiologist. 22(1):4–13. ISSN 0971-3026. doi: 10.4103/0971-3026.95396. URL `https://www.ncbi.nlm.nih.gov/pmc/articles/PMC3354356/`.

[29] X. Wang, L. Xie, C. Dong, and Y. Shan. Real-esrgan: Training real-world blind super-resolution with pure synthetic data. In *International Conference on Computer Vision Workshops (ICCVW)*, .

[30] X. Wang, K. Yu, C. Dong, and C. C. Loy. Recovering realistic texture in image super-resolution by deep spatial feature transform, . URL `http://arxiv.org/abs/1804.02815`. version: 1.

[31] X. Wang, K. Yu, S. Wu, J. Gu, Y. Liu, C. Dong, Y. Qiao, and C. C. Loy. Esrgan: Enhanced super-resolution generative adversarial networks. In *The European Conference on Computer Vision Workshops (ECCVW)*, September 2018.

[32] J. W. Wong. Electronic Portal Imaging Devices (EPID). In L. W. Brady and T. E. Yaeger, editors, *Encyclopedia of Radiation Oncology*, pages 207–213. Springer Berlin Heidelberg, Berlin, Heidelberg, 2013. ISBN 978-3-540-85516-3. doi: 10.1007/978-3-540-85516-3_33. URL `https://doi.org/10.1007/978-3-540-85516-3_33`.

[33] S. Yoo, G.-Y. Kim, R. Hammoud, E. Elder, T. Pawlicki, H. Guan, T. Fox, G. Luxton, F.-F. Yin, and P. Munro. A quality assurance program for the on-

board imagers. *Medical Physics*, 33(11):4431–4447, Nov. 2006. ISSN 0094-2405. doi: 10.1118/1.2362872.